This is an Accepted Manuscript, which has been through the Royal Society of Chemistry peer review process and has been accepted for publication.

Accepted Manuscripts are published online shortly after acceptance, before technical editing, formatting and proof reading. Using this free service, authors can make their results available to the community, in citable form, before we publish the edited article. We will replace this Accepted Manuscript with the edited and formatted Advance Article as soon as it is available.

You can find more information about Accepted Manuscripts in the Information for Authors.

Please note that technical editing may introduce minor changes to the text and/or graphics, which may alter content. The journal's standard Terms & Conditions and the Ethical guidelines still apply. In no event shall the Royal Society of Chemistry be held responsible for any errors or omissions in this Accepted Manuscript or any consequences arising from the use of any information it contains.

Low-dimensional II-VI semiconductor nanostructures of ternary alloy and transition metal ion doping: Synthesis, Optical properties and Applications

Arfan Bukhtiar [a,b*], Zou Bingsuo [a,c*]

a MOE Key Laboratory of New Processing Technology for Non-ferrous Metals and Materials; State Key Laboratory of Featured Metal Materials and Life-cycle Safety for Composite Structures, Guangxi University, Nanning 530004, China

b, School of Physical Science and Technology, Guangxi University, Nanning 530004, China

c, School of Resources, Environments and Materials, Guangxi University, Nanning 530004, China

Abstract

Light matter interaction for spin-controlled devices has gained lot of attention in past few years also known as dilute magnetic semiconductor. Strong electron-phonon interaction and outstanding excitonic behavior of II-VI semiconductor is an advantage over III-V semiconductors especially for low dimensional system. Herein, we comprehensively review the spin-exchange interaction of transition metal ion doping through sp-d exchange that enhance the possibility of spin-based photonic in binary, ternary alloy and transition metal ion doping in II-VI semiconductor. For one-dimensional structure, few number magnetic ions can ferromagnetically coupled to form exciton magnetic polaron to give coherent spin-polarized emission, which opens a new horizon to develop bandgap tunable, active waveguide, tunable emission and lasing at nanoscale based on different structures, composition, morphology as well as excitation conditions. The photonic crystal supplies significant information about photon-exciton interactions in the coupled optical microcavities. Lastly, we extend the discussion to the most recent advancement of one-dimensional structure for device application and possible prospective in future technology.

Keywords: Dilute magnetic Semiconductor (DMS), II-VI semiconductor, Binary and Ternary Alloys, Transition metal (TM); Tunable bandgap and emission behavior

1. Introduction

Incorporation of transition metal (TM) ion in II-VI semiconductors and their ternary alloy exhibits spin-carrier injection and spin-spin coupling due to p-d hybridization (involving anions and TM

ions) and extensively used for dilute magnetic semiconductors (DMS) applications. DMS is an emerging class of semiconductors that exhibits both semiconductor behavior as well as ferromagnetic response. For practical application, the DMS must show ferromagnetic response at room or above room temperature after Dielt et al theoretical prediction of ferromagnetic display in wide bandgap semiconductor [1]. Extensive research on II-VI-based DMS over last two decades has led to the construction of DMS-incorporated structures such as quantum wells and superlattices. The exchange interaction between (s, p) bands of the host lattice and d-band of the magnetic ion is responsible for magneto-optical and magneto-electrical effect at room temperature. The d-d transition peaks of transition metal ions in the II-VI semiconductors are influenced not only by exciton recombination process but also by spin-related couplings [2]. Recent advancement in DMS shows the antiferromagnetic (AFM) coupled ion observed at room temperature that show the d- d intra-band transition peaks at higher in energy side than FM coupled ions. Spin related micro-photoluminescence (PL) response and theoretical study reveals the red-shift of d-d transition peak of Mn(II) ion in FM system assisted as bosonic laser and other spintronics application. Polarons are quasi-particles that interact at the quantum state coupled with spin of localized magnetic ions in DMS called Magnetic Polarons. Magnetic polarons are subdivided into bound magnetic polarons (BMP), free magnetic polarons (FMP) and excitonic magnetic polarons (EMP). EMP is self-organized magnetic quasi-particle that is formed by the excitons in DMS. At high excitation power, EMP merged due to overlapping tails of carrier waves function and form long cluster of collective magnetic polarons and forming large ferromagnetic domain. The large collective response of exciton magnetic polarons state pronounced the bosonic behavior [3–5]. Spintronic is an advanced device technology that utilizes quantum spin states of electrons as well as controlled charge states (spin up and spin down) for magnetic memory devices or switching applications. The integration of electronics, magnetism and spin in single device is an extremely important research topic for the development of spintronic devices. An important task related with spintronic devices such as MRAM, spin LED and Spin FET is to make the spin injection within the materials as effectively and efficiently control the spin transport and detection within semiconductor devices [6–8].

II–VI semiconductors especially zinc chalcogenides (ZnO, ZnS, ZnSe, and ZnTe) and cadmium chalcogenides (CdS, CdSe and CdTe) have been intensively studied in the field of one-dimensional (1D) nanostructures due to their superior optical properties [9–12]. 1D nanostructure within few

nanometer range (lateral dimension between 1 to 100 nm) has gained immense attention over the past three decades due to its numerous fascinating properties that can be tuned by changing their shape, size and growth conditions [13–16]. Various optical phenomena such as electron–exciton interaction, electron–phonon interaction, and other emissions such as donor–acceptor pair exciton and anti-sites emission are important to understand the crystal quality of 1D nanostructure and their sensitivity to light. Zinc and cadmium chalcogenides cover the spectral range from 2.25 eV to 3.37 eV (Visible to UV) and 1.4 eV to 2.42 eV (NIR to Visible); their direct bandgap along with quantum confinement makes it suitable for future optoelectronic application. The ternary alloy of II-VI semiconductor can tune its bandgap with variable stoichiometry ratio that their response to multi-spectrum wavelengths. Utilizing the quantum confinement effect in 1D nanostructure in ternary alloy has gathered immense attention for tuning bandgap for technologically motivated research based on photon absorption or emission as synthesized by physical deposition methods such as chemical vapor deposition [16–18].
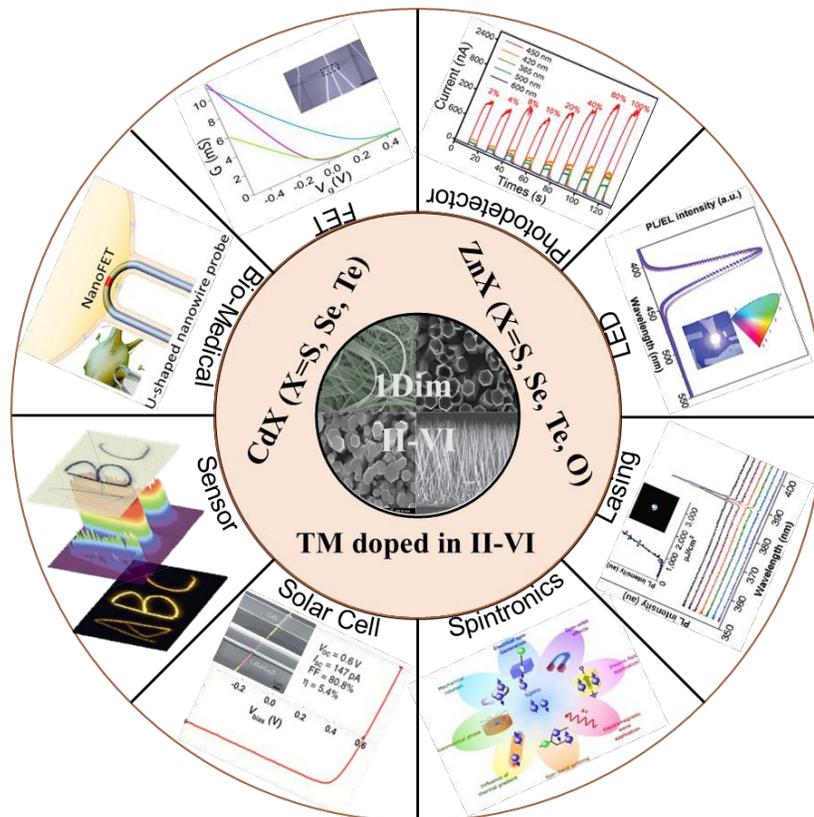

Figure 1: Graphical display of II-VI semiconductor.

1D structures (scale down to submicron range) have shown unique properties in extensive and novel applications. 1D structure of nanowires (NWs) and carbon nanotubes (NTs) has inspired great interest from curiosity-driven and technology-motivated research, which were originally called "whiskers" and more recently known as nanobelts (NBs) [19]. As, the size scaled down from bulk to 1D (scale down to submicron); the exchange interaction of spin and carriers had new predominant aspect that modified the optical and electrical properties with the help of external magnetic field commonly used in spintronic, optical imaging and others [20]. In the last decade, high-quality II-VI ternary alloy 1D nanostructures have been prepared for tunable nano-lasers, LED, solar cells and photodetectors with elaborate control and reproducibility achieved by various research groups [21–23]. Therefore, the current progress in 1D nanostructure ternary alloy of II-VI semiconductors has strengthened the expectation of its pivotal role in the future application of energy conversion and biological application (Figure 1) [16,24]. Different prototypes have the capability to assemble and integrate individual structures into functional devices on a large scale. 1D hybrid nanostructures are highly appropriate in various optoelectronic applications such as Type-I or Type-II junctions; Type-I junction exhibits high fluorescence and light emitter yield (LED and Laser), while Type-II junctions facilitate the formation of e–h pairs with improved energy conversion efficiency [21,25].

In this review, we explore the curiosity-driven/achievement and technologically motivated research over the past decade related to 1D micro/nanostructure of II-VI semiconductors and its impact on the device application industry. In the introduction, we presented a general background about the 1D nanostructure related II-VI semiconductor and its ternary alloys; and TM doping within II-VI materials and its ternary alloy. Incorporation of TM exhibits spin-carrier injection, spin-spin coupling among TM ions and p-d hybridization which make direct semiconductor multitudinous potential in photonic and optoelectronic applications. EMPs, BMP and Localized EMPs are striking areas for DMS that need vast field of study to explore 1D systems. Finally, we discuss the future perspectives of 1D nanostructure for II-VI semiconductors, its ternary alloy with and without doping, and its potential for new device applications.

2. Synthesis of 1D Nanostructure from II-VI semiconductor and its Alloy

Various research groups synthesized 1D nanostructures II-VI semiconductors by different techniques. Each synthesis mechanism is a crucial stage to grow 1D nanostructures that have good

reproducibility, crystallinity and most importantly cost-effectiveness. Therefore, the realization of chemistry and physics of nanostructure is reasonably supportive to control the growth pattern, crystal structure and compositional complexity for practical applications of materials toward novel technologies [26,27]. Lieber and co-workers reported the NW based application in biochemical sensors, extracellular and intracellular electrical sensors, molecules delivery, injectable electronics, biosynthesis and optical neuromodulation for brain science. Moreover, the importance of NW structures such as axial, radical/coaxial modulated, branched and kink are subsequent generation building blocks for bioelectronics, photonics and electronics circuits. High surface-to-volume ratio, fast signal response, high temporal resolution and minimum energy consumption highlighted the importance of nanostructures for future applications [28–30].

II-VI 1D nanostructure ternary alloy of cadmium and Zinc chalcogenides have been widely used in various applications due to their tunable bandgap behavior and excellent transport properties. Binary alloy bandgap can be tuned by changing the nanomaterial size; meanwhile, the ternary alloy bandgap is adjusted by changing their composition [31–33]. TM ion doping in binary and ternary II-VI alloy can tune its bandgap along with magnetic ion inner conversion and energy transfer within the crystal symmetry of the host II-VI materials. Therefore, light-matter interaction provides fascinating information and tunable optical emission from ferromagnetic semiconductors, which usually arises from carrier-spin interaction, spin-spin coupling and sp-d hybridization between anions and dopant ions [5,34,35].

2.1 Growth Mechanism

Synthesis of 1D nanostructures from II-VI semiconductors has been demonstrated by nucleation growth in vapor phase mechanism and solution process. The merits of vapor phase mechanism is to produce high crystal quality of II-VI material due to the high temperature growth process. Wagner and co-workers introduced vapor liquid solid approach that is currently quite established and intensive use to grow 1D nanostructure for different research applications with device integration [36]. Meanwhile, the solution process is relatively cost-effective to prepare 1D nanostructure at lower temperature only compromising its crystallinity. In this section, we detail elaborate growth mechanisms and experimental techniques to prepare high-quality 1D structures from II-VI semiconductors and recent development in ternary alloy for production of high-quality and critical stoichiometry for future application [37–39].

2.1.1 Vapor phase growth

Vapor phase growth involves two main mechanisms (i) nucleation growth and (ii) without nucleation growth also known as vapor liquid solid (VLS) and vapor solid (VS) mechanism. In nucleation growth, the catalyst initialize the growth mechanism and act as seed during growth in which host material vaporized in the presence of source gas and react with catalyst (act as seed) to form 1D nanostructure. Shape, size and morphology can controlled by controlling the catalyst shape and size as the function of temperature [39–41].

Vapor liquid solid (VLS) growth: The VLS growth is the most extensively and widely adopted process to synthesize high crystalline, flexible and large-scale 1D nanostructures. The kinetic of VLS is based on alloying formation of catalyst and host material, which lead to formation of single or branched-shaped homo/heterogeneous nanostructure on single substrate. To control the kinetic of VLS is challenging to probe under conventional condition. Therefore, two-zone and three-zone temperature furnaces are employed to analyze the fast kinetic or in-suit techniques such as transmission electron microscopy (TEM) to investigate the growth kinetic with real-time domain [40–42]. Shape, size, crystal structure and morphology of desired material depend on solid liquid alloy formation or adsorption of liquid solid interface is in supersaturated form, which depend on numerous parameters such as pressure, deposition temperature and time, carrier gas flow and catalyst droplet size [43,44]. Moreover, polarity determination in II-VI semiconductor with dumbbell pairs analysis with high angle annular dark field (HAADF) scanning transmission electron microscopy (STEM) imaging for high-medium atomic number and low atomic number NWs obtained from VLS mechanism. Such change in polarity in NW leads to twining or polymorphism formation at elevated temperature. Therefore, HAADF and STEM provide suitable information about complex hetero-structure and hetero-interface between polar and nonpolar semiconductors [45–47]. Self-catalytic growth in VLS is special case in which self-constituent metallic element serves as the catalyst for host compound formation; for example, Cd metallic particles are used to grow cadmium chalcogenides. However, Van der epitaxial growth in VLS also support the self-catalytic growth micro/nanostructure on mica substrate reported by various groups based on II-VI materials. High-quality micro/nanostructure growth directly correlated with the substrate temperature, source gas, flow rate, evaporation temperature of host material and growth time [47–50].

***Vapor Solid (VS) Growth*:** The vapor solid mechanism is a spontaneous condensation process without use of catalyst or metal droplet. Spontaneous condensation of vapor into solid is induced by the decrease in Gibbs free energy from crystallization or decrease in super-saturation [45,49]. Reaction temperature in VS mechanism is slightly higher than VLS that accumulate anion-cation adatom onto the substrate. The quality of nanostructure obtained from the VS mechanism directly depend on growth temperature, time and super-saturation ratio for high diffusivity of the adatoms. VS mechanism has been associated with the radial thickening (formation of NB) and tapering of NWs at high super-saturation at elevated temperature. For II-VI semiconductors, numerous reports available on wurtzite phase crystal structure grow as NBs under appropriate ambient conditions [50–52].

2.1.2 Solution process

The solution process is also widely used to grow 1D colloidal NWs at low temperature in comparison with VLS or VS mechanism. It exhibits numerous advantages over high temperature growth methods such as controlled diameter, surface passivation, solubility and large production. Diameter can be controlled in solution process either with help of surface capping ligands or surfactant free method. In surfactant method, monodisperse metal catalyst nanoparticles (NPs) having diameter of few nanometers help to grow colloidal NWs which is protective by surface capping ligands around the nanostructure. While, surfactant free nanostructure is prepared in squalene (as solvent) and semiconductor precursors; where semiconductor precursor thermally decompose into nanodroplet and subsequently provide assistance to grow NWs [25,35]. Similarly, organometallic (metal with low melting point) precursors are dissolved in an organic solvent at elevated temperature; formation of liquid–metal droplets (few nanometer) act as catalyst to from nucleation process followed by the growth of 1D structures of II-VI ternary alloyed [53–55].

***Solution liquid solid (SLS) growth*:** The SLS is used to synthesize crystalline structures below 200 ˚C in the presence of catalysis (Bi, In, Sn and Ga). Metallic catalyst used to prepare colloidal structure of various compositions and structures (such as axial heterojunction, core/shell, etc.). SLS growth is similar to VLS growth, but difference of low temperature in control environment. Influence parameter is temperature in SLS that will control the diameter of rod and wire in the range of 2-20 nm diameter [25,34]. Moreover, various heterostructures of Type-I and Type-II of II-VI semiconductors were reported with solution growth mechanism. For Type-I (CdS/CdSe),

exciton recombine in core of CdSe and CdS server as the concentrator to improve the light efficiency. While, Type-II (CdSe/CdTe) serves as the two localized charge carriers exhibits the Coulomb interaction, exchange interaction of interface-related exciton recombination [54,56–58].

2.2 Growth Extension

Single Nanowire Array: Single NW array have been achieved by epitaxial growth on a crystalline substrate. The crystalline planes of substrate effectively control the orientation of NWs over large scale; which is very important for device fabrication. II–VI NWs grown epitaxially on the substrate surface with lattice mismatch less than 10 % show tremendous photonic response. The building block of NWs formation is the hetero-interfaced between host material and catalyst particle that helps to grow fast structure perpendicular/vertical on the substrate surface along with large tolerance to lattice mismatch [59]. Epitaxial growth of ZnO NW arrays first reported by Yang and co-workers that have been extensively reported in a broad range of electronic and photonic applications [60,61]. Moreover, fast growth of NW array enable lattice relaxation in lateral dimension that leads the formation of large critical height prior to defect nucleation as reported for lattice mismatched epitaxial films. High growth temperature is suitable for high crystalline material growth and epitaxial growth practice the covalent bond between 1D structure and substrate, thus requiring corresponding of in-plane parameters to overcome the crystalline defects. Van der Waals interaction or epitaxial provide strong chemical bond between heterojunction with minimum impact on lattice matching. Various II-VI materials nanostructures have been successfully grown using Van der Waal epitaxial method exhibiting strong luminescence behavior [46].

Heterostructure Nanowire: Heterostructure nanostructures is classified as (i) axial and (ii) radial structure. Axial heterostructures have same diameter of two different materials and radial has two different materials with different diameters also known as core/shell nanostructures reported in 2002 [60,61]. Heterostructure or heterojunction NWs have various advantages in bioelectronics, solar cells and various photonics devices. Lieber and co-worker also reported that the coaxial multishell NWs materials depends on degree of freedom (DoF) that synthetically modulated and tuned properties have led to advances in nanophotonic [62–64]. Moreover, the branched nanostructures with heterogeneous or homogeneous junction make it more complex design but open new horizon in various energy related applications. Branched NWs with homo or heterogeneous junction provide a higher degree of complexity to allow for the design of interconnected hierarchical nanostructures

with rich electrical, optical, and chemical properties, especially in energy applications [65–67]. Wang and co-worker reported heterojunction/hyper-branched of Si and GaN NWs [68]. Dai and co-worker reported CdSe/CdS core/shell NWs prepared by two-step process with CVD [69]. Pan reported a one-step thermal evaporation of multiple source to synthesize Si/CdS_xSe_{1-x} core/shell NWs [70–73]. Moreover, the composition of CdS and CdSe precursor in CdS_xSe_{1-x} NW can altered its length for 1D nanostructure in CVD along with composition grading, lateral and branched heterostructures formation of CdS_xSe_{1-x}. In addition, Buhro reported the $ZnSe_xTe_{1-x}$ NWs grow by solution process with composition gradient. The growth of $ZnSe_xTe_{1-x}$ NWs employed three-segment heterostructure having ZnSe and ZnTe localized at extreme end of NWs [74].

Composition gradient / Transition metal ion Doping: Composition gradient within 1D II-VI semiconductors illustrate board range tunable emission in a single structure which is quite difficult to attain with planar epitaxial growth. Axial direction growth of NWs are important for bandgap gradient obtained from vapor phase growth mechanism [75]. The composition gradient and doping profile can be controlled by precursor concentration or stoichiometry ratio and substrate temperature zone as reported by Zhang and others [75–78]. Similarly, the TM ion doping in II-VI materials make it suitable for future applications such as spintronics [79–82]. The origin of ferromagnetism in semiconductor especially II-VI semiconductor is related with spin exchange interaction between TM ions impurity and carriers available at conduction or valance band through sp-d exchange interaction. Available electron in the outer level (3d and 4s) of TM is of great interest to explain the possible carrier-spin interaction. Electron spin is a quantum phenomenon coupled with magnetic moment and degree of spin that carried out the information of spins up or spins down. Mn, $3d^5$ shell is half filled and $4s^2$ electron bonding to s-p^3 bonding. According to Hunds rule, 5d-electrons has parallel spin and opposite spin considerably need large energy. Coulomb potential, carrier-spin (electron-spin) interaction and Mn-Mn (spin-spin) interaction are possible interaction reported in DMS by different groups. Zou and co-workers reported various II-VI materials 1D nanostructures doped with TM ion for DMS application will be detail discussed in the next section.

3. Fundamental Optical Properties of II-VI Nanostructure

II-VI semiconductors have wide range of direct bandgap materials that normally reveals high optical absorption and emission within visible range. Cadmium and Zinc chalcogenides are

promising potential II-VI materials in the field of 1D nanostructures that have been extensively studied over last two decades for various optical applications, due to their high quantum efficiency and light sensitivity. II–VI semiconductors have wurtzite-type structures, zinc blende and diamond like structures [83–85]. For wurtzite-type structure, valence bands arise from p-states having lower symmetry than diamond and zinc blende like-structures. Inversely, the minimum of the conduction band is $\Gamma 7$ symmetry with an s-state. The valence band is splitting into three sub-bands due to the spin–orbit coupling and crystal field; A-exciton ($\Gamma 9$ or heavy hole), B-exciton ($\Gamma 7$ or light hole), and C-exciton ($\Gamma 7$ or split-off (SO) band). In order to investigate the optoelectronic or photoelectrical behavior within II-VI semiconductors, one must develop the deep understanding of the band structure related exciton transitions. In this section, we highlighted the recent progress in zinc and cadmium chalcogenides binary alloy, ternary alloy and TM ion doping in 1D nanostructure related electronic and optical transition.

3.1 TM ion doping in Cadmium chalcogenides (CdX; X=S, Se, Te)

3.1.1 CdS

Cadmium sulfide is an attractive II-VI semiconductor material with bandgap of 2.4 eV in the visible range has been extensively used for various optoelectronic application. 1D nanostructure of CdS exhibits the strong luminescence, high mobility and excellence transport behavior in comparison with bulk material [86–89]. Since, II–VI compound semiconductors are traditionally optically active, therefore exploration of their luminescence properties is essential for various optical applications. Excitons are quasi-bosonic particles that freely move in the crystal lattice as well as describe the bound state of an electron–hole (e-h) pair with electrostatic Coulombic force interactions. Therefore, the carrier-carrier, carrier-exciton and carrier-phonon interaction exhibit superior features under excitation wavelength [90–92]. In comparison to their bulk counterparts, nanostructures have contemporary higher exciton–polariton coupling strength. Leite et al. reported the temperature dependent multiple phonons in CdS under different excitation power that exhibit strong electron-lattice interaction [93]. In addition, the ternary alloy and TM ion doping with II-VI material typical luminescence process provide suitable information to understand the transition state of electron relaxation to the ground state [94,95].

Transition metal ion related Luminescence behavior

TM doping in 1D CdS is quite interesting for DMS application; the d-d transition between the ground state $^6A_1$ and first excited $^4T_1$ state for ferromagnetic (FM) and antiferromagnetic (AFM) coupled of spin ions in host matrix makes it useful in various spin related application [95–97]. Ge et al. reported the coherent bosonic lasing of EMP at 520 nm at 232.393 uJ/cm^2 for Ni doped CdS synthesized by VLS mechanism. 1D CdS with TM ion doping excited with different wavelengths (405nm and 532 nm) to understand the Mn^{+2} transition with the host CdS crystal symmetry [98]. EMP emission from Ni(II) doped in CdS and Mn doped CdS 1D nanostructure synthesized by VLS mechanism has been reported by various groups. Moreover, the Zhang et al. also reported the Sn doped CdS low threshold value for NW laser due to Plasmon Polaritons [99,100]. LEMP emission formation in CdS is related to Ni cluster formation even at low doping concentration. High doping concentration (up to 2-4%) show the NiI2 cluster emission in CdS related to LEMP, consistent with theoretical ab initio calculation by VASP software. The localized and delocalized states interact with d-bands show LEMP for delocalized charge transfer effect of coupled Ni ions surrounded by I and S ions. The LEMP decay via efficient hopping mechanism for high Ni doping and behave coherently. Interestingly, the FM coupling of the Ni(II) pair has stable energy lower of 121 meV than the AFM Ni pair, indicating that the incorporation of Ni ion in host lattice modifies its band structure. From DOS, the d-band is occupied above fermi level, close to conduction band minima. Strong hybridization of d-band with valance band dominant the exciton and exciton-spin interaction. However, for AFM, metallic states of d-band are dominant as distributed cross at the fermi level. Another prominent effect known as the charge transfer effect is also been reported at which the spin-down state contact with continuum conduction band and d-states could extend the band edge to lower energy. Charge transfer effect at continuum state combined with FM coupling will lead second band at near highest d-level called bound EMP or BEMP. Therefore, the aggregation of Ni cluster and FM coupling of d-d transition energy states can exhibit the LEMP and BEMP in 1D NBs. The LEMP can form BEMP as FM ion coupled with TM aggregate and doping formed charge transfer at low energy side due to M-L cluster in CdS lattice to produce single-mode lasing and EMP lasing as excited by fs-laser. High excitation density of coherent exciton may lead to the formation of coherent EMP or CEMP for lasing. The spatial and energy difference between two EMPs and BEMP (LEMP) level have a much longer lifetime, lowest energy and limited space. Therefore, the CBEMP state at a smaller threshold to

produce lasing with fs pulse pumping. As, the EMP threshold value is achieved, the EMP produces lasing through CEMP formation with coherent emission. Therefore, the bosonic nature favors the formation of CEMP, LEMP and CBEMPs in the host lattice to produce the EMP condensate for single-mode lasing and spontaneously coupled with spin will produce multi-exciton emission. This new concept related to exciton-magnetic polaron can tune the intrinsic microscopic interactions in strongly correlated compounds related to size and spin ion-doping ratio in DMS. Therefore, the excitonic nature will produce multi-spin-coupled polaronic excitonic states that may lead to their new magnetic and/or spin-related optical properties [5].

Figure 2a shows the electronic band structure of pure CdS; Figure 2b reveals the density of state for single Cd, S and CdS through sp hybridization of occupied and unoccupied available state [95,101]. Figure 2c shows the Mn atom doping in CdS as theoretical studies predict that one Mn replace Cd due to smaller ionic radii for spin distribution iso-sphere and spin polarization. The Mn related d-d transition happen, when TM ion doped in crystals and the magnetic coupling within the lattice influences its location. The binding energy of Mn-3d state for magnetic ion impurity in semiconductor is to optimize Hubbard parameter (U= 2.8 eV) for $2\times2\times2$ supercell that show strong correlation with experimental data for d-d transition in Mn doped CdS [102,103]. Figure 2c shows the spin-polarized electronic band structure of single Mn-doped CdS calculated along high symmetry directions. For two Mn ion contribution leading 5.6% of dopant impurity in supercell shows the energy difference between antiferromagnetic and ferromagnetic state in 26 meV. Simulation results shows the favorable antiferromagnetic for long-range dopant in CdS nanostructure. Optical absorption of electronic transition for occupied and unoccupied state as shown in Figure 2d for pure and doped CdS. For pure CdS, the absorption edge occur at 2.43 eV generated between S-2p and Cd-2s with valance and conduction band. As compare with the Mn doped CdS, doped sample has weak band edge peak intensity and shifted toward smaller energy zone. For single Mn related emission exhibits at 2.20 eV, close to experimental value of 2.13 eV for d-d transition; while double Mn ion peak is attributed at 2.38 eV. The d-d transition of double Mn is larger than single Mn ion owing to AFM coupling of Mn ion in CdS system. Therefore, d-d transition between the ground state $^6A_1$ and first excited $^4T_1$ state for FM and AFM coupled Mn ions. For AFM coupling, one Mn ion of spin-up interact with the empty spin-up state exhibits the blue shift in comparison with FM coupling as observed in luminescence spectra for other II-VI semiconductors [103–106].
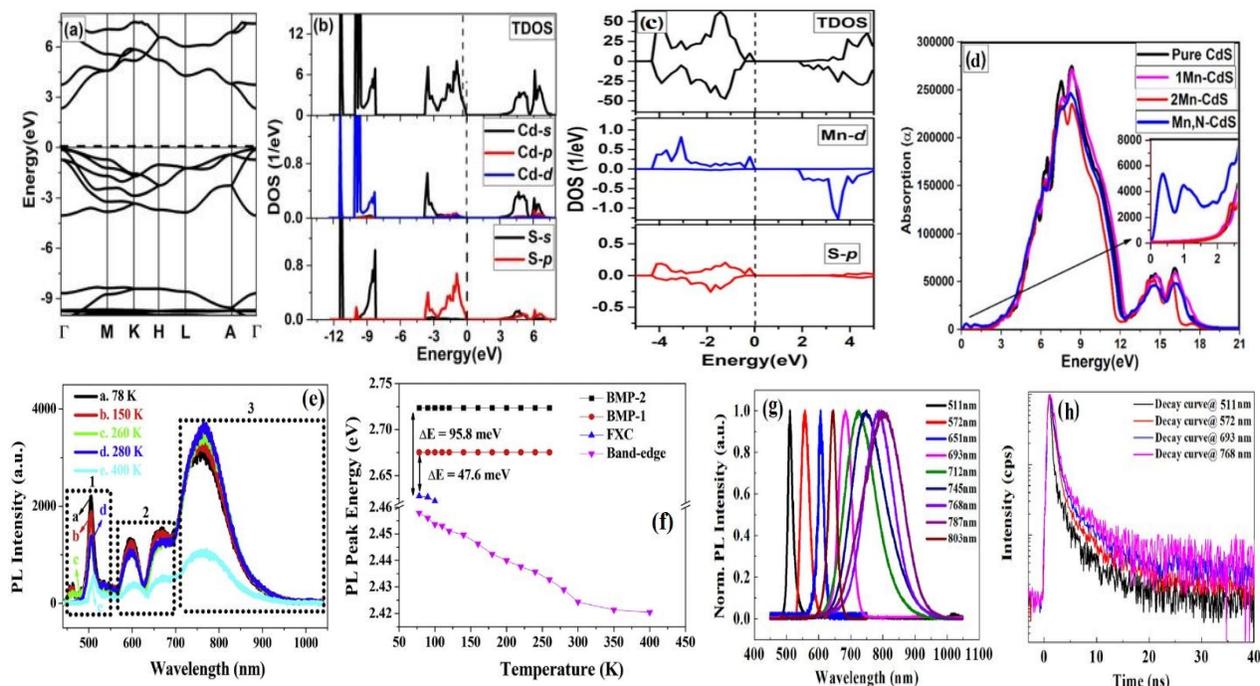
Figure 2: (a) The calculated band structure and (b) TDOS and PDOS of Pure CdS. The TDOS and PDOS of Mn-d, S-p and N-p for FM configurations in (c) $Cd_{34}Mn_2S_{36}$. (d) The calculated optical absorption coefficient for pure CdS and Mn-doped CdS with and without N co-doped [95]. (e) Temperature-dependent micro-PL spectra in the bright-field optical image of an individual Mn-doped CdS nanosheet. (f) Temperature dependenft PL peak positions of the band-edge for CdS (purple), FXC (blue), BMP-1 (red), and BMP-2 (black) in the Mn(II)-doped CdS nanosheet. (f) AFM and FM coupled Mn ions in CdS [107]. (g) PL spectra of the obtained single undoped CdS and Mn^{+2} doped CdS belt at 300 K. The black line is from the pure CdS belt and the other lines are from the emission of CdS doped with different Mn ions. (h) PL lifetime decay plots for the band-edge emission along with Mn^{+2} related emissions at room temperature in a Mn-doped CdS single belt excited at 405 nm [102].

Figure 2g shows the PL spectra 1D belt like structure of both undoped and Mn(II) doped CdS and Mn(II)-doped synthesized by VLS mechanism. Undoped CdS show strong near bandedge emission at 508 nm and no emission peak appears after 525 nm [5,102]. For Mn doped samples, the luminescence spectra shows the emission spectra ranging from 570-900 nm other than bandgap emission as shown in Figure 2g. Multiple emission peaks appears in the emission spectra is due to d-d transition in the ferromagnetic $(MnS)_n$ cluster. Emission peak at 510 nm and 518 nm in doped

sample is due to EMP as also reported for nanocrystal (NC) by different research groups [104–106].

Therefore, tunable emission with different Mn ion in 1D CdS NB make it interesting for various

DMS applications. Such emission is an interaction between free exciton and ferromagnetic cloud

already reported in other II-VI materials [97]. Yellow band emission at 572 nm is attributed from

Mn^{+2} as reported at 576-598 nm; which is assigned to d–d transition between the $^4T_1$ excited state

and the $^6A_1$ ground state of Mn^{+2}. Emission peaks other than band edge also appears independently

under 532 nm excitation source below band edge with the existence of near band edge emission at

515 nm for 405 nm excitation. Such tunable emission owing to Mn interaction with host material

has been rarely reported for DMS structures [8,103]. Thus, the ferromagnetic exchange in this (MnS)n

cluster has strong coherent coupling between magnetic ions within the lattice that may lead to the

formation of localized exciton magneton polaron formation because of the p-d hybridization and

FM coupling [108–110]. Figure 2h shows the PL decay curves for 1D CdS with TM ion doping excited

with different wavelengths (405nm and 532 nm) to understand the Mn^{+2} transition with the host

CdS crystal symmetry [102]. From PL decay curve, we can understand that the small change with

few nanosecond (ns) smaller than free exciton lifetime indicate that it is related to combination of

free exciton and EMP in Mn doped CdS and large change due to inhomogeneous states (defect)

present in the structure. But steady changes in lifetime in the same direction indicate the emission

spectra from red to near IR is Mn ion related and no defect related state involve within bands.

Further increase in excitation power will reduces the lifetime due to interaction of more spin states

and large coherent [111–113]. Therefore, this lifetime ranging within 1 ns reveals the reflection of

spin–spin interaction during lattice relaxation as reported in other II-VI semiconductors. Figure 2e

show the luminescence spectra of Mn doped CdS nanosheet. Figure 2e has highlighted the three

different emission spectra within the range of (1) 440–550 nm (2) 560–680 nm and (3) 700–1050

nm. Emission spectra ranging from 440 nm to 550 nm (green emission) at 78 K subdivided into

triplet emission owing to splitting of valance band into three sub-bands. According to crystal field

symmetry, spin-orbital interaction of excited electron can occupied three exciton energies [A-

exciton (2.5535 eV), B-exciton (2.5675 eV) and C-exciton (2.629 eV)] [107,114,115]. Figure 3f

confirms the existence of band edge emission, free exciton emission and spin-exciton interaction

at low temperature. Moreover, the band-edge peak emission as function of temperature is mainly

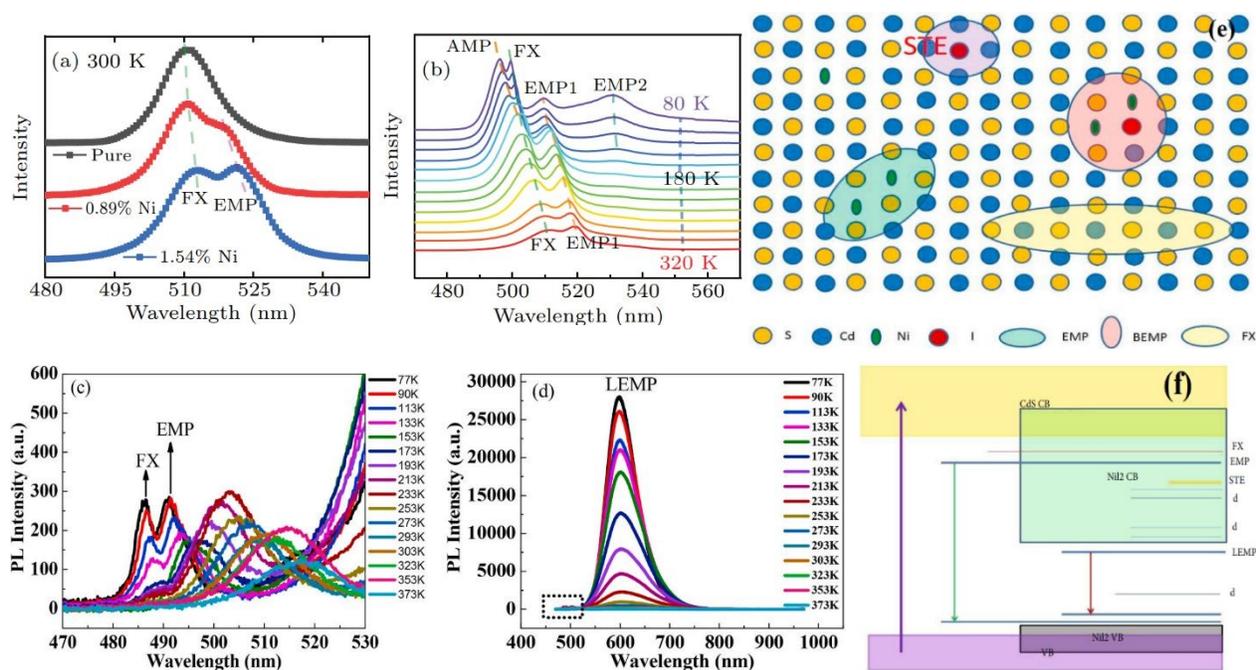observed in wide bandgap semiconductors.

Figure 3: (a) Micro-PL spectra of CdS NB with different Ni concentrations in a range of 480 nm – 550 nm at RT (b) Temperature-dependent micro-PL spectra of CdS NB with Ni concentration of 1.54% in range of 470 nm – 570 nm [98]. (c) Temperature dependence of PL of the single Co-doped CdS NB excited with CW laser at 405 nm. (d) Magnified selected spectrum in the range 470–530 nm, as marked by a rectangle [5]. (e) The spatial distribution diagram of the different excited states in NiI-doped CdS lattice. (f) The electronic structure of $CdS:NiI_2$ NB, in which the nanocluster of NiI_2 is incorporated [116].

Ge et al. reported the coherent bosonic lasing of EMP at 520 nm at 232.393 uJ/cm^2 for Ni doped CdS synthesized by VLS mechanism [98]. Figure 3a, b show the room temperature PL spectra of doped and undoped CdS and low temperature PL spectra for Ni concentration of 1.54% in CdS NB, respectively. For VLS mechanism, the S vacancies are normally generated during growth of 1D system in the presence of Hydrogen in source gas. In case of Ni^{+2} doped in CdS, the dopant atom substitute the Cd ion for higher concentration but this may not happen for low doping concentration [114,115,117]. Another important discussion is the crystal symmetry of host material and dopant ion interaction with crystal symmetry. Under luminescence, the transition of carrier excitation and de-excitation/recombination will provide detail information about spin-carrier interaction within semiconductor. Therefore, the EMP related peak in Ni doped CdS will become more dominant with increase in dopant concentration that directly correlated with the coupling of

dopant cation in crystal symmetry. For pure CdS belt like structure exhibits the redshift in PL spectra is owing to deficiency of S ion during growth that may lead to the formation of donor levels in the conduction band. As, the dopant ion incorporated in CdS lattice will enhanced more defect within the host lattice that may produce strong exchange interaction of spin magnetic ion with native defect states [115,117,118]. Such strong exchange interaction produces the board EMPs emission or redshift at room temperature. Ge and co-worker show the increased in intensity ratio of free exciton and EMP emission. The lattice shrinkage may weaken the electron-phonon interaction at low temperature. At 80k, different peaks appears in the emission spectra corresponding to free exciton, EMPs and antiferromagnetic magnetic polarons of Ni^{+2} pairs. Moreover, the bosonic lasing of EMPS condensate out of complicated states as excited by femtosecond (fs) laser as reported in other II-VI 1D nanostructures [3,117]. Spectra ranging from red to near-IR originated from FM coupling with Mn cluster as become prominent at below 260 k is owing to localized EMP as observed in Mn doped CdS. Same behavior of EMP formation has been observed in ZnSe for Co-doped NWs. However, lowest transition level for Co doped CdS exhibits the p-d hybridization through the high 3d state normally possessed the longer life time [118]. Low temperature luminescence spectra of Co-doped CdS reveals the strong free exciton, EMP and LEMP emission as shown in Figure 3c, d. TM concentration with the host material also result red shift in the band edge and LEMP emission due to the high level of d-d transition from $^4T_1$ (P) to $^4A_2$ (F) of Co ion [5,119–121]. As the temperature is lower than room temperature, slightly blue shift in emission spectra of intra-shell d-d transition emission implies that d-d transition in Co doped CdS is less localized than Mn doped CdS lattice. From VLS mechanism, various studies highlights the successful incorporation of TM ion in 1D CdS NWs and NBs that exhibits the room temperature ferromagnetism and anti-ferromagnetism. Ni doped CdS crystal also reveals the board EMP emission at 600 nm attributed to the d-d transition of $^3T_1$(P) to $^3T_1$(F) of intrinsic Ni(II) ions in sulfide. Gaussian fitting board EMP emission of experimental data for Ni(II) doped in CdS reveals that cubic crystal field may split due to reduced symmetry information; therefore, board emission happen in Ni doped CdS is due to two level emission and difficult to distinguish incomparison with Mn doped CdS nanostructure synthesized by VLS mechanism [107,109,113]. Figure 3e shows the single Ni and I; and coupled Ni+I doping in the host lattice resultant the inhomogeneous DMS structure. Figure 3f shows the ion doping related electronic structure of $CdS:NiI_2$ NB. EMP emission observed quite far in $CdS:NiI_2$ band edge emission is owing to high magnetic ion

concentration or defect formation in F or Cl during growth in VLS mechanism in the presence of hydrogen in source gas. Meanwhile, Br or I ion are heavy that might co-doped with Ni in the host lattice and exhibits strong lasing phenomena that will be detailed discuss in lasing section. Co-dopant ion in CdS lattice may lead formation of exciton complexes or acceptor/bound exciton or self-trap exciton as shown in Figure 3e of different exciton spatial distributions within the lattice [114,120].

High-density EMPs could polarize and combine with free exciton in 1D NB of CdS:Co, leading to coherent emission behavior at room temperature. EMP condensation in NB happens due to the following reasons: 1) spin coupled with exciton and phonon; 2) spin ion aggregation with FM coupling; 3) EMP is more stable than free exciton for material having higher exciton binding energy than thermal energy that coherent coupled through FM exchange interaction. 4) 2LO phonon along c-axis in hexagonal structure has large transition probability and strong polarizability to interact with exciton to favor the EMP state in TM ion doped semiconductors. Due to weak interactive force, highly stable spin-exciton-phonon (LO phonon) polarization may exhibit the bipolaron emission in PL spectra at high temperatures. Moreover, the much lighter effective mass of excitons than electrons in CdS:Co semiconductor exhibits the strong interaction between EMP condensation at critical temperature. Steady-state spectra exhibits the two-band emission near bandgap related with free exciton and EMP at room temperature as shown in Figure 3c for 1D NB of Co doped CdS. The second peak (518 nm) is very close to 2LO A1 phonon, which indicates that EMP formation close to band edge needs phonon polarization in the same direction. Therefore, the orientation dependent EMP collect free exciton to condensate EMP to produce lasing emission even at perpendicular direction. Such coherent EMP condensation to exhibits lasing in II-VI 1D structure need to be study under ns laser excitation for better understanding of exciton-exciton, exciton-electron, exciton-phonon and exciton-spin interaction with variable timescales [100,122]. The spectra line width and intensity strongly dependent on the excitation power of Co doped CdS. For threshold power of 7.4 uJ, linear increase in intensity due to inhomogeneous distribution of magnetic ion in belt. For threshold power of 16 uJ, lasing line width and intensity is not so wide due to exciton-carrier or exciton-phonon interaction that may involve lasing in single structure. Such random lasing in 1D structure is contingent on the exposed area that is quite helpful to understand the collective EMP lasing phenomena in doped wurzite microstructure [100,123]. The collective EMP condensation favored by the 1D longitudinal polarization and FM coupling of

magnetic ion detection at room temperature for better understanding of magnetic exciton BEC in DMS nanostructure. Exciton magnetic polaron states in 1D NB and NW appear by exchange interaction between spin-carrier interactions results in formation of EMPs. The overlapping tails of the carrier wavefunctions and spins form large cluster formations under high excitation density and respond as collective magnetic polarons to pronounce bosonic nature in NWs and NBs. Therefore, the collective EMP condensate by coherent light in nanostructures show the photo-magnetism behavior that increases possibility of modulating single-mode lasing by FM coupled with exciton in DMS. The large EMP coherence space and optical or magnetic modulation in 1D nano/microstructure of wide bandgap semiconductors need more study for nanophotonic applications for future devices applications [5].

3.1.2   CdSe

Direct bandgap (~1.74 eV) of cadmium selenide (CdSe) exhibits the n-type conductivity and possesses astonishing electronic and optoelectronic properties like other II-VI materials [10,83]. Wurzite structure is more stable than zinc blende and rock salt (normally obtained at high pressure [124–127]. Deng et al. successfully form the zinc blende NC at low cost and green reagents. 1D tubes CdSe nanostructures include NW, NB and NT have been reported with both physical and solution synthesis mechanism [127]. Dai et al. successfully controlled the shape of CdSe NCs during synthesis and demonstrated the elongated nanorods (NRs) for many interesting optical properties [128]. Kuno et al. reveal that the nanocrystallite emission originated from the surface related defect due to large surface-to-volume ratio [129]. However, the bandgap luminescence arise from optically inactive fine structure state or dark exciton. Meanwhile, Pan et al. reported the enhance luminescence spectra for CdSe NW and NBs synthesized by VLS mechanism [130]. 1D nanostructure is directed by well-confined structures which might results in high optical gain under high power and suitable for ultrafine red-color lasing. For 1D CdSe, excited electron in conduction band interact with phonon and fast decay in contrast with QDs of CdSe due to phonon bottom-neck effect [131,132]. Mirov and co-workers successfully doped TM ion in CdSe and others II-VI semiconductors for mid-IR Lasers [133]. II-VI semiconductors and related ternary alloy dopant sites for cubic structure occupied tetrahedral site and opposed to the octahedral site in the crystal symmetry. Tetrahedral site of crystal symmetry provide smaller crystal field splitting and transition emission into IR region due to dopant ion.

Transition metal ion related Luminescence behavior

To understand the lasing phenomena within CdSe matrix, one must know the spatial recombination through any spectroscopic measurement. CdSe NC has poor band edge emission mainly for two reasons; (i) optically inactive structure state at bottom of conduction band known as dark exciton and (ii) transition from these defect to the valence band. Interestingly, for 1D nanostructure CdSe synthesized by VLS mechanism has strong luminescence at high excitation that may high the population rate at lowest of conduction band. Alternatively, the high crystallinity obtained from VLS mechanism of hexagonal CdSe nanostructure that exhibits the red color lasing line of individual crystalline CdSe NB as reported by Pan [130,134,135]. Meanwhile, the size dependent and lateral thickness of CdSe nano-platelets tuned the LO-phonon corresponding to low exciton-phonon coupling, large oscillator strength and energy spacing of both. Optical transition energy related with exciton-phonon interaction in CdSe is controlled by lateral size and thickness by Achtshein [131]. CdSe platelets like structure are attractive for optoelectronic and permits us to control the exciton energy states by thickness but lateral dimension disparity in the LO-phonon coupling independently of thickness and lateral size.

Another major key feature of II-VI materials is that heavy anions in the crystal field offer low optical phonon energy cutoff value and decrement the efficiency of non-radiative decay. Such decrease in efficiency provide potential ability of high fluorescence yield at room temperature as shown in Figure 4a [133]. Yu et al. synthesized CdSe nanoplatelets and nanoribbons using solution process mechanism doped with Mn^{+2} ion as shown in Figure 4b [136]. TM ion doping in CdSe in low dimensional systems (NWs, nanoribbon, etc) exhibits the unique magneto-optical behavior characterized by various spectroscopic analysis. Mn^{+2} doping in CdSe exhibits the strong carrier-induced ferromagnetism due to sp-d exchange interaction between magnetic ion and electronic state of CdSe. Thus, quantum confinement at nanoscale provide more dominant of carrier-spin exchange interaction and opens new horizons for DMS community [137–141]. Mikulec and Erwin reported that the Mn^{+2} incorporation in ZnSe and CdS is comparatively more convenient then the CdSe matrix. The probability of Mn ion doping in CdSe matrix is 50% for bulk but for NC, it is still challenging [142,143]. Surface adsorption of magnetic ion impurity during nucleation process at nanoscale form the cluster formation known as the magic-sized cluster suitable for uniform doping in host crystal. For nanoscale or 1D nanostructure, reduced dimension result may increase possibility of quantum confinement and provide low probability of impurity ion adsorbed within

magic-sized cluster. Yu et al. successfully doped the Mn^{+2} ion within the CdSe NC as shown in Figure 4b [136,144]. Magnetic ion doping in magic-sized cluster formation at nucleation stage of growth provide uniform doping concentration in host semiconductor. Cu^{+2}, Ag^{+2} and other TM ion successfully doped in NC exhibits red-shift broadband emission at room temperature. Pan et al. prepared the hexagonal CdSe NWs and NBs like structure with CVD method that exhibits the red-color lasing within individual nanostructure [130]. Chen et al. also prepared the 1D nanostructure of CdSe by CVD method that exhibits the strong excitonic behavior under different temperature as shown in Figure 4c-e [145]. Temperature dependent absorption spectra at 10 k show strong emission spectra of exciton peak (1.8248 eV) and free exciton peak coincide with LO phonon (1.8515 eV) of CdSe NWs. Due to lattice expansion, low temperature mapping of CdSe NWs strongly exhibits the exciton-phonon interaction. According to Bose-Einstein approximation, the exciton-phonon interaction function of temperature and low temperature variation is quite helpful to analyzing the thermal expansion and exciton-phonon interaction due to bandgap shrinkage. Similarly, the temperature dependent luminescence spectra represents the increases in the intensity at low temperature and inset image of Figure 4e show the difference in activation energy (5.40 eV and 18 meV) as calculated by dual activation energy model; while the energy 18 meV is comparable with bulk exciton energy [145,146]. From crystal field theory, the ground state of Cr^{+2} ion is 5d to upper levels in visible spectrum. Tetrahedral site of crystal field (T_d) splits 5d into triplet ($^5T_2$) and duplet (^5E) states. For Cr^{+2}, the triplet state allow the transition between levels and allowed spin state; while, Fe^{+2} duplet state allow the transition in host matrix. Therefore, Cr^{+2} ions make transition from ^5E (5d) to $^5T_2$ (5d) which is promising for Laser application. John-Teller mechanism and spin-orbital coupling are also responsible for energy splitting. Numerous reports available for Cr^{+2} doped in CdSe exhibits the direct lasing at room temperature. Similarly, Chen et al. show the change in the excitation density will enhance the spontaneous emission; therefore, multiple peaks appears at 715 nm and 725 nm (above threshold value of 0.296 MW cm^{-2}) at room temperature. These multimode random lasing in single structure of CdSe NW in NIR region make it suitable for NIR optoelectronic application such as sensor, laser and energy conversion devices [133,147,148].
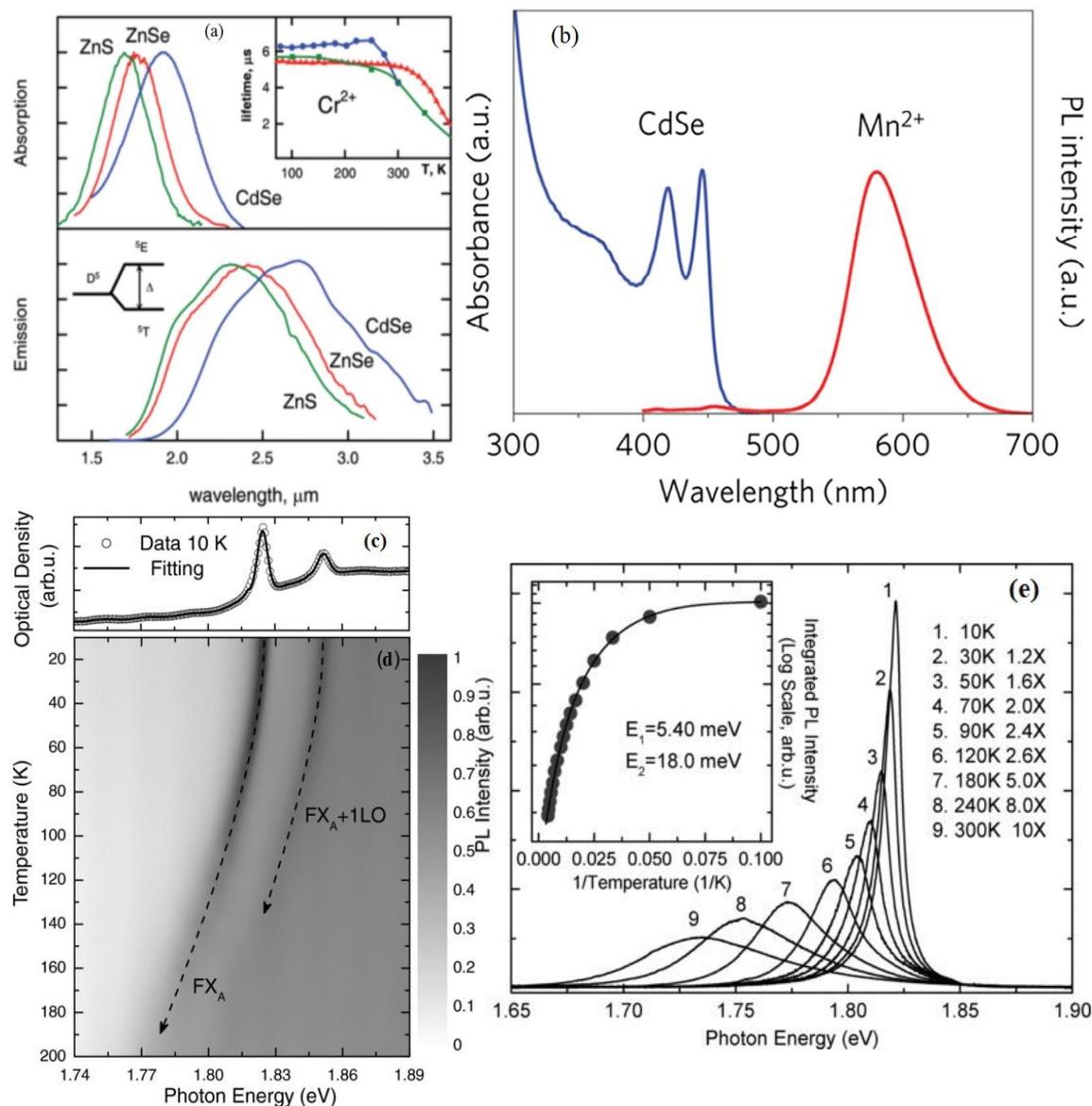
Materials Advances Accepted Manuscript

Figure 4: (a) Normalized room temperature absorption and emission-gain spectra of Cr^{+2} ions in ZnS, ZnSe, and CdSe crystals. Insert shows temperature dependences of Cr^{+2} ions lifetimes in ZnS (circle), ZnSe (triangle), and CdSe (square) crystals; Copyright © 2010 Wiley InterScience [133]. (b) The absorption (blue line) and PL (red line) spectra of Mn-doped CdSe NPLs; Copyright © 2009 Springer Nature [136]. (c) Low temperature (10 K) free-exciton absorption of CdSe NWs. The solid curve is the multi-Gaussian fitting of the absorption spectrum (d) Temperature-dependent mapping of the absorption spectrum. (e) The free-exciton emission of CdSe NWs at various temperatures. The inset plots the dependence of the integrated PL intensity on the reciprocal of temperature, and the solid curve is the Arrhenius fit with two activation energies, Copyright © 2011 Wiley [145].

Solution process colloidal QD exhibits the exciton and bi-exciton lasing at room temperature. Spectral symmetric PL is temporally integrating streak image over nanosecond fitted by pseudo-Voigt function for low and high fluence provide information related to exciton and bi-exciton transition. Giant oscillator strength near band edge emission has strong coherent phasing strength as correlated with single atom in host matrix. Therefore, the ultrafast dynamics spectroscopy provide detailed information of carrier and decay kinetic in picosecond ps time domain, The bi-exciton lifetime of CdSe matrix is dominated by non-radiative Auger recombination up to 10 ns, almost the two order of magnitude larger than measured radiative lifetime. Streak camera images of CdSe CQ Well excited with 1 kHz, 70 fs laser pulses, fluence of 20 uJ cm^{-2} of ultrafast time decay measurement value about ~10 ps, and unambiguously assigns the peak to stimulated emission provide evidence of intensity dependent spectra originated from bi-exciton transition within respective energy position at ultralow threshold fluence [149].

3.1.3 CdTe

Like other II-VI semiconductors, CdTe exhibits strong luminescence behavior and is an attractive material for various optoelectronic applications such as solar cell, photodetector, lasing, etc. CdTe is direct bandgap (1.45 eV) semiconductor inherently p-type conductivity due to presence of Cd vacancies, while others CdS and CdSe are n-type conductivity [150–152]. Tang et al. reported the spontaneous organization of CdTe NW from NPs due to strong dipole-dipole interaction [152]. Neretina et al. formed vertically aligned CdTe NWs synthesized through catalytically driven grown method [153]. Hiesinger et al. studied both n-type and p-type CdTe excitation spectra of exciton luminescence at 2k [154]. For n-CdTe, the two peaks line appears at 1.59375 eV and 1.59320 eV belong to exciton bound to a neutral donor (D^o, X). Emission peaks at 1.5919 eV and 1.5893 eV are originated from exciton bound to an ionized donor (D^+, X) and exciton bound to neutral acceptor (A^o, X). While, in p-type CdTe, all these emission line appears more strongly with two other emission lines at 1.5896 eV and 1.5898 eV replica of exciton bound to neutral acceptor (A^o, X). For n-CdTe, the weak bands from 1.596 to 1.598 eV are assigned as spin-triplet exciton also called lower branch polariton (LBP) and upper polariton branch (UPB) of free exciton, respectively. Higher energy emission at 1.6031 eV is related with n=2 excited state of free exciton; while the low energy onset shows the 1LO phonon sideband at 1.5747 eV. At 20.6 k, the 8LO phonons peaks appears with background but for 1.8 K, the exciton coincides with low energy

threshold field to rise the value at low temperature. For p-type CdTe, LO phonons peaks appears with lower intensity than n-CdTe with two additional peak. As, the temperature reaches below 20 k, these two additional peaks due to neutral acceptor (A^o, X) disappeared between the oscillatory structures.

Transition metal ion related Luminescence behavior

Various researchers have extensively reported the TM ion doping in CdTe for DMS and optoelectronics applications such as solar cell. TM ion doping in II-VI materials related with 4d element effect on both optical and electrical properties. Kurchatov and others research reported the successfully incorporation of TM ion within II-VI host matrix that exhibits the IR lasing emission at room temperature [155–157]. Lafuente-Sampietro et al. reported the resonant optical control of the spin (single Cr atom) in CdTe/ZnTe QD [158,159]. At 5k, the Cr spin relaxation has been observed by strong resonant laser field, which is responsible for Cr atom tuning optical stark effect. The circular polarized PL spectra of magnetic anisotropy of Cr spin induced by biaxial strain. The exchange interaction between spin atom and exciton further split the Cr energy level due to high polarizability of crystal field. For carrier dynamics understanding in CdTe/ZnTe QD doped with Cr atom in pump probe experiment was performed to observe the relaxation time and non-equilibrium distribution of Cr spin population with circularly polarized resonant pump pulse. Peak intensity map of Cr doped in CdTe/ZnTe QD show the low energy bright exciton state and dark exciton. Cr ion interaction with phonon within the system show strong spin-phonon coupling at low temperature, which is an important step forward to control the TM ion coherent spin for future spintronic device [158,160]. Similarly, Cr spin is coupled with exciton near valance band and show the Nano-magnetic behavior due to optical pumping of electron-Cr and hole-Cr. Resonance and non-resonance optical pumping can directly use as the spin memory (write and erase). Therefore, the spin channel can be studied with polarized emission that respond to relaxation channel of Cr ion in II-VI semiconductors. Therefore, optical pumping and power dependent PL intensity related temperature effect is directly affected the hole-Cr spin near valance band and electron-Cr local generation of phonons.

Optical pumping show the positive charges exciton and relaxation of Mn-spin exchange coupled with confined hole spin in CdTe. Such spin can be observed under optical injection of spin-polarized carriers with time domain of few tens of ns. Interestingly, the localized spin state can be

controlled by charge state of strain-free QDs. So, magnetic anisotropic of atom can be controlled by electrical field make it suitable for miniaturized data storage application for fine structure and strain-free QDs. Such fine structure show the spin splitting of Mn ion within few meV energy ranges coupled with heavy-hole spin near the valance band of CdTe. Pumping and magnetic influence the Mn-electron dynamics in excited state and Mn-hole in ground state. For zero magnetic field, spin-relaxation time of Mn-hole is shorter due to valance band mixing [157,159–161]. PL time delay measurement further explain the dynamics of charge carrier interaction with optically active injection of spin polarized photo-carriers. Similarly, Mn doped in CdTe QD show the spin flip under resonant excitation mainly controlled by the carrier-spin interaction. Such coherent dynamics is directly observed in ultrafast time domain and localized the spin ion in CdTe matrix [157,159–161]. Bose-Einstein condensation (BEC) of exciton-polaritons related phase transition related to quantum effect in CdTe/CdMgTe microcavity at 5k [162]. Spontaneous quantum degeneracy of polaritons in CdTe microcavity excited by non-resonant pumping significantly narrowing the polariton emission line width. The condensation of exciton polaritons in a CdTe-based microcavity condensation is not standard BEC due to leakage in cavity. The polaritons are non-interaction as boson but not follow the conservation law above some critical density under specific temperature. Spatial coherence and macroscopic polarization through condensation can be used as polariton-laser in CdTe. Thus, for wide bandgap semiconductors such as ZnO or GaN, the polariton condensation build-up macroscopic polarization and spatial coherence for polariton laser with increase in temperature [162–165].

3.1.4 Ternary Alloy of Cadmium chalcogenides (CdX; X=S, Se, Te)

II-VI semiconductor excitonic emission can be easily observed at room temperature due to their exciton binding energy is higher than thermal energy. Therefore, many researchers have established optically pumped stimulate emissions of II–VI semiconductor and their alloy from 1D nanostructures. Secondly, the low threshold within low dimension II-VI semiconductor stimulates the excitonic emission that is a prerequisite for lasing at room temperature. Thirdly, the optical cavity formation in 1D nanostructure (whispering gallery or Fabry–Perot mode lasing) enable to achieve the lasing action [166–169]. For ternary alloy have advantages over binary semiconductor of wavelength/bandgap tunability of multi-color lasing as reported in both Zn and Cd chalcogenides. Tunable emission from UV to visible to NIR from Zn and Cd chalcogenides 1D structures has

been demonstrated from different synthesized mechanisms such as VLS, VS, solution process and etc [77,170–172]. Moreover, the TM ion doping in II-VI semiconductor matrix also exhibits lasing phenomena; therefore, the existence of lasing often comes exciton-exciton interaction, electron-hole plasma and exciton-polariton near their bandgap. CdS doped with NiI has formed $(NiS)_x$ and NiI_2 cluster in 1D NB exhibiting the dual lasing line in single structure at room temperature. Another important factor is excitation area exposure that show the lasing threshold in single structure in all directions as observed in CdSe nanostructure [116,122,173–175].

Cd based ternary alloy $CdSe_xS_{1-x}$ NW with homogenous composition has been synthesized through solution-liquid-solid process by Yang and co-workers [58,176]. Ternary alloy nanostructure gain enormous attention owing to continuous tunable bandgap which make it suitable for various electrical and optical applications such as photodetectors, solar cell, FETs, etc. Rosenthal et al. reported the ternary NC of $CdSe_xS_{1-x}$ having different sizes and compositions; results indicate that surface states strongly correlated to the relaxation process of photo-excited carriers studied by ultrafast fluorescence upconversion spectroscopy [176–178]. Colloidal $CdSe_xS_{1-x}$ NWs exhibits strong emission tuned from 508 nm to 628 nm with narrow spectral width along with high quantum yield. Therefore, tunable and polarized emission of $CdSe_xS_{1-x}$ NWs provides greater sight to understand the exciton dynamics for various optical applications as shown in Figure 5a-d. Figure 5a, c shows the absorption and PL spectra of $CdSe_xS_{1-x}$ alloy NWs, where variation in composition gradient shows redshift in bandgap tuning with increased in Se ratio. Similar studied conduct for $CdSe_xS_{1-x}$ alloy NWs synthesized by CVD, NCs and quantum dots (QDs) [170,179–182]. At low temperature PL, defect related emission of different composition has been suppressed except for CdSe and $CdSe_{0.25}S_{0.75}$ indicate that alloy formation of $CdSe_xS_{1-x}$ NWs can be feasible for high quality polarized LEDs as shown in Figure 5f. Spectral broadening of emission can be related with (i) inhomogeneous broadening (ii) optical phonon interaction and (iii) acoustic phonon interaction at low temperature; while the bandwidth broadening can be related with (i) acoustic phonon scattering (ii) longitudinal optical (LO) phonon scattering and (iii) exciton surface scattering. Below 130k, for CdSe and $CdSe0._{25}S0._{75}$ acoustics phonons contribute significantly (dotted line comes from inhomogeneous broadening and acoustics phonon scattering) but above 130 K, the LO phonon and surface phonon contribute more effectively and reason for band width broadening as shown in Figure 5e. From the luminescence spectra, we can understand the recombination dynamics of photo generated carriers with the help of schematic diagram (Figure 5g). Process can

be ascribed as (i) photoinduced exciton can localize in the valleys, (ii) radiative recombination, (iii) photoinduced excitons, (iv) surface defect and (v) trapped electrons recombine with trapped holes to give defect related emission. However, both compositional gradient of alloy and nanoscale dimension strongly influence the exciton recombination due to surface induced quantum confinement as reported in different studied [183–186]. Therefore, the PL decay measurement become the effective tool to analysis the recombination process under very low excitation power. $CdSe_xS_{1-x}$ ternary alloy reported by Pan's and other research groups by using CVD route as shown in Figure 5h-k [75,77,179]. Liu's and co-workers also reported the $CdSe_xS_{1-x}$ alloy NWs for various application such as sensor, thermoelectric (Figure 5l-o), wave-guide and photodetector in recent years [187–189]. As, the ternary alloy of II-VI semiconductor or heterostructures are important for bandgap engineering but also radial core/shell nanostructures are also gain attention due to their special structure characteristic and having miscellaneous applications such as field-effect transistors, solar cells, biomedical applications, and memory devices [25,69–71,190]. For Type-II heterostructure of CdSeTe, wurzite (CdSe) and zinc blende cubic (CdSe) structure can be achieved by the controlling the temperature and ligand. Moreover, the Se and Te content in heterostructure tune the bandgap relation emission; diameter and shape of tetrapod demonstrate the change in emission linewidth [191]. Low-threshold lasing for CdTe at the surface of core of NW or NC exhibits the strong lasing emission line. Colloidal Type-II (CdSe/CdTe) heterostructure has minimal overlap of e-h wave function at interface that intensifies the amplified spontaneous emission with high density of charge transfer effect and exhibits the strong lasing at lower threshold value [192]. Interfacial of Type-II heterostructure longer the Auger recombination lifetime support the continued lasing and decrease in oscillator strength between electron and hole will intensify the optical gain for LED and laser applications. Transient absorption show the multiple oscillation at high pump power assigned to acoustic phonon normally observed in single metal nanostructures with quality factor of 9-10. Inhomogeneity of CdTe NWs lead to the result of the different charge carrier and charge trapping related to surface and pump power [193].
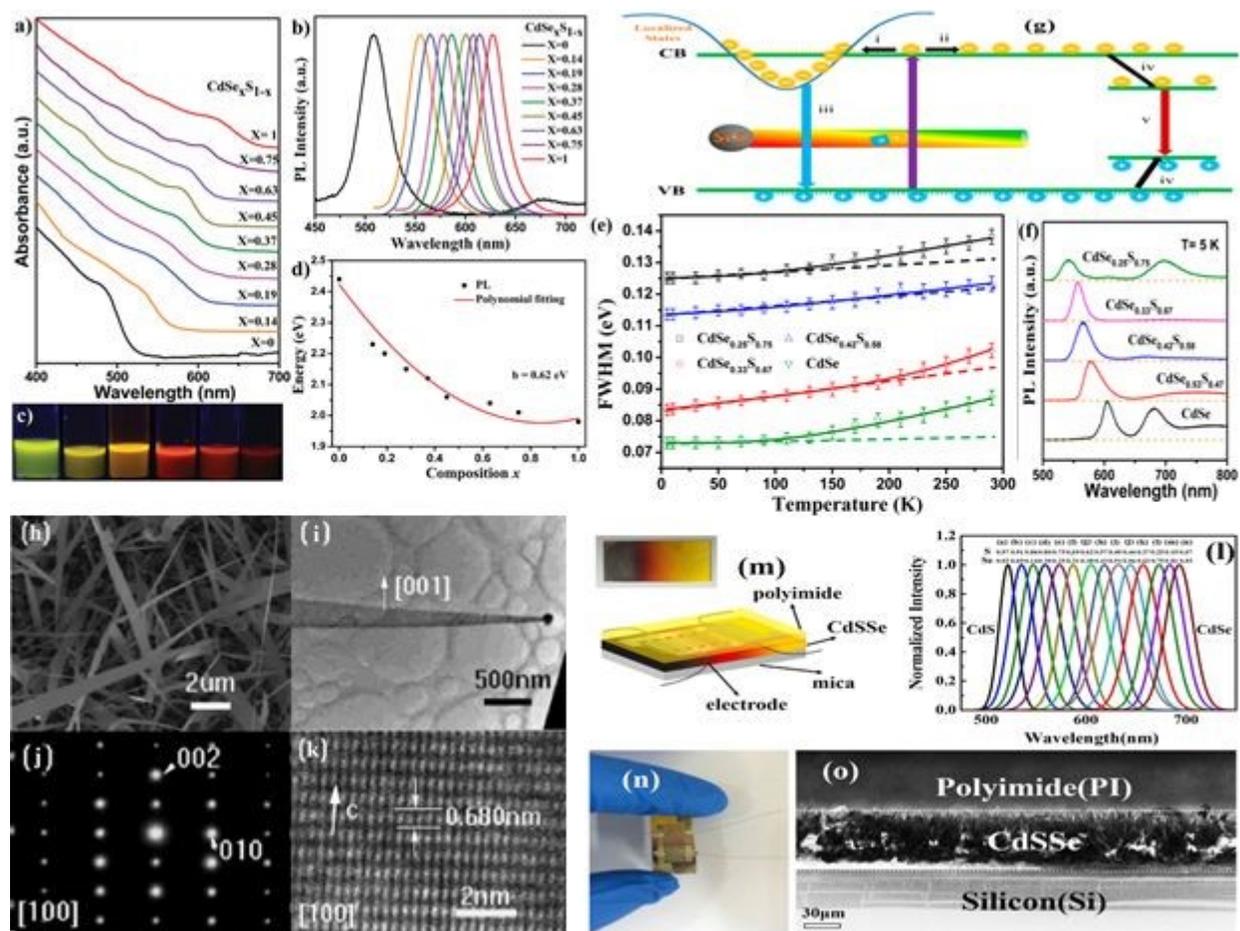
Figure 5: (a) UV–vis absorption spectra of CdS_xSe_{1-x} prepared by solution process; b) PL spectra of the CdS_xSe_{1-x} NWs with different Se content. c) Photographs of typical emission colors from the obtained alloyed NWs under UV 365 nm irradiation. d) Energy gap–composition correlation of CdS_xSe_{1-x} NWs, where the data points represent the value extracted from their respective PL [176]. (e) The solid lines are fits using the Varshni law and exciton–phonon model temperature dependent, while dotted line represent the inhomogeneous broadening and the acoustic phonon scattering. (f) PL spectra of compositions varied alloyed NWs at 5 K; (g) Schematic of the kinetic model of exciton recombination in NWs [58]. (h) SEM morphology of ternary CdS_xSe_{1-x} NBs synthesized by CVD (i) TEM image; (j and k) its selected area electron diffraction (SAED) pattern and HRTEM image, respectively [70]. (l) PL spectra measured at different composition along the length direction of the CdSSe NW (m) Real-color photograph of $CdS_{1-x}Se_x$ chip and the diagram of the sweat sensor and (n) Real image of the as-prepared sweat sensor. (o) Cross-sectional SEM image of PI-coated CdSSe NW chip [188].

Pan et al. synthesized the axial NW like structure of CdS/CdSSe via VLS mechanism. Pumping fluence exhibits two broad emission at 520 nm (green emission) and 600 nm (red emission) at low pump power of 29 μJcm^{-2} corresponding to spontaneous emission. Both emission show sharp bandwidth of 0.4 nm at high power show the stimulated emission in heterostructure. Moreover, the slightly blue shift at power corresponding to electron-hole plasma formation at surface contributes to the exciton-phonon scattering and redshift due to bandgap renormalization effect [75,77]. Guo et al. synthesized high-quality ternary alloy of $CdS_{1-x}Se_x$ Nanotripods for broadband tunable single mode lasing for high integration optical circuit and photonics communication [173]. Various factors such as compositional variation and diameter of tripod related cavity became the prominent to tune the band gap of $CdS_{1-x}Se_x$ and single-mode lasing. Therefore, the tunable wavelength has tremendous application such as wavelength-converted devices, nanophotonic laser and optical communication on signal chip [123,194,195]. Yang et al. also reported the bandgap tuning of colloidal NWs of $CdSe_xS_{1-x}$ as synthesized by solution process. At low temperature, PL show the surface defect related emission corresponding to exciton and localization states related with compositional ratio of NW. Therefore, the more carriers localized in these states and do not move to the surface that possible enhance the radiative recombination of ternary alloy.

CdS/SnS_2 superlattice microwire synthesized by CVD show multiple emission modulate by exciton and photons in 1D system. The physical deposition method successfully achieves strong lasing for multicolor emission at low threshold value. Novel multi-peak emission with controllable periods first time due to contribution of 1D photonics crystal and periodical exciton confinement [58,176]. Sn doping in CdS not only tune the bandgap emission but also change the defect related emission line. Peng et al. also observed the strong electron-phonon coupling interaction in optical micro-cavity based CdS-Sn related with carrier interaction, trapping and recombination for 1D nanostructures [196]. Tian et al. show the quantum confinement on polarization anisotropy emission in CdS-Sn micro-cones like structures. Polarization ratio achieved up to 60 % providing suitable information about the quantum confinement and optical confinement in nanostructures related with dielectric contrast with Sn incorporation in CdS matrix. As, the cross-section radius of nanostructures scaled down related with Sn doping and reduction of carrier lifetime. Moreover, the polarization ratio of magnetic ion or spin ion corresponding to dielectric that will help us to study the spintronics devices at room temperature [123,197,198]. Bao et al. reported the single mode laser of CdS NW channel on chip SiN waveguide with high efficiency up to 58 % by evanescent

coupling. Composition gradient demonstrate the various emission color from green to red; while the lasing emission wavelength range from 520 nm to 738 nm provide broad wavelength tripod lasers [199]. Li et al. reported the multiphoton pump lasing of bi-exciton from solution of colloidal CdSe/CdS nanoplatelets [200]. Colloidal solution show an optimal lateral size that minimize the ultralow threshold for lasing at room temperature. The CdTe alloy with other optical active material such as CdSe as Type-II semiconductor tetrapod structure or ZnTe exhibits the strong optical response and useful for various optoelectronic applications. 1D NW of CdS/CdSTe/CdTe show high optical responsivity due to n-type and p-type characteristic of CdS and CdTe. CdSTe act as depletion layer similar to intrinsic Silicon act as sandwitch in PIN photodetector. The light illumination will transfer the photoelectrons from CdTe to CdS and hole transfer from CdS to CdSTe simultaneously and then to CdTe layer's shell. CdSTe layer reduces the carrier recombination probability and increases the photocurrent, make it suitable for photodetection in wide spectral range [201,202].

Figure 6 a-b show the lasing in CdS NBs co-doped with Co(II) 0.1–0.68 % as prepared by CVD. The two-band emission near the band-edge located at the 508–510 nm (FX) and at the 518–525 nm for the EMP at room temperature. The YAG:Nd (355 nm using 2 ns laser) show the lasing line at 518 nm (Figure 6a). Figure 6b show the line width and intensity as the function of excitation power. Beyond the threshold power of 7.4 µj, we can see a super-linear increase of the emission intensity. Regardless of the inhomogeneous distribution of the dopant ions in NBs, a single lasing mode always happens at the EMP location. Over 6 µj, the exiton–carrier or phonon interactions start and to be involved in lasing process. The Co(II) ions with a ferromagnetic coupling provide significant carriers and driving forces to complete this collective emission processes as observed in others II-VI semiconductors. Others II-VI semiconductor doped with TM ion as excited by fs laser exhibits the EMP lasing line, whereas CdS:Co NBs show lasing with both ns and fs lasers. This difference indicates that the EMP in the latter should have a larger coherence length and coherence time because ns laser excitation can cover more microscopic interactions, such as exciton–exciton, exciton–phonon, exciton–carrier, and exciton–spin, inside the excitation zone, while these interactions usually exist in variable time scales [3].
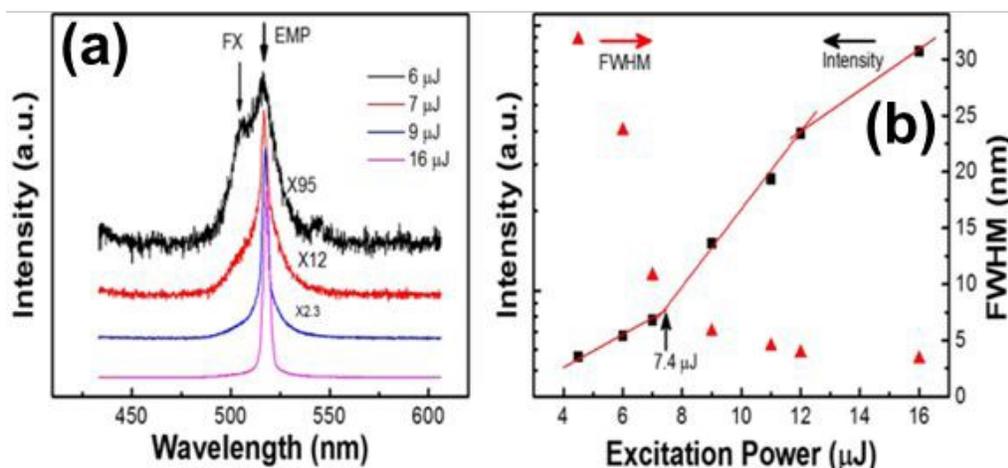
Figure 6: (a) PL spectra from spontaneous emission to stimulated emission when excited by nanosecond pulse laser (355 nm). The PL emission intensity and fwhm is extracted and plotted as a function of pumping power. (b) When the excitation intensity was below the threshold, a broad spontaneous emission band was observed which shows a linear increase with excitation power, while the pumping power was larger than the threshold, the emission intensity showed a superlinear increase with the excitation power. Moreover, the width at half-maximum (fwhm) become narrower when increasing the pumping power Copyright © 2016 ACS publication [3].

Type-II interface of ZnTe/CdSe reveals significant blue shift toward lower energy band, whereas the high-energy band is related with CdSe. The relative small lattice difference between two semiconductor core-shell nanostructures with high surface-to-volume ratio is suitable for photovoltaic application [171,190,203]. Wang et al. demonstrate the CdSe/CdS/ZnS QDs with spherical optical cavity propagated the light around the circumference due to ZnS shell at room temperature [204]. The ratio of S:Se in CdSeS NW can be controlled by exciton dynamics along with bandgap tuning as measured by fs transient absorption spectroscopy. Lifetime measurement show the shorter with increase in Se ratio; while, increase in S ratio reveals large redshift in steady state absorption. Short time about 10 ps with increase in Se ratio also reveals the photo-bleaching recovery from 8.4 % to 57.7 %, which make the 1D NW of CdSSe suitable for photovoltaics and optoelectronics application with good control on both optical and excited state properties. Homogeneity of alloy depend on phonon frequencies of atomic mass of atom in unit cell and lattice configuration. Changing in S:Se ratio exhibits the linear shift of Raman bands of LO phonon frequency to higher or lower wavenumber. Raman band of CdS and CdSe show the homogenous

distribution of Se and S atom in QDs along with new Raman bands between LO phonon frequency show the breaking of translation invariance of lattice. Additional vibrational peaks show the isotope mixture near zone center of optical mode correlate with linear frequency-mass dependency in crystal system [170,182,183,205–207]. For QDs, the size dependence broadening in Raman lines due to phonon confinement; while, the weak confinement and narrow bandwidth distribution show the sharp Raman line due to uniform or homogeneous distribution of precursors.

3.2 TM ion doping in Zinc chalcogenides (ZnX; X=O, S, Se, Te)

3.2.1   ZnSe

ZnSe is an important II-VI semiconductor used in various optoelectronic applications such as nonlinear optical devices, LEDs, FETs, panel displays and many others. 1D nanostructure of ZnSe become more attractive sue to their unique optical, electrical and thermal properties due to dimension reduction. 1D nanostructure of ZnSe has been grown by vapor liquid solid mechanism and solution process method to attain different type of 1D structures such as NW, NR, NB, NT, core/shell, bi-axial, tetrapod and alloyed. Various researchers reported the 1D growth of ZnSe by using various physical and chemical route mechanism [21,208–210]. Li et al. reported the size dependent periodically twinned ZnSe NWs by catalytic growth in CVD; whereas oriented arrays of ZnSe NR was obtained by Zhang et al. by using MOCVD [210,211]. Wang et al. prepared the epitaxial 1D growth of ZnSe NWs by MBE on GaAs substrate [212]. ZnSe zinc blende QD converted into hexagonal wurtzite 1D NWs through oriented attachment of NC. TM ion doping in 1D ZnSe also show excellent optical response and is extensively studied by various research groups [213–216].

Transition metal ion related Luminescence behavior

Figure 7 shows the PL spectra of different TM ion doping (Mn^{+2}, Ni^{+2}, Co^{+2}, Fe^{+3}) in ZnSe nanostructure [20,117,213,216]. Mn doped in ZnSe nanostructure synthesized by VLS mechanism and solution process as reported by many researchers [20,217–219]. Figure 7a show the Mn doped ZnSe nanoribbon; emission spectra at 461 nm assigned to near band edge emission at room temperature. At 77 k, the peaks split into two originated from free exciton and EMP. Emission peaks at 534 nm and 646 nm correspond to the low energy side and high energy side of d-d transition (D1) originated from $^4T_1(^4G) \rightarrow ^6A_1(^6s)$ in Mn-doped ZnSe. Peak emission at 585 nm is related to d-d transition. The d-d transition of Mn in ZnSe is extensively reported in other II-VI semiconductors. For ZnSe as host matrix, Mn originated at 534 nm and 650 nm corresponding to the following: (i)

Mn-Mn ions aggregate together to form AFM coupling (ii) self-activation of V_{zn} –Cl_{Se} complexes due to Mn doping (iii) direct coupling of FM Mn-Mn pairs (iv) surface trap states. Therefore, the structural relaxation are involved in optical emission of Mn-Mn interaction pair in ZnSe host matrix, crystal field and crystal lattice distortion to show the both FM and AFM pairs in the same zone. Therefore, low temperature PL provides sufficient information about the origin of emission spectra related to Mn-Mn interaction in host material. Peak emission at 533 nm, 580 nm and 664 nm at 77 k show ZnSe emission related to d-d transition and small redshift is due to sp-d hybridization effect. Figure 7b Fe^{+3} doped ZnSe nanoribbon synthesized by VLS mechanism show three emission spectra at 467 nm, 553 nm and 630 nm [213]. Peak at 467 nm assigned as band edge peak as observed in Mn doped ZnSe (461 nm; Figure 7a). Peak emission at 553 nm and 630 nm corresponds to second (D1) and third (D2) emission peak related to Fe^{+3} d-d transition. Moreover, the emission spectra abound 467 nm under different excitation correspond to redshift with increase in intensity sue to following reasons (i) bound exciton (ii) EMP interaction and (iii) e-h plasma formation at the surface. For low power, the bound exciton peak is dominant, further increase in power red shift in spectra and increase in intensity due to EMP. Further increase in spectra, the emission spectra reaches at 493 nm due to e-h plasma formation at the surface of nanoribbon related with excess charge of Fe^{+3}. Therefore, the low temperature luminescence and lifetime measurement provide suitable information about the emission spectra in host matrix as also studied by different groups [220–224].
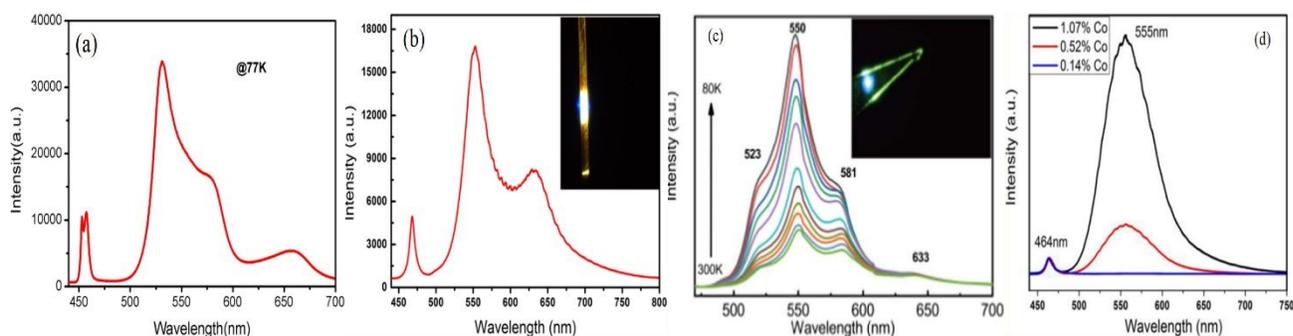

Figure 7: Transition metal ion doping in ZnSe matrix (a) Temperature-dependent PL spectrum of Mn-doped ZnSe nanoribbons excited with a cw laser (405 nm) at 77 K, Copyright © 2020 IOP publishing [20]. (b) PL spectrum of an individual Fe doped ZnSe nanoribbon with a 405 nm laser at excitation. The inset in the top right corner is the PL image of the nanoribbon in the dark field observation, Copyright © 2017 Applied Science [213]. (c) Temperature dependence of the near-band-

edge luminescence peak (FXs, EMPs) of NiI_2-doped ZnSe NBs from 300 K to 80 K at relatively high (1.2%) doping concentration, Copyright © 2021 IOP publishing [117]. (d) The PL emission spectra measured at room temperature with different concentration of Co doped ZnSe NRs, Copyright © 2021 IOP publishing [216].

Figure 7c show the emission spectra of Ni doped ZnSe under different temperatures [117]. At 300 k, the two emission spectra appear at 463 nm and 471 nm that are assigned to bound exciton and EMP as discuss for Mn^{+2} and Fe^{+3} doped ZnSe [225–228]. At low temperature the shoulder peak at 453 nm appears due to incorporation of Ni ions; combination of free exciton with AFM coupling with Ni ion or cluster show the formation of this peak rarely reported in magnetically doped semiconductors [214,229–231]. Hou reported that the TM incorporation in ZnSe reveals the origin of ferromagnetism, which may lead to the red shift in emission spectra. However, AFM coupling may lead the blue shift in emission spectra as coupled with d-d transition. Normally AFM coupling appears at high doping ratio with bound exciton but with low doping is rarely reported. Other research on Ni doped ZnSe also reveals the importance of DMS for future spintronics [232–234]. Figure 7d shows the Co doped in ZnSe by Zou et al prepared by VLS mechanism; emission spectra show anomalous nonlinear optical behavior due to magnetic ion incorporation in ZnSe nanoribbon like structure. From the PL emission spectra, Co doping concentration change form 0.14% to 1.07%. As, the doping concentration increase, the peak at 555 nm also is enhanced due to Co-Co coupling. Thereby, the intra-shell noted with high d-d transition that is responsible for FM coupling of TM ion pair, which may produce the nonlinear optical absorption. Moreover, the intensity ratio of band edge emission and d-d transition can tuned the visual emission under different doping ratio normally reported in NC [235–238].

Lasing is attributed in pure ZnSe near to band edge emission, which is sharp due to coherent transition without thermal distribution. Similarly, Mn doped ZnSe spectra also exhibits the lasing under different pump power and inset is the relationship excitation power and intensity. As, the excitation power increase, intensity ratio is also increase in nanostructure that exhibits the lasing in doped sample. Normally, II-VI semiconductor doped with TM ion exhibits the lasing in NIR [133,155,239–241]. In addition, various research reported the lasing in owing to exciton-polariton within the microcavity formation within the structure during growth or wurtzite structure [91,162]. For Mn doped ZnSe NW, the emission spectra two peaks attributed at 466.8 nm and 472.5 nm is assigned

to bound exciton band edge emission and phonon assisted exciton transition. Phonon assisted exciton transition is possible, when the exciton and phonon are coherent space or density of states and same polarization that may lead the formation of spontaneous polariton-exciton related emission. For belt like structure, the polariton-exciton emission is reported at 475 nm with board emission at 650 nm related to trapped state emission [242]. For ZnSe:Ni nanoribbon, the free exciton lasing emission is dominant at low excitation power, as the excitation power increase the EMP peak begin to increase and sharp anomalously. Such anomalous behavior in ZnSe:Ni doped is owing to nonlinear of EMP related lasing interaction with spin, LO phonon and exciton polarized in the same direction [117,230].

3.2.2 ZnS

ZnS is a wide bandgap semiconductor normally existence in cubic zinc blende (3.72 eV) and hexagonal wurtzite (3.77 eV) phases as room temperature. Wide bandgap and optical active make it potential candidate for various application such as flat panel display, LED, sensor, Laser and many others. 1D nanostructure of ZnS has been synthesized by both physical and chemical method that is extensively used is various application [243–245]. Meng and co-workers synthesized ultrafine ZnS NW using vapor phase growth in the presence of Au as catalyst [246]. By controlling the substrate temperature, gold thickness define the average diameter of ZnS NW ranging from 10-20 nm. Highly density 1D ZnS NWs grow on anodic alumina oxide (AAO) templates by Ding et al.; luminescence spectra reveals the stimulated emission originated from the narrow resonant cavity modes [247]. Wang et al. detail explained the different morphology of 1D nanostructure of ZnS prepared by using vapor phase mechanism [204,248,249]. Moreover, solution process application is in various light emission device such as flat panel, LED and biosensors [18,21,245,249]. TM ion doping in ZnS nanostructure has been reported by various groups via both chemical and physical method [250–253]. ZnS structures show the high transmission in the visible spectrum and large excitonic binding energy of 40 meV makes it significant material for photonic and optoelectronic applications [21]. Xiong group reported the high crystalline wurzite phase ZnS NWs synthesized by VLS mechanism [251]. At 10K, the bandgap emission becomes more dominant with weaker defect luminescence. For wurzite structure, the spin-orbital interaction and splitting of crystal field near valance band distribute the exciton energies into three bands (named as A (FXA), B (FXB) and C (FXC)) having split energy among them is 89 meV (FXC-FXB) and 57 meV (FXB-FXA),

respectively. In luminescence spectra, the FXA and FXB clearly observed at room and low temperature; for FXC not observed at room temperature due to fast decay time. Excitation intensity show the clearly change in relative intensity of exciton and defect related emission due to difference in their density of state. Therefore, the FXA and FXB show the red-shift effect (8 meV and 12 meV) with increase in excitation but defect insensitive to photon flux and saturate. Such shift in exciton emission is due to laser heating effect in 1D nanostructure; thereby no change with laser excitation is related with shallow level emission rather than shallow donor-bound exciton [254,255]. For heterojunction ZnS/CdS QDs, trap carrier across the barrier exhibits the two activation energy are 18 and 300 meV, that is responsible for lasing due to ZnS shell act as spherical optical cavity; which make possible transition from linear to nonlinear tendency at room temperature. The temperature gradient show that (i) single structure has less impurity or defect (such as Zn vacancy and S interstitial) and (ii) thermal broadening of exciton peaks represent the exciton-phonon interaction. Above 120 k, inhomogeneous broadening is owing to acoustic-phonon interaction and below 120 k, LO phonon responsible for inhomogeneous broadening (Bose-Einstein condensation fitting). The exciton transition in ZnS matrix and coupling strength of exciton-LO phonon is directly determined from the broadening of exciton peak energy and width. Such stable and high crystalline NWs are promising material for high efficient LED and Laser in UV range [251].

Transition metal ion related Luminescence behavior

ZnS NW doped with Cr ion total energy calculated for both spin and non-spin polarized states as shown in Figure 8(a–c). Cr (II) interact with the nearest neighbor S atom by replacing the Zn ion. The p-d hybridization between Cr and S comes from d-state and p-states show the small magnetization. From the spin density of states or distribution of Cr ion in ZnS NW show the large contribution of dopant ion to total magnetization in opposite direction favors the AFM interaction. From the Bader Charge (BC) analysis of bond length and charge transfer supports that doped NWs are stable due to strong Coulomb interaction between S and Cr atom than pure ZnS NW. Moreover, the spin-down show semiconducting nature, while the spin up show the half-metallic ferromagnetic semiconductor seems to be good candidate as DMS spintronics application. The FM state stabilize through spin-up of Cr ion that is partially filled up due to energy gain from double-exchange mechanism, but the super-exchange mechanism has no energy gain. The spin-down of Cr ion show the semiconducting properties or no magnetism behavior. The exchange spin splitting of d-orbital of Cr ions in the FM state is larger than in the AFM state due to the double-exchange

mechanism. Moreover, the intrinsic vacancy can be overcome by co-doped of non-metal such as N, C, or I at anion site. The co-doped with N atom contributes the one hole into valance band that lower the Fermi level close to the valance band. From calculation, the total energy of co-doped at surface is lower than the bulk site indicate the N prefers at the surface of NW. In addition, the N-p states are asymmetrical in nature that involves in magnetization and favor the AFM coupled of d-state with p-state of N and S ion. Therefore, the co-doped involve in magnetization and spin density is concentrated around Cr and N atoms with less density around S atom.

Figure 8(a-c) show the absorption spectra of pure ZnS, surface configuration of Cr ion and co-doped samples that show high absorption near IR and UV-Vis region. The Cr ion surface incorporation show the d-d transition energy about 0.95 and 1.53 eV in near IR (Figure 8b). The absorption peak at 2.42 eV corresponds to the transition between the d-state and p-orbital in the valence band. The peak appears at 3.05 eV is due to transition between the interband transition and d-states of the Cr(II) ion. Therefore, the Cr (II) ion reduces the fundamental bandgap energy from 3.49 to 3.20 eV and slightly redshift appears through sp-d exchange interaction of the host and the localized d-electrons of the transition metal ion. Moreover, the co-doped sample show the sharp peak around 1.32-1.85 eV is assigned by defect states of co-doped samples generated by d-d transition of Cr spin ion (Figure 8c). Therefore, the single Cr ion and co-doping of ZnS NWs decrease the bandgap and e-h pair formation under illumination increase the absorption intensity. From the optical absorption coefficient, the d-d transition for FM and AFM configuration using electronics structures of near and far configuration as shown in Figure 8(a–c). To understand the magnetic coupling, we need to understand the optical absorption of FM and AFM of Cr coupled ion system. For FM configuration, the occupied d-states are below the Fermi level, while the unoccupied d-states are above the conduction band with d-d transitions peaks appears at 0.79 eV and 1.14 eV, respectively. For AFM configuration, the d-d transition energies are at 0.94 eV, 1.32 eV, and 1.53 eV of single Cr ion in the host lattice. Meanwhile, the AFM and FM configuration is blue and red shifted in luminescence spectra in various other II-VI semiconductors such as ZnS and ZnSe [256,257]. It is clear that the optical band gap and d-d transition peaks happen at the same energy level in both FM and AFM configurations due to the paramagnetic behaviors in the far configuration. The peaks related to bandgaps in both FM and AFM happen at 3.23 eV, while the peaks related to d-band-to-d-band transitions occur at 0.90 and 1.52 eV in both coupled spin systems [258].

TM ion in ZnS has been studied extensively to control its optical and electrical properties; therefore, it is special interest owing to nanoscale spintronic application. Various researcher successfully incorporated TM ion (Mn, Ni, Fe, Co, Cu and others) in ZnS using different synthesis mechanism [259–265]. Among all these, Mn doped in ZnS has been studied widely due to its phosphorescence and spin related application. Radovanovic et al. used CVD route to synthesized the Mn doped II-VI and III-V semiconductors [97]. Liu et al. calculation show the strong d-d transition in ZnS as host matrix is owing to cluster formation of Mn ion, thereby the regular distribution of Mn in the host matrix exhibits the room temperature ferromagnetic [250]. The s, p and d orbital density of states of S, Zn and Mn for Mn@DOS-ZnS in ferromagnetic ground states and spin exchange within d orbitals of Mn ion in ZnS. Calculation results show the ferromagnetic exchange and half metallic at fermi level for d-orbital make it much interesting for DMS application. Half-metallic exchange of d-orbital presence in electronic structure show ferromagnetic double exchange interaction and super exchange antiferromagnetic interaction at room temperature. Fernandez et al studies the low temperature absorption and luminescence of ZnS epilayer prepared on GaAs substrate, both experimental and theoretical calculation provide suitable information of temperature dependent heavy hole, light hole and split-off band along with the accurate information of temperature dependent eigen-states, broadening and strain related parameters, respectively [255]. Radiative recombination show strong injection rate due to inelastic exciton-polariton scattering. Emission peak at 470 nm related with the excitonic transition in UV range from valence band to conduction band. Emission related 340 nm is related to defect related emission and 590 nm assign to Mn transition. Mn is composed on excitonic transition band is happen due to charge transfer is at 355 nm (Mn^{+2} 3d → C.B); while series of d-d transition is $^6A_1$ (6s) → ^4E (4d), $^4T_2$ (4d), ($^4A_1$, ^4E) (^4G), $^4T_2$ (^4G) or $^4T_1$ (^4G) bands. Transition from $^4T_1$ → $^6A_1$ is lowest excited state for Mn transition within ZnS [257,263,266].

Figure 8(d-e) show the optical absorption behavior for Mn doped ZnS with different Mn concentration. In comparison with pure ZnS, Mn-doped and co-doped show several absorption edge due to excitonic effect in ZnS. Secondly, the Mn doped show slightly shift toward lower energy along with d-d transition at 2.19 eV. For single Mn ion in ZnS show the electron flip from spin up to down state with energy at 2.73 eV. From electronic transition, 3d-state of Mn occupied at the top of valance band and 4s-state of Zn at the bottom of conduction band. For co-doped (C, Mn) attributed transition between 3d (Mn) and 2p (C) near fermi level is half metallic. The d-d

transition for Mn–Mn pairs in FM and AFM coupling is obtained from the electronic structure. In FM configuration, 3d-states of Mn is fully occupied in the up-spin and 3d-states are empty in the spin-down. For one electron spin flip is also observed in ZnS with optical d-d transition energy of 2.01 eV for 5.25 % Mn concentration and 1.44 eV for 12.5 % Mn concentration in FM configuration. The spin of one electron flipped and the transition is from up-spin to down-spin state. The experimental result of ZnS:Mn NB [257], which is smaller than that of single Mn ion doped system (2.19 eV). For AFM coupling, the filled up-spin state of one Mn couple with the empty up-spin state of another Mn ion. Therefore, the d-d transition for 5.25% Mn concentration is 2.44 eV, and for 12.5% Mn is 2.32 eV in AFM configuration supported the experimental result. Thus, the d-d transition for FM coupled Mn doping is always smaller than that for AFM coupled Mn ions doping, which could show up simultaneously in Mn-doped ZnS NB and ZnSe NB for their luminescence spectra [257,267–269].
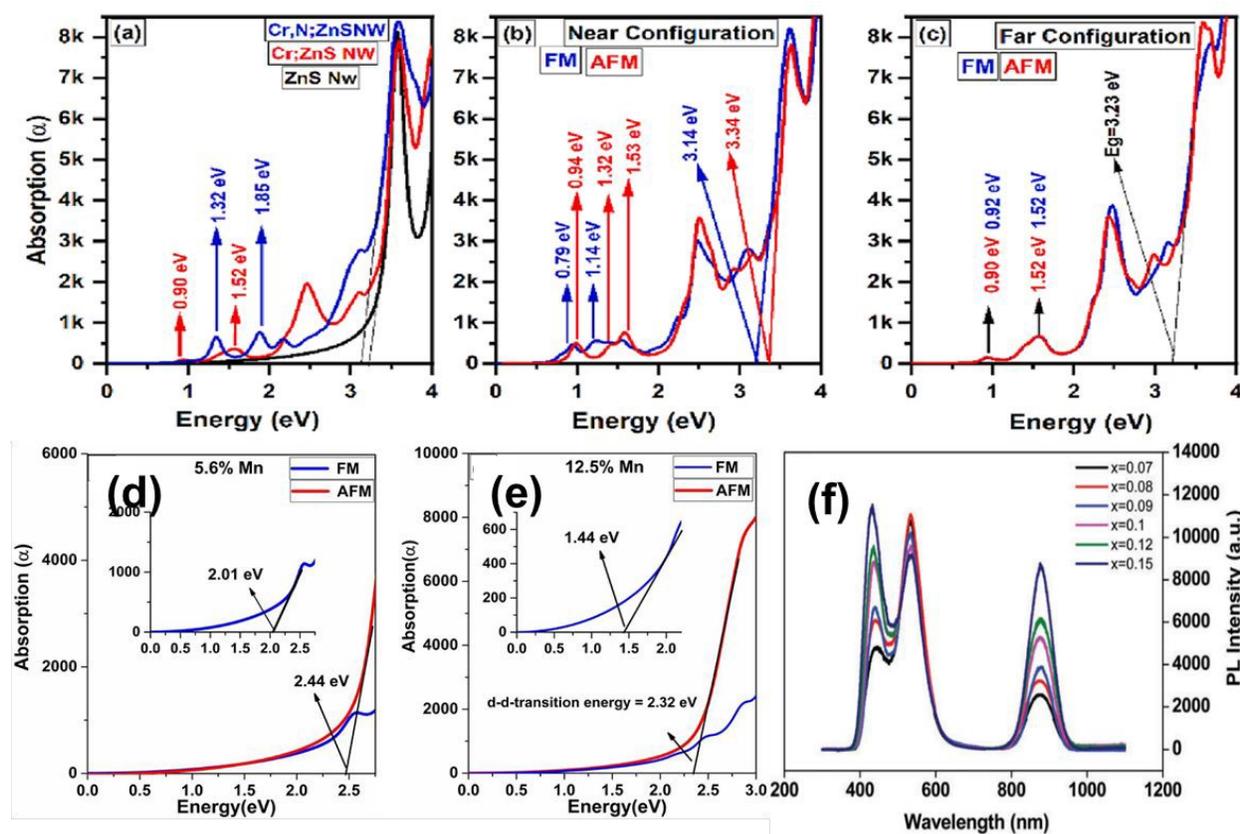

Figure 8: The optical absorption of (a) pure ZnS nanowire, single Cr(II) ion doped wire, and single Cr and single N co-doped wires, (b) FM and AFM systems in near configuration, and (c) FM and AFM in far configurations, Copyright © 2023 Elsevier [258]. The absorption spectra of FM and AFM

coupled Mn ions doped systems with 5.6% (a) and 12.5% (b) concentration of Mn dopants, Copyright © 2023 IOP Publishing [267]. (f) Room-temperature PL spectra of $Zn_{1-x}Mn_xS$ nanobelts, Copyright © 2017 the Royal Society of Chemistry [257].

VLS growth mechanism for 1D nanostructure growth of ZnS may lead the formation of twin or stacking fault during growth of NWs, NB and NR like structures [244,249,255]. Therefore, the defect related emission spectra of different morphology exhibits difference in their emission spectra due to surface relaxation or surface passivation for different nanostructures. Mn doping in ZnS matrix of different morphology also exhibits the difference in Mn related peak as discussed above for other II-VI materials in detailed. Kamran et al show the emission from localized Mn ion require no contribution surface capping [257]. Figure 8f show the Mn doped ZnS NBs with green emission due to dopant along with additional peaks at 420 to 460 nm and 560 to 890 nm. High temperature growth in CVD normally lead the formation of stacking fault in ZnS that show the emission peaks in the range of 520 to 550 nm which suggest the formation of AFM related with Mn-Mn pair formation. For ZnS:Mn NB, the dopant ion not contribute from the surface but defect can involve in AFM Mn-Mn pair formation with slightly blue shift as compared with emission of single Mn ion in ZnS lattice. However, QDs show the strong surface effect that directly influence the exciton stability and luminescence. For 3% Mn in ZnS NB, the emission band is decomposed into four emission peaks appears at 452.4, 535.5, 579.8, and 649.3 nm reflect their spin-exciton interactions and magnetic couplings. The blue emission assigned at 452.4 nm correspond to the anti-ferromagnetic coupling of 4 Mn ions. The green emission appears at 535.5 nm show the interaction of defects with the anti-ferromagnetic coupling of 2 Mn. While, the yellow emission line at 579.8 nm is due to the d–d transition ($^4T_1(^4G)$–$^6A_1(^6S)$) of Mn^{2+} ion also reported in ZnS:Mn QDs. The orange emission at 649.3 nm is corresponding to ferromagnetic Mn–Mn pair as reported in CdS:Mn. Moreover, the calculations of ZnS:Mn show the red- and blue-shifts of the d–d transition corresponded to FM and AFM coupling in MnS cluster, respectively. Further, increase in Mn concentration to up to 5%, show the emission at near IR at 877.6 nm. For high growth temperature in CVD, the Mn ion aggregate with high number will shift the yellow emission to red or near IR as observed for doping concentration above 6% due to FM coupling. The blue shift show the AFM aggregation of $(Mn)_n$ cluster of different energies in host lattice. Form Mn doped ZnS NB, the 0.2% Mn incorporation show the cluster or aggregation of two Mn ion. With increase in Mn ion show the multiple emission line or more Mn aggregate in host lattice, show the AFM coupling at

535 nm and cluster formation at 460 nm. From the experimental results, the increasing of Mn ion and the growth time both can increase the aggregation of Mn ions in the ZnS lattice with cluster stability that reflects the origin of the ferromagnetism in the ZnS:Mn crystal.

Moreover, the presence of defect due to TM ion doping may lead the formation metallic behavior at the surface of nanostructure and Mn cluster formation that may exhibits the AFM coupling [250,265]. Therefore, the peak emission is spectra at 452 nm, 579 nm and 877 nm assigned as the AFM coupling, d-d transition and Mn cluster formation in NIR, respectively as shown in Figure 8f. Under different composition gradient, the emission spectra intensity and peak position explain possible transition state with host matrix. Li and co-worker reported the Mn-related defect emission at 585 nm for ZnS NRs [266]. Kang et al. reported the room temperature ferromagnetism for Mn/Fe and Co doped ZnS via CVD [270]. Wang et al. fabricated the Mn doped ZnS sea urchin like structure from solvothermal method also assigned 587 nm peak emission related with Mn^{+2} ion in host matrix [271]. Therefore, the TM ion doping in ZnS matrix can control its electrical and optical properties to tune for spintronic applications.

3.2.3 ZnTe

In many respects, inherently p-type conductivity of ZnTe make its more attractive wide bandgap material among Zn-family and superior optical properties are due to its direct bandgap (2.26 eV) and Bohr exciton radius (6.2 nm) make it potential material for various optoelectronic applications [272–276]. PL emission spectra at 13 k show the split of single peak into multiple peaks that provide suitable information about host matrix related exciton emission. At 525 nm, the emission is related to band edge emission without Y-emission (600-700 nm) for high quality nanostructures obtained from VLS mechanism. Moreover, the Y-emission also show strong existence under impurity incorporation in ZnTe matrix due to presence of strain effect. The degeneracy of conduction and valance bands are 2-fold (Γ_{6c}) and 4-fold (Γ^{8v}) in zinc blende ZnTe, respectively. Large spin-orbital splitting at topmost of valance band assigned three exciton states; whereas strain may splitting the exciton in topmost of valence band into free exciton heavy hole and light hole. ZnTe Epilayer show the free exciton heavy hole and light hole at 2.379 and 2.375 eV at 2k, respectively [277–279]. Utama et al. reported the free exciton heavy hole and light hole at 2.377 and 2.372 eV, respectively. However, the bound exciton become dominant at low temperature and its emission spectra observed at 2.375 eV due to neutral acceptor causes by defects or extrinsic impurity. For room

temperature free exciton emission more prominent than bound exciton emission; bound exciton emission decrease at increase of temperature due to ionization effect. In this case, the emission at 2.368 eV (intrinsic shallow acceptor levels; Zn vacancy) is less than free exciton heavy hole at low temperature due to (i) no elemental doping and (ii) less stoichiometric related defect in VLS growth. ZnTe is polar semiconductor that exhibits the strong exciton-phonon interaction at low temperature due to resonance phenomena. The LO phonon are coupled with free exciton light hole that may leading the emission of higher-order LO phonons in ZnTe matrix also reported for CdS. So, the decay rate of excitons are highly enhanced due to presence of hot-exciton process [280]. Band edge emission of ZnTe is in visible spectrum (Green emission) without any impurity incorporation make it suitable for visible optoelectronics device such as LED and lasers [274,281,282]. Unique physical properties of ZnTe make it interesting for monolithic integrated optical circuits of signal transmission and processing, best electro-optical figure of merits of all semiconductors, terahertz generation and detection along with very favorable photodetection properties in various device applications such as p-type Field Effect Transistors (FETs) [281–283]. For wide bandgap semiconductor such as ZnTe also has strong exciton related emission incomparison with narrow bandgap semiconductor such as CdSe, CdTe in which band edge emission often rises from separate carriers after photo-excitation. Therefore, carrier effect is ZnTe is also reported by researcher that might show the redshift in the emission spectra as the function of incident intensity related with surface Plasmon effect [284–286]. Such phenomena may depend on the growth condition, synthesized mechanism and quality of final product obtained.

Transition metal ion related Luminescence behavior

TM ions in II-VI semiconductors (based on tellurides) are best-known diluted magnetic semiconductor (DMS); TM ion is substituted by cations of the host semiconductor are appealing bridge for future spintronic devices. Most of the research groups used Molecular beam epitaxy (MBE) technique to substitute TM ions (such as Mn, Cr, and others) into ZnTe for spintronic application [6,79,105,287]. Other methods also employed for TM ion doping in ZnTe reported by various groups [2,284,285,288–290]. PL is effective and non-destructive technique to find the bandgap and related other information such as impurities in host matrix to find the origin of transition in the spectra. Figure 9c show the lasing in single belt like structure of Fe doped ZnTe prepared by VLS mechanism at room temperature. Room temperature PL spectra show the NIR emission for Fe doped ZnTe. Angle resolved measurement reveals the cavity formation in microstructure due to

presence of Zn vacancy that exhibits the strong luminescence in NIR emission at room temperature. Moreover, fs laser excitation exhibits the near band edge lasing but no emission can be seen at NIR as observed by continue laser excitation. This indicates that the exciton-defect related emission due to slow/fast coherent recombination process exhibits in single structure [290]. Moreover, the electronic configuration of Ni doped in ZnTe matrix; where Ni^{+2} is tetrahedrally coordinate by four anions (T_d symmetry point). T_{2g} – orbital of $3d^8$ of Ni^{+2} interact with p-orbital valance band to form strong sp-d hybridization that break the optical selection rule and make d-d transition in emission spectra. Moreover, the PL emission spectra reveals the redshift due to (i) radiative recombination of exciton or photo-induced carriers (ii) bandgap renormalization effect (iii) carrier-carrier scattering and (iv) e-h plasma formation at the surface under high laser power [285,291]. Another factor that cause the redshift formation is the structure dependent surface effect that can enhance the carrier-carrier scattering leading to the formation of e-h plasma formation at the surface. Laser spot size on the rod and belt like structure exhibits more surface e-h plasma effect in belt like structure due to surface act as reflector due to Zn deficiency or Te inclusion at the surface. Polarized PL emission of both Mn and Ni doped samples provide the suitable information of structure that suggest zinc blende structure is obtained at high temperature growth in VLS mechanism [285]. Normally high temperature growth of ZnTe lead a cavity formation that exhibits the NIR emission and literature suggested that the cavity formation normally observed in wurtzite structure. For zinc blende cubic structure, possibility to observe the cavity related NIR emission is twinning or polymorphs in structure during high temperature growth as reported in ZnTe [52,291–293].
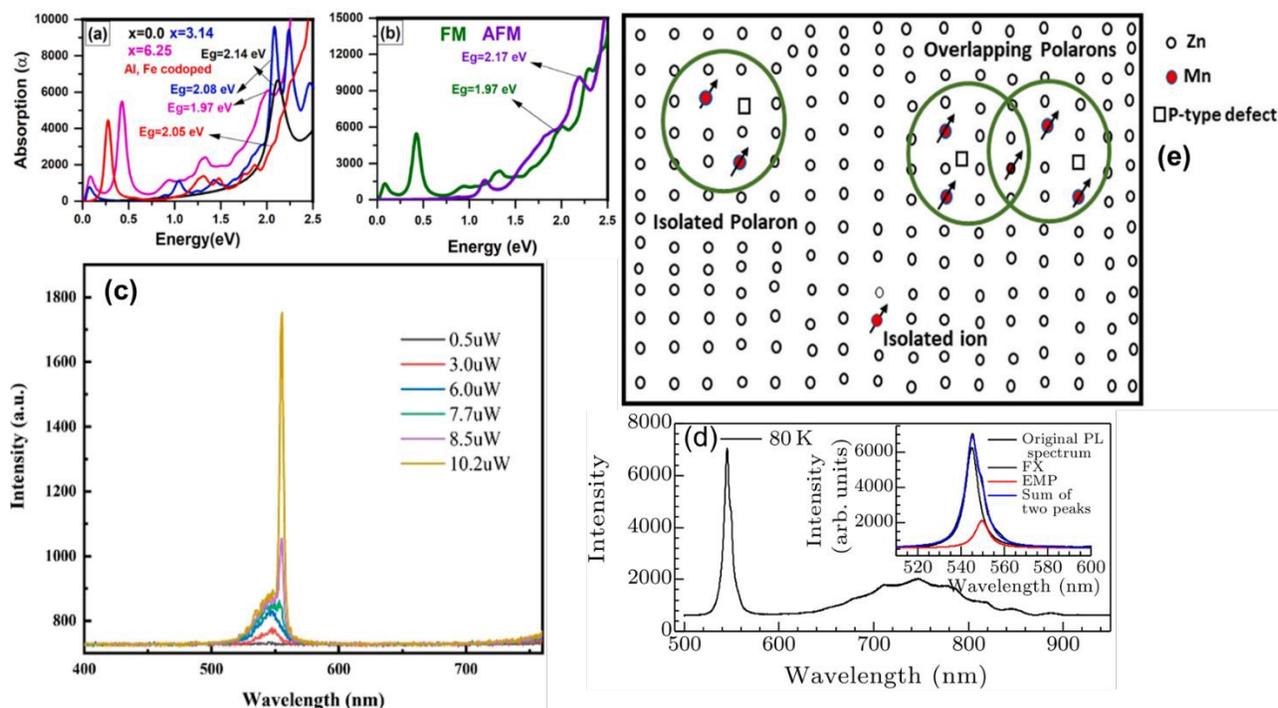
Figure 9: (a) Single Fe doped, double Fe doped and (Al, Fe) co-doped ZnTe (b) Absorption spectra of FM and AFM coupled ion system. Copyright © 2023 Elsevier [2]. (c) PL emission spectra of the ZnTe microbelt under femtosecond pulse excitation with pump powers changing, Copyright © 2023 American Chemical Society [290]. (d) PL spectra of Co doped ZnTe at 80 k with Lorentz fitting. Copyright © 2018 Chinese Physical Scoiety [289]. (e) Schematic diagram of bound magnetic polarons model for Mn (II) ZnTe, Copyright © 2023 Elsevier [1].

Figure 9a, b show the first-principles calculations study of the magnetic and opto-electronic properties of Fe (II)-doped ZnTe based on the RKKY-exchange. Fe (II) occupied the tetrahedral crystal field to show the spin allowed d-d transition in IR region. Optical bandgap reveals the AFM coupling blue shift, while the FM coupling exhibits the redshift in the emission spectra. Fe ion in host lattice has no gain in energy due to double exchange of spin states (e_{2g} and t_{2g}) that are fully occupied support the FM interaction. Similarly, the two spin ion of same spin gain energy due to super-exchange of half-filled e_{2g} support the AFM interaction. The exchange splitting of d-state in FM state is smaller than in AFM and energy gained due to super-exchange interaction is larger than that due to double exchange interaction. For n-type incorporation of dopant ion in host lattice occupied the spin down partially filled at e_{2g} state, which support the FM configuration. Therefore, the large exchange splitting of d-state support the FM interaction with double exchange is larger

than super-exchange that favors the FM state in n-type Fe (II) doped ZnTe. Fe ion incorporation in ZnTe and co-doped with Al ion is responsible for intermediate d-states between conduction and valance band. Fe ion associated with intra-band transition absorption peaks appears at 0.2, 0.92 and 1.03 eV are associated with electronics transition of E_2 to T_2^3 and E_2 to T_2^3 states, respectively. As, the Fe ions increases, the number of d-states also increase with additional d-d transition peaks appears due to Fe-Fe pair system corresponding to transition states of $E_1^2 - E_2^2$, $E_1^2 - E_3^2$, $E_1^2 - T_1^3$ and $E_1^2 - T_2^3$ having energies at 0.25, 0.45, 0.88, and 1.31 eV, respectively. The d-d transition intensity increases with increase of Fe concentration but with Al co-doped show reduces of d-d transition along with band-edge transition peaks. Moreover, the increase in Fe (II) concentration show redshift in band-edge transition and d-d transition related with Fe-Fe ion through sp-d exchange coupling. When Al is co-doped in ZnTe, the Fe(II)-Fe(II) ion pair show blue shift in bandgap due to Burstein-Moss effect. Additionally, in the Fe(II)-Fe(II) ion pair system, the intensity of the absorption coefficients rises with Fe concentration and falls after co-doping. From density of states peaks of FM and AFM configuration show the occupied and unoccupied d-orbital states for both Fe (II) and Fe (II) with co-doped in ZnTe. The d-d intra-band transition exhibits the red and blue shift for FM and AFM coupled system with different energy show the different type of magnetic coupling influence in the absorption spectra confirm by both theoretical and experimental data. The improved opto-electronic and magnetic properties of Fe (II)-doped ZnTe by n-type (Al) co-doping provide insight into the potential applications of these materials in spin-related photonic and spintronic devices such as photovoltaics and remote sensing [2].

Dong et al. show the terahertz generation by optical rectification in ZnTe usually degraded by factors (i) harmonic generation, (ii) two-phonon absorption and (iii) free carrier absorption [294]. The Te inclusion in ZnTe for THz generation observed with IR transmission spectroscopy. Te inclusion has hundreds of picoseconds region and wider width; while for ZnTe matrix several picoseconds. On the other hand, central frequency and bandwidth of Te inclusion are 0.1 and 0.6 THz, whereas, the ZnTe are approximately 0.2 and 1.8 THz. Additionally, the amplitude of the THz waves from Te inclusion at the center is higher than that from the ZnTe matrix. Te inclusion in ZnTe matrix attribute the unique emission that may enhanced the multiple reflection of THz pulse. Such multiple reflection enhanced the phonon polariton within the host matrix related with the second harmonic generation [294,295]. The energy transfer mechanism based on the anti-stokes emission for various technological applications in biological imaging, up-converted laser, solar cell and many

others [296]. Excited states absorption (ESA) show the electron transition that uses as absorb two photon at intermediate electronic states to create highly excited carrier. Energy transfer induced up-conversion (ETU) is similar to Auger effect in which energy transfer from excited e-h pair to another carrier. Two-photon absorption (TPA) is the simultaneous absorption of two photon within intermediate state to achieve high electron transition. For TPA related emission show large anti-stokes shift without acquire real intermediate state at high excitation density at nanoscale time scale. So, high density and shorter time scale is key for TPA related linear upconversion absorption. Phonon-assisted anti-stokes PL (PA-ASPL) exhibits only where strong electron-phonon interaction happen at very low excitation power. Phonon related anti-stokes emission involves indirect optical transition due to hot exciton effect in polar semiconductor as discuss above for both ZnTe and CdS naonbelt. Exciton are strongly coupled with optical phonon through deformation potential interaction or Frohlich interaction that is responsible for higher order Raman peaks due to resonance phenomena.

Figure 9e illustrates the schematic of the BMP model responsible for the ferromagnetism in p-type Mn (II) doped ZnTe. Different mechanisms, such as double exchange mechanisms, bound magnetic polarons, super-exchange mechanisms, and band-coupling models, were used to explain the ferromagnetism in the DMSs. The most widely considered defect-mediated mechanism for understanding ferromagnetism in dilute magnetic semiconductors is the bound magnetic polaron model. Zn vacancies play a crucial role in understanding the magnetism in the Mn(II) in ZnTe, the 3d states of Mn ions around defects couple ferromagnetically to each other at which the hole carriers are bound to form the BMPs. Polaron-polaron interaction ferromagnetic coupled with carrier-ion-carrier interaction. Paramagnetic (PM) component is attributable to isolated polarons and Mn (II) ions. In addition, the co-doped and Zn vacancy boost the room temperature ferromagnetism. Furthermore, we infer that the BMP model (defect-mediated model) fits to understand the origin of ferromagnetism. The optical study reveals the that Mn (II) doping at the Zn site widens ZnTe bandgap and produces spin-forbidden d-d transition peaks on the low energy side of the bandgap. The p- type defects in Mn (II)-doped films produce absorption peaks in the infrared region and improve the absorption efficiency. In addition, the optical bandgap and spin-forbidden d-d transition of Mn(II) to different modes of spin- spin interactions were correlated, and we found a red shift of d-d intra-band transition peaks as well as an optical bandgap in the FM-coupled Mn(II) ions system and a blue shift in the AFM coupled ions system, supporting the

experimental observations. Theoretical calculation of Mn(II) doped ZnTe show the occupied spin level of Mn lead to super-exchange mechanism in p-type semiconductor. Mn incorporation lead the ferromagnetism behavior through additional hole carrier formation with dopant ion. Moreover, the Zn vacancies and co-doped coupled the hole carriers with spin-up of Mn(II) ion with stable ferromagnetism behavior. The hybridization of Te-p level and Mn(II)-d level around fermi level support the stabilized AFM of d-level due to fully occupied of spin electron after gain energy to support super-exchange mechanism. The double-exchange mechanism appears with no energy gain occupied just below the conduction band or minima of conduction states. Meanwhile, the spin-up and spin-down overlapping show no magnetism for AFM coupled ion system. Since, the interaction between two-spin ions with opposite shift at d-orbit show the exchange spin splitting of large AFM state than FM states. Therefore, the origin of AFM coupling in ZnTe slab-like structure is due to super-exchange of electron hopping occurs between Mn ions via the intermediate p-state of the anion. From experimental results reveals that the hole carriers play vital role in ferromagnetism behavior in DMS study along with defect states and co-doped to enhance p-type behavior in semiconductor. In general, the FM state is highly stabilized with additional hole carriers that localized at the topmost of valance band in ZnTe with broaden due to symmetry breaking relaxation. Secondly, the Zn vacancy act as double acceptor that generates two holes in the spin-up states by charge transfer in the coupled ion systems. The states splits into occupied and empty states in the majority spin channel due to the transfer of charge from the Mn-d state to the defect level of Zn vacancy. The energy difference is about 135 meV greater than thermal energy indicate the stable FM state than AFM above room temperature. The magnetic moment contribute by (i) Mn (II) ion doped in ZnTe or Mn-Mn interaction (ii) hybridization between Mn-d and Te-p orbitals with minor magnetic moment and (iii) spin distribution of Mn(II) with Zn vacancy. The large density of spin exists around Mn(II) and the interaction of the Mn ion with the nearest Te atoms is antiferromagnetic. Moreover, the co-doped also enhance the ferromagnetism behavior as it act as double acceptor with energy difference about 138 meV lower than AFM state [1].

Figure 9d show the Co doped ZnTe show the free exciton emission along with the shoulder peak of energy difference of 19.4 meV less than LO phonon at 80 k assigned to EMP emission. The aggregation of Co ion show the ferromagnetic spin that bind with free exciton to form EMP. Moreover, the broad emission ranging from 600 – 900 nm show the d-d transition associate with $^4T_1(P) \rightarrow {}^4A_2(F)$ of ferromagnetic coupled Co ion in the host lattice from high d-level of intra-band

transition. Moreover, the power dependent emission reveals the redshift in shallow-trapped states (564 nm) due to high carrier concentration generation normally appears in low excitonic binding energy semiconductor such as ZnTe (12.6 meV). The high excitation power generate the large number of photoinduced carriers that are responsible for an electron-hole plasma formation at the surface. Secondly, large radius for photon and exciton increase the possibility of electron-phonon coupling with increasing in electronic scattering, that is responsible for large red shift at 563 nm. Previous studies deduce the formation and emission of EMP in TM ion doped II–VI semiconductors, specifying the emission at the long-wave side of FX. There is a double-peak structure in the range of 540–580 nm, and the emission of EMP appears due to the coupling between free excitons and ferromagnetic spins out of transition metal ions. The emission peak at 572 nm related with EMP, which is corresponding, to phonon and spin interaction. Redshift in EMP emission indicate the carrier interaction dominant and increase in intensity show the strong spin binding effect at high power due to large polaron radius. Therefore, the EMP becomes more dominant even at high concentration provide stability of spin-spin interaction even at room temperature and high excitation power [297].

Ni (II) ion doping in ZnTe show magnetic polarons together with hot carrier effect that need to be understand by Power and temperature dependent PL. The spin-exciton, spin-spin coupling and carrier-phonon interaction emission account for their ferromagnetic properties. The power dependent luminescence behavior responsible for hot carrier effect that suppressed the charge trapping effect for low exciton binding energy (8.12 meV). The large polaron radius exhibits strong interaction between carrier and magnetic polaron results anharmonicty effect in which side-band energy overtone to LO phonon. The photon-like polariton show the polarized spin interaction with LO that show strong spin-phonon polariton. Multiple emissions show the non-uniform distribution of Ni ion in ZnTe nanostructure with strong exciton emission near band edge and lower energy side due to ferromagnetic coupled Ni pair or cluster interact with traps/defect state. The localized spin induced exciton interact with hole exchange (heavy hole greater than electron) at the topmost of valance band in ZnTe to form LEMP formation. Non-radiative decay of localized spin/exciton is responsible for multiple emissions at room temperature related with photon-like polariton. The optically polarized anisotropy explain the dielectric contrast due to degeneracy of exciton states at the topmost of valance band represent spin-spin coupling, exciton-spin-phonon and electron-phonon interaction of magnetic polarons of low excitonic binding energy semiconductors for

future spin-based optoelectronic devices. The free exciton (FX), FX interact with 2LO phonon-spin interaction corresponding to $^3T_1(^3F) \rightarrow {}^1T_1(^1G)$ and EMP peaks with ferromagnetically coupled Ni ions at $^3T_1(^3F) \rightarrow {}^1E(^1G)$. In addition, other d-d transition of single Ni ions (600-900 nm) appears at low energy side with energy shift of 14-38 meV due to localized states. These results show spin-spin magnetic coupling and spin-phonon interaction at room temperature that open a new horizon of optically controlled dilute magnetic semiconductor applications more realistic [298].

3.2.4   ZnO

Zinc oxide semiconductor with hexagonal wurtzite structure, direct bandgap (3.37 eV) and large exciton binding energy of 60 meV has been widely use as transducers, transparent conduction electrode, solar cells, and wide ultraviolet (UV) optoelectronic devices. 1D ZnO nanostructures exhibits the high charge transport, mobility, electron affinity, and thermal stability make it attractive for solar cell and other electronic devices has been synthesized by both physical and chemical method [299–303]. ZnO NWs and layer used as transport layer in hybrid solar cell based on Poly (3-hexylthiophene) (P3HT)/ZnO composite are benchmark systems that have attained high power conversion efficiencies [25,304]. ZnO also exhibits the strong electron-phonon interaction that may lead the formation of multiple phonon emission or hot exciton related emission that can be observed in absorption spectra, PL and scattering spectra. Zou et al. discuss the exciton coupled with magnetic ion in micrometer-sized DMS in ZnO and CdS. Ferromagnetic and optical responses strongly depend on TM's growth size, composition in local structures, and the nature of TM ions. For TM-doped II-VI semiconductors QD show confined exciton to form EMP in QDs. Moreover, the size dependent quantum confinement reveals giant Zeeman splitting, photo-induced magnetism and anomalous temperature variation dependent EMP emission. The increase in TM composition gradient in QDs shows the energy shift and enhances the spin-orbital coupling and spin-spin coupling that enhance the EMP formation without LO phonon. For 1D or other than the quantum confinement effect, the exciton interaction with spin changed due to the long-range coherence of EMPs. The luminescence behavior shows that the condensation of EMP formation in higher dimensions corresponding to collective spin influences their electrical and optical response. II-VI semiconductors NWs and NBs as prepared with CVD mechanism for DMS highlighted their long-range exciton-spin interactions and optical behaviors even at small

concentration. The spontaneous migrate the TM ions formed cluster formation in high temperature growth with no new phase in host matrix [5]. Dietl et. al predicted that the transition temperature Tc in p-type ZnO DMS will be greater than 300 K, which is possibly used for making various room-temperature spintronic devices [6,7,105,305].

Transition metal ion related Luminescence behavior

Figure 10a show the power dependent PL spectra of ZnO:Mn NW excited by 355 nm fs laser as prepared by CVD. At low pump power, the free exciton peak appears at 3.305 eV with another peak at 3.168 eV ahead of free exciton peak. The energy difference between two peak is about 137 meV correspond to overtone of A1 2LO mode originated from polaronic exciton of bound exciton that involves the spin-phonon coupling. Further increase in excitation power show superlinear increase in peak B as shown in Figure 10a. The peak A related with free exciton slightly increase and decrease swiftly as power increases from 0.3-3 µJ. Figure 10b, c show the intensity and FWHM as function of excitation power. For high power range, the peak B become sharp with reduction in FWHM. The lasing line of peak B is blue shifted about 50 cm^{-1} and analogous to the phase space filling effects of excitons at high excitation which represent an exciton repulsion but not a carrier effect. Above 4.0 µJ, the lasing line narrow around 3meV that reflects the complete coherent emission along with increase in intensity as show in Figure 10b. Further increase in power may lead the formation of additional line in the spectra corresponding to dipole-dipole interaction of exciton out of single mode coherent. Figure 10c show the single mode lasing of ZnO:Mn NW with narrow FWHM related with BEC excitons. For low doping profile in ZnO NW show the emission at low excitation power due to exciton coupling and electron-phonon coupling at room temperature for large exciton binding energy (60 meV) semiconductor. For high Mn ions in host lattice may weak the UV emission at low power due to trapped states within bandgap. The emission show the non-linear phonon-phonon coupling in 1D NS with the enhancement of A1 phonon along the axial direction. Such strong non-linear coupling may lead the formation of 2LO phonon interaction with exciton that exhibits the boson nature of bipolaron exciton in 1D system about 4 µJ/cm^2. The intensity increment and narrow FWHM reflect the coherent two-phonon-exciton formation and condensation that lead the BEC states at room temperature for ZnO:Mn. The stable BEC in 1D system is related with (i) coherent and high-density exciton states produce by fs laser, (ii) side crystal face reflection may enhanced the high-density exciton, and (iii) aggregation of free exciton with different orientation assisted by coherent 2LO A1 phonon in longitudinal direction.

Therefore, the high-density bipolaronic exciton emits coherently that reflect the characteristic of dynamics BEC stats. Figure 10 d show the 3D contour plot for coherent exciton emission for different laser power. Emission spectra of Mn doped ZnO clearly reveals stokes signal interact with LO phonon because electron interact more strongly with LO phonon rather than other phonons due to deformation potential interaction [306]. For ZnTe, the LO phonon involves the relative displacement due to opposite charge ions that induce polarization which strongly interact with electron through Frohlich interaction [296]. Mn doped ZnO NWs exhibits the strong electron-phonon interaction as observe the eleven order of LO phonon modes in which deformation potential of dopant ion influence the atom displacement from equilibrium position. Therefore, the displacement of atom enhance the lattice polarity and show the multiple phonon due to strong electron-phonon interaction in Mn doped ZnO NWs. Secondly, the slight shift towards higher wavelength sue to sp-d hybridization between localized d-electron of dopant atom and VI-group anion as observed for other II-VI semiconductors. Thus, magnetic ion doping quench the band edge emission is owing to radiative absorption by color center, which highlights the high-order phonon peaks in hot luminescence process under 325 nm and 355 nm [306].
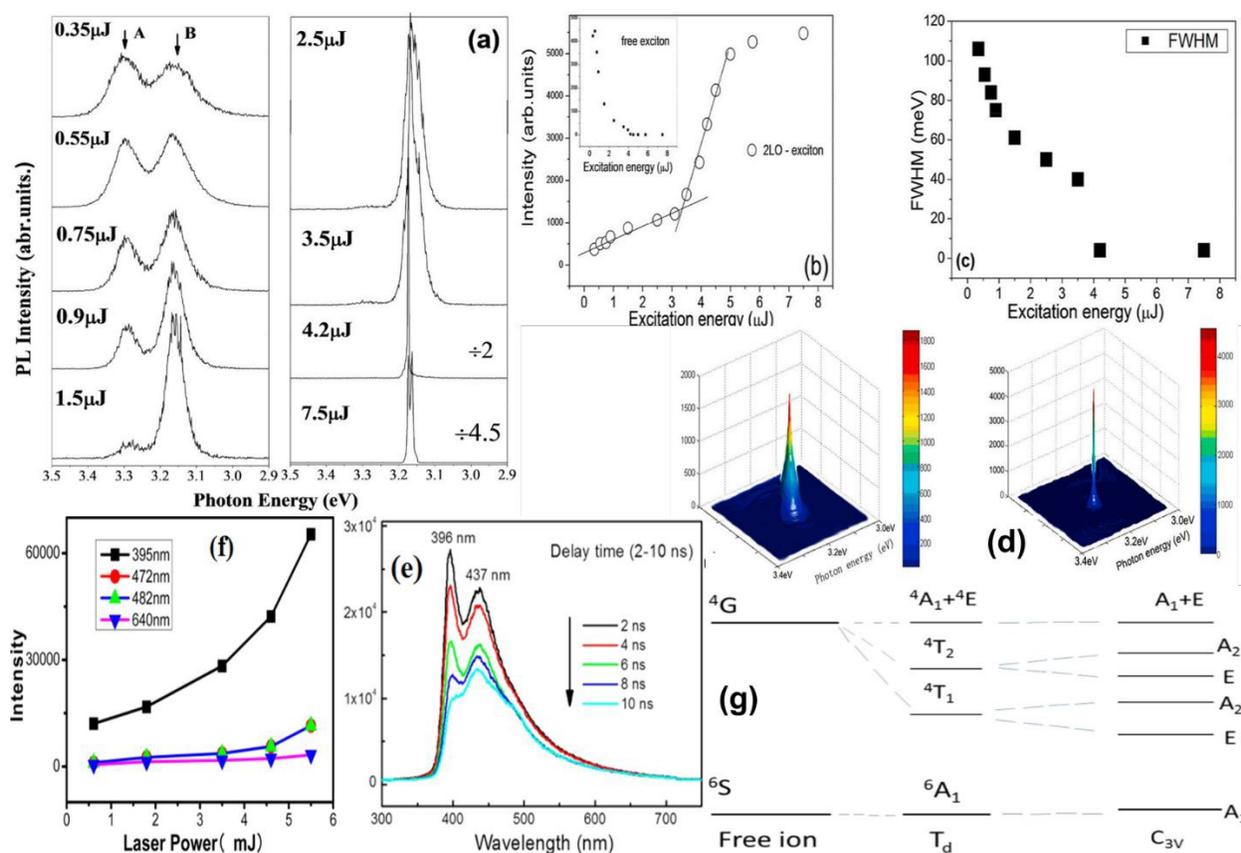
Figure 10: (a) Photoluminescence spectra at various pumping energies of ZnO nanowires. (b) The luminescence intensity vs laser excitation energy. (c) The luminescence B band FWHM vs laser excitation energy. (d) The energy profile of the luminescence B line at 3.5 μJ and 4 μJ. Hot luminescence spectra of Mn-doped ZnO NWs, Copyright © 2011 IOP Publishing [307]. (e) Time-delayed photoluminescence of ZnO:Mn NW under a laser pulse at 355 nm (duration 2 ns) from third harmonic of a Nd:YAG laser with the pumping energy 3.5 mJ. Observed spectra variation after the NW was excited within 2−10 ns delay time range. (f) Dependence of the emission intensity of various wavelength on the excitation powers (g) Diagram of Mn(II) levels in ZnO matrix. $^6A_1$ is the ground state and $^4T_1$, $^4T_2$, ^4E, and $^4A_1$ are excited states in ZnO, respectively. Copyright © 2014 American Chemical Society [4].

TM ion doping in ZnO are important for DMS and their structure and magnetic origin need to be understand. Liu and co-worker explorer the magnetic exciton relaxation and spin-spin interaction of Mn doped ZnO NW prepared by CVD method [4,308]. Figure 10e show the Time-delayed PL of ZnO:Mn single NW under a laser pulse at 355 nm (duration 2 ns) from third harmonic of a Nd:YAG laser with the pumping energy 3.5 mJ. Observed spectra variation after the NW was excited within 2−10 ns delay time range. Emission at 396 nm and 437 nm observe at low excitation power, as the delay time is extended, the shoulder peak at 480 nm appears along with shift peak from 396 nm to 402 nm. At high delay time about 28 ns, emission peak 472 split into multiple peaks and become sharp under more delay with the emission of another peak at 636 nm that is Mn related emission. Figure 10f show the dependence of the emission intensity of various wavelength on the excitation powers. From these result, we conclude that each excitation emission in luminescence spectra is time dependent related to their electronic configuration, carrier-carrier interaction, carrier coupling with spin ion interaction, carrier-phonon interaction and exciton-phonon interaction in the respective host material crystal symmetry [309,310]. All the emission peak observed under different time domain show the superlinear intensity increase with laser excitation power as shown in Figure 10f. For 1D nanostructure such phenomena become more interesting specially related to exciton and exciton-spin relaxation characteristic. At first, the exciton related emission exhibits that further recombine with phonon or impurity or magnetic ion related emission in the spectra as observe with fs laser produce free exciton and bipolaron exciton in Mn doped ZnO NW [307]. Moreover, the excitation in ZnO is orientation dependent as discuss above about vertical align and horizontal align NW reveals different quantum efficiencies. So, the intermediate

states with lower energy are populated after the relaxation of photoinduced carriers [5,310]. Emission at 394 nm for 2 ns pulse is assigned as bi-polaron exciton (BPE) or it could be EMP [4,307]. Schematic diagram (Figure 10g) to account for d−d transitions from the ground state $^6A_1$ to the different intermediate excited states $^4T_1$, $^4T_2$, ^4E, and $^4A_1$ in ZnO are calculated to be 2.55, 2.85, 2.97, and 2.99 eV, respectively through CI energy band calculation and photoemission spectra [4,311]. Therefore, both theoretical and experimental correlation provide suitable information about emission spectra of ZnO crystal symmetry matrix with and without doping at room temperature. Also, 1D Mn doped ZnO NWs show coherent emission localized exciton magnetic polaron, that is source of ferromagnetism in host matrix to produce coherent EMP emission related different time domain. Such kind of 1D single structure are significant for both spintronic and spin related photonic devices. The epitaxial growth of ZnO NW array on sapphire by chemical vapor transport method and find out the external quantum efficiency related to PL of ZnO NW at room temperature [301,312]. Interestingly, bandgap related external quantum efficiency (EQE) is strongly depend on the excitation power density and spot size. For EQE, we have to understand the absorption first; as the band edge emission improve or intense with increase incident laser power than the exciton related radiative recombination dominant. On the other hand, defect related emission become more intense than near band edge indicate the non-radiative recombination related with defect state is dominant in the single structure.

3.2.5 Ternary Alloy of Zinc chalcogenides (ZnX; X=S, Se, Te, O)

The ternary alloy of Zn chalcogenides with tunable composition for bandgap engineering prepared by VLS mechanism and solution process method. The compositional variation in II-VI semiconductors cause the optical inhomogeneity that may lead the formation of more scattering and screening to charges but still exciton play vital role for lasing as excited by two photon pump lasing for $ZnS_{1-x}Se_x$ nanoribbons [313]. Quantum confinement has predominant effect on optical gain media including tunable emission in board spectrum, low threshold lasing and temperature insensitive lasing performance at nanoscale. For low dimensional system stimulated emission and lasing is quite challenging especially but high quality synthesis of colloidal QDs overcome this problem. For one-photon, pumping in colloidal QDs has poor spatial resolution especially for biomedical field. Therefore, the two-photon or multiple photon absorption method has been employed to investigate the biophotonics without strong scattering from tissue or biological

sampling. ZnS/CdS/CdSe colloidal QDs excited with one-, two- and three- PA (photon absorption) with fs laser pulses at 480 nm, 800nm and 1300 nm, respectively. The stimulated emission of CdSe/CdS/ZnS core-shell QD excited with 1300 nm [271]. Figure 11a show the photoelectron transfer diagram of $Zn_xCd_{1-x}Se$ and $Zn_{0.9}Cd_{0.1}Se$/ GQDs nanocomposites as prepared by hydrothermal process. Zn/Cd ratio can alter the crystal structure from wurzite (CdSe) to cubic (ZnSe) with high current photocurrent for 0.9/0.1 ratio [314]. The composition gradient changes within the single structure, the emission line is also tuned depend upon the Se or S composition modulation. As the fs laser excitation increase, the lasing phenomena also study above threshold value of 1.2 to 5.13 mJ cm^{-2} for ZnSe to $ZnS_{0.43}Se_{0.57}$ under different excitation power. For core-shell structure, ZnTe used as type II with CdSe or ZnSe to covers the visible spectrum range. ZnSeTe QDs emits blue color to green emissivity by controlling the Se/Te ratio. However, the realization of red-emissive becomes highly exciting mainly due to a strong band gap bowing between bulk ZnSe and ZnTe. An identical triple shelling with ZnSe inner and ZnS outer show PL emission at 608 nm with quantum yield of 55%. An enhance their PL performances, an interlayer of ZnSeTe with lower Te/Se ratio as interlayer not only improve the PL emission but also improves the quantum yield up to 63 % with slightly redshift. Te ratio as interlayer is potential application for red emission in display devices [315]. ZnTe/CdSe/(Zn, Mg)Te core/double-shell NWs grown by MBE show the emission to the spatially indirect exciton recombination at the ZnTe/CdSe Type-II interface. The significant of study to observe a blue shift of emission energy with an increasing in excitation fluence that induced electron-hole separation at the interface. The optical emission in the NIR originates from NWs, and not from 2D residual deposits between them. Both CdSe shell thickness and Mg concentration induced the NIR emission related with strain or defect related layer within heterostructure NWs as measure by cathodoluminescence [203,316].

Tang et al. reported the gradient alloy of $ZnS/Cd_xZn_{1-x}Se_yS_{1-y}$ core-shell QDs for liquid crystal display based on reversible thermal quenching based o multiphonon process, temporal trap states and re-existing trap states. CdSe provide effective confinement to electron and hole recombination for large band gap material such as ZnS. Secondly, the core-shell confine the wave function of electron and hole for exciton recombination that may reduce the interfacial trap defect. Under illumination, the Auger recombination will determine the non-radiative recombination at high power. Therefore, the luminescence quenching in QDs related with static charge distribution of trap states and surface trap states. Both resonance tunneling and thermally active physical process

followed by radiative with and without tunneling and non-radiative recombination activate through tunneling [146,171,243,317]. ZnCdS and ZnSSe QDs alloy show the blue emission with quantum efficiency of 25-50 %. For core-shell nanostructures, the ZnS can be used as both Type-1 and Type-II semiconductor with core of different II-VI semiconductors [21]. ZnSSe NRs show spontaneous emission as excited by two-photon pumping with 800 nm fs pulse laser. Increase of Se ratio in single crystal NR show red shift from 422 nm to 464 nm. Lasing emission line achieved at 5.13 mJ/cm^2 with sharp emission intensity (Figure 12b). Further increase in excitation power illustrate super-linear emission intensity in single crystal that further narrows the FWHM due to occurrence of stimulated emission. A slightly blue shift in the position corresponds to the phase space-filling effect of exciton at high excitation for low threshold material such as ZnSSe NR. Two-photon pump with fs laser help tool to understand the lasing generated by free exciton and its scattering process in ZnSSe single crystal. Lifetime provide the suitable information of lasing behavior originated from free exciton or bound exciton in the ternary alloy of ZnSe. Amplitude of decay time of free exciton is increased and bound exciton amplitude decrease above threshold value due to cavity effects that saturates the binding states under high carrier density and reduces the bound exciton amplitude. Decay time also decreases with increases in pump energy that suggest the transition from spontaneous emission to stimulated emission with narrow bandwidth and super-linear emissive intensity. The different modes illustrate gain competition and distinct shifts as a utility of excitation density [313,318].
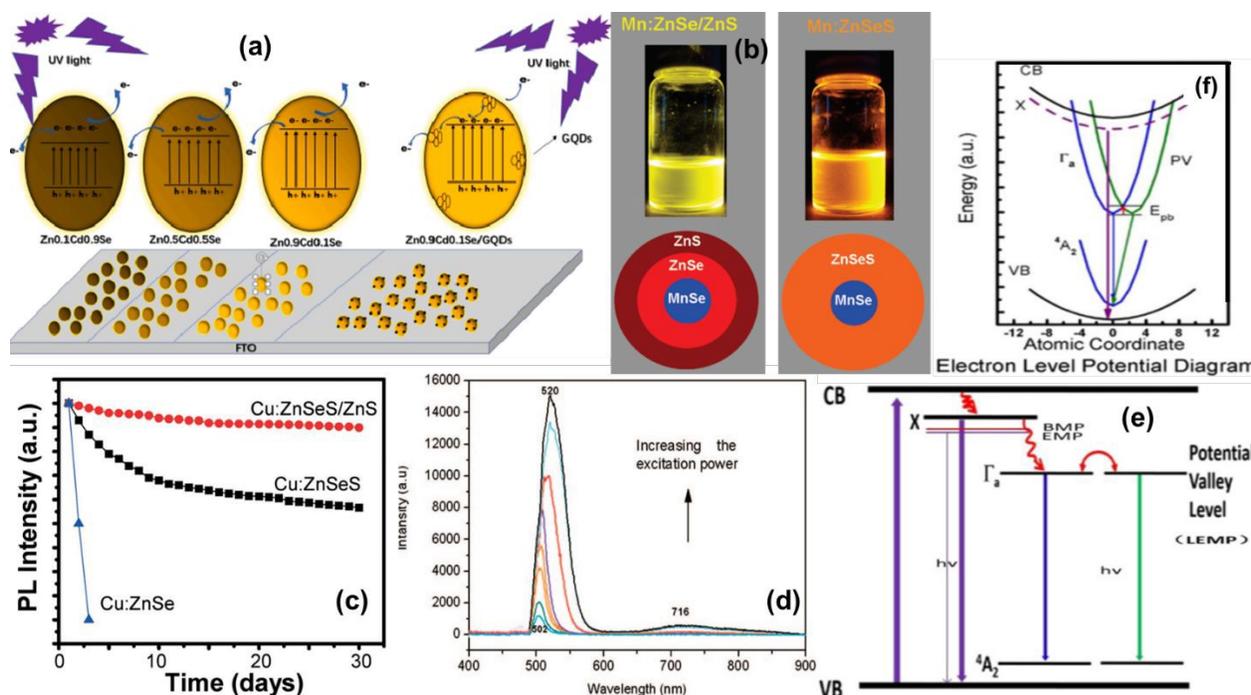
Figure 11: (a) Photoelectron transfer diagram of $Zn_xCd_{1-x}Se$ and $Zn_{0.9}Cd_{0.1}Se/$ GQDs nanocomposites, Copyright © 2022 Elsevier [314]. (b) digital image of ZnSe/ZnS:Mn (left) and ZnSeS:Mn (right) expose by UV lamp, Copyright © 2011 ACS publishing [319]. (c) The photostability curve plot of Cu:ZnSe, Cu:ZnSeS and Cu:ZnSeS/ZnS d-dots in air and light, Copyright © 2011 The Royal Society of Chemistry [320]. (d) PL of 6-fold symmetry branched nanostructures using Ar^+ 488 nm as excitation light source at room temperature, Copyright © 2008 ACS [321]. (e) Schematic of recombination dynamics of excitons (X), EMP or BMP near bandedge at high excited state to ground state of d–d transition of Co^{2+} ion (blue color) and STE (green color) within bandgap of Co(II) doped ZnSe NR. (f) The electron level potential diagram with atomic coordinates in Co doped ZnSe NR, Copyright © 2021 IOP publishing [216].

Figure 11d show the power dependent ZnS and CdS as 6-fold symmetrical branched NS PL at room temperature. The strong luminescence behavior has been observed with red shift effect ranging from 502 nm to 520 nm that is assigned to band-edge dominant from recombination of exciton or shallow trapped electron pairs of CdS. Moreover, the ZnS and CdZnS bandgap is larger than CdS; thereby CdS related emission is more prominent in the heterostructure as prepared by CVD. The red shift in the spectral behavior is responsible by two factors; (i) excess carrier formation or (ii) trap states formation due to nonstoichiometric sites or defects of CdS at interface. Therefore, the high excitation power responsible for excess carrier generation due to

nonstoichiometric interface and enhance the carrier-carrier scattering that may lead the formation of electron-hole plasma formation at threshold power, so redshift occurs. At low excitation power, the strong emission at 503 nm corresponding to ZnS/CdS interface, because the CdS:Zn layer at the interface may possess slightly larger bandgap and larger radiative recombination efficiency than individual CdS. As the laser power increase, the amount of photoinduced excitons will become larger that move longer distance from interface to CdS ends with redshift effect and broadening of emission line. For high power, another peak appears far from band-edge around 673 nm to 800 nm, centered at 716 nm [321].

Transition metal ion related Luminescence behavior

Figure 11b, c show the ZnSe/ZnS core/shell alloy NC doped with Mn and Cu luminescence behavior. Mn doped ZnSeS alloyed NC phosphine free approach show the successful formation of MnSe nanocluster along with ZnSe/ZnS core/shell (Figure 11b; left). The small size nuclei formation of MnSe need selenium source at 280 C to from MnSe cluster. At the interface of MnSe core, the ZnSe shell formed depend upon growth temperature about 260 C. At 220 C, the third layer of ZnSe coated over the doped NC. The PL emission at 584 nm corresponding to the $^4T_1 \rightarrow ^6A_1$ tranistion of Mn^{+2} ion in ZnSe as discuss earlier [319,322]. The slight redshift in absorption indicate the ZnSe layer grew after each injection of the Zn precursor. The high PL quantum yield achieved because of Mn ion emission centers are isolated from surface defects. Further, the ZnS shell grow to from core/shell nanocrystal show noticeable redshift without alloying between core/shell with PL emission at 595 nm. The absorption spectra show the small peak at 400 nm attributed to excitonic excitation of host ZnSe/ZnS core/shell NC. Similarly, the alloy formation of ZnSeS show the blue shift with spectrum around 350 nm (Figure 11b; right). The Mn:ZnSeS alloy show the Mn related peak at 605 nm with increase in PL quantum yield that indicate the reduce of interfacial scattering in alloy shell [319]. Figure 11c show the Cu doped ZnSe/ZnS core/shell NC and ZnSeS alloy PL quantum yield after 30 days show the green fluorescent material of Cu-doped NCs with high stability. Therefore, the high quantum yield and stability make these NCs suitable for various optoelectronics applications such as bioimaging, LED, and others. Cu:ZnSe d-dots is quenched after two days. Cu: ZnSeS NCs decreased slightly but still high quantum yield then Cu:ZnSe. Cu:ZnSeS/ZnS core/shell d-dots have better stability under air and light with ~90% of the initial intensity under after 30 days. ZnS as shell protect it from outer environment and stabilize the Cu emission NCs [320]. The D states belongs to (i) surface defect (ii) point defect (iii) impurity defects

and X state related with the Co-doped in host matrix (Figure 11e, f) [216]. 1D structure reveals the twin structure (wurtzite and zinc blende) formation during VLS growth as confirmed from structural analysis that might be responsible for D state or above mention defects [209,313]. For doped nanostructure, the dopant ion incorporation in potential valley (green) near the intrinsic atomic potential [224,242,323,324]. At room temperature or above room temperature, the potential barrier overlap that disappear due to mixing of two potential well as shown in Figure 11f. Another reason is the structure twinning formation of such state in potential valley that disappears the energy barrier between two states.

Similarly, the alloy formation of Mn doped in ZnSe/ZnS Type-I core shell NWs through solution process show the different visibility due to bandgap engineering [21,190,317]. Mn doping in ZnSe is another strategy to tune the bandgap in 1D nanostructures and improve overall luminescence of material. ZnSe heterostructure with small bandgap material such as CdSe covers the broad emission spectra and applies in various optoelectronics applications. CdZnSe NWs can be prepared with solution process and physical deposition method by numerous research groups [325–328]. Zn content in heterostructure blue shift the energy of near band-edge and exhibits the donor-acceptor pair recombination corresponding to Zn vacancy near valance band or deep acceptor states and shallow state near the conduction band. Moreover, Cd incorporation in heterostructure is suppressed the Zinc vacancies or Zn defect related emission. Moreover, the adsorption of oxygen or water molecules at the surface of NWs will enhance the photosensitivity due to more surface electrons activating surface resistance. Therefore, depletion layer at the surface of n-type semiconductor will extract more electron than low surface resistance. Such capability of heterostructure device improves the photo conducting behavior along with switching application. Zn chalcogenides alloy and TM ion distribution as prepared by CVD and solution process can be useful for bandgap tuning by controlling its composition ratio, which make Zn chalcogenides quite efficient for various optoelectronics applications such as photodetectors, solar cells and LEDs.

4. Application of II-VI Nanostructure

Binary and ternary semiconductors of Zn- and Cd-Chalcogenide have remarkable physical and chemical properties and popular to possess wide spectrum of electronics and optical properties. Most importantly, the materials belong II-VI semiconductors possess direct band gap along with high optical absorption and emission coefficients. In addition, binary and ternary II-VI

semiconductor alloy are easily miscible, providing a continuous range of properties. Therefore, they can serve as efficient light emitters, such as light diodes and lasers, solar cells, and radiation detectors operating in the range from IR to UV and X-ray. Besides general photovoltaic applications, II-VI semiconductors binary and ternary alloys are also potential candidates for a variety of electronic, electro-optical, sensing, and piezoelectric devices; while the few II-VI semiconductors covers the terahertz range. In particular, nanoparticles of II-VI semiconductors, such as QDs, ID structures, and core-shells structures, can be used for development of gas sensors, electrochemical sensors, and biosensors. As, the device scale down to few nanometer range, the tunable bandgap, high extinction coefficient, possible multiple exciton generation, and unique electronic and transport properties make them highly attractive among research community. Therefore, the preparation methodology, doping concentration and crystalline quality make this class of II-VI semiconductor important over III-V and others semiconductors. Currently, the blended of II-VI semiconductors with perovskite become make new class of hybrid device to achieve high sensing, opto-electronics and bio-medical device applications. In addition to device-centric research, our manuscript also discusses the potential applications of II-VI semiconductor nanostructures in fields such as sensing, imaging, and quantum information processing. Future studies could explore these applications further, investigating new sensing modalities, enhancing sensitivity, or integrating these materials into advanced imaging systems with improved resolution and sensitivity. Moreover, our research underscores the significance of understanding fundamental material properties and phenomena, such as carrier dynamics, spin-related effects, and optical properties in II-VI semiconductor nanostructures. Future studies could focus on unraveling these intricate mechanisms to pave the way for tailored material design and enhanced device functionalities [329–332].

4.1 Photonic and optoelectronics Application

1D nanostructures offer multiplicity of potential applications, especially in photonics and optoelectronics due to their excellent optical properties. 1D nanostructures of II-VI semiconductor has covered wide range of photonic application such as tunable laser lead to white light generation, photonic integrated circuits and many sensing applications. This section will highlights few of them some interesting instances of the applications in complete detail of binary, ternary alloy and TM ion doping in II-VI semiconductor matrix.

4.1.1 LASER

First 1D NW laser demonstrate by Yang and co-worker in 2001 based on ZnO semiconductor [333]. Afterward, number of research groups demonstrate the lasing phenomena in 1D ZnO NWs and NBs. Moreover, the others II-VI 1D system also extensively used for lasing application such as CdS, CdSe, ZnS CdSSe, and others [166,173,334,335]. For 1D structures not only exhibits spontaneous emission but also reported stimulated emission results in optical amplification based on cavity wall act as a reflector. Binary and ternary II-VI materials and TM ion incorporation in 1D nanostructure are promising materials uses as next generation laser application and capability of tunable emission wavelength with integrated devices. Lasing in ZnO nanostructure has been extensively studied due to its hexagonal wurtzite structure and formation of cavity during high temperature growth as reported by various groups [307,336–339]. Gargas et al. has been demonstrated disk shape architecture for low threshold voltage performed the whispering gallery mode (WGM) lasing with low loss in comparison with FP cavity in hexagonal wurtzite ZnO for on-chip nanophotonic integration. Both experimental and theoretical correlation shows that the UV WGM lasing can be achieved from ZnO nanostructure with subwavelength diameters [300,301]. The room temperature emission of single-mode lasing from nano-disks having diameters of 842 nm as excited by optically pump pulsed laser. At low laser pump power, the emission spectra is broad and wide, but as the pump power increase above the threshold value, emission spectra becomes sharp with maximum fwhm value about 0.8 nm. Integrated peak intensity at 391 nm is pump power dependent or in other words threshold value dependent. From experimental result, different diameter of nanodisk exhibits the lasing emission around for 385 nm, to 391 nm is firmly by the overlap of WGM with gain media of ZnO [333,339–341]. Moreover, the lasing threshold is tuned as the function of diameter; large diameter exhibits low lasing threshold is owing to overlap of WGM mode to shift into spectral window of optimal gain. Similarly, the smaller diameter compromises less spatial overlap among the WG mode and the ZnO gain medium. The optical mode diminish confinement causes a reduction in quality factor is owing to the increase of the leakage power. Simulation study reveals the 7.5 % reduction in radiative power lost through substrate that can be improved by 20.7% with taper base increase in Q-factor. Both experimental and simulation based on FDTD show promising outcome for nanoscale laser and on-chip device for nanophotonics [300,312].

Figure 12a show the heavily doped Mn in ZnO show different modes in the luminescence spectra under different excitation power. As, the pump power increases, the carrier interaction become strong with redshift due to amplified spontaneous emission. High excitation power may lead the formation of electron-hole plasma formation that increases the carrier interaction in specific direction to support the lasing mode simultaneously. In comparison with low doping profile (Figure 10), the free exciton emission suppress by strong scattering of impurity ion and phonon. At low pump excitation, the stimulated emission due to exciton-exciton interaction. Further increase in power show the increase in emission intensity that reflects the giant oscillator strength and cooperative radiation of localized exciton. High power excitation dominant the electron-hole plasma formation that redshift with multimode lasing for high Mn concentration. Figure 12b show the low Mn doping profile in ZnO at different fs laser excitation at room temperature as discuss in Figure 10 (peak A and B). The blue shift in the emission is due to phase space filling effect without carrier scattering of exciton at high power. At 4.2 µJ, the coherent transition of bipolaronic state that enhance the intensity and narrow the FWHM of emission spectra. Further increase in pump power (7.5 µJ), the peak energy width of 10.5 meV (second peak appears in emission spectra) assign by dipole-dipole interaction of different coherent states. From experimental result, we emission behavior is similar for low and high doping profile at high excitation with change of threshold power that dependent of doping profile. Secondly, the redshift of peak A happen due to aggregation of neighboring exciton or by screening to enhance the Coulomb interaction between free carriers through bandgap renormalization.
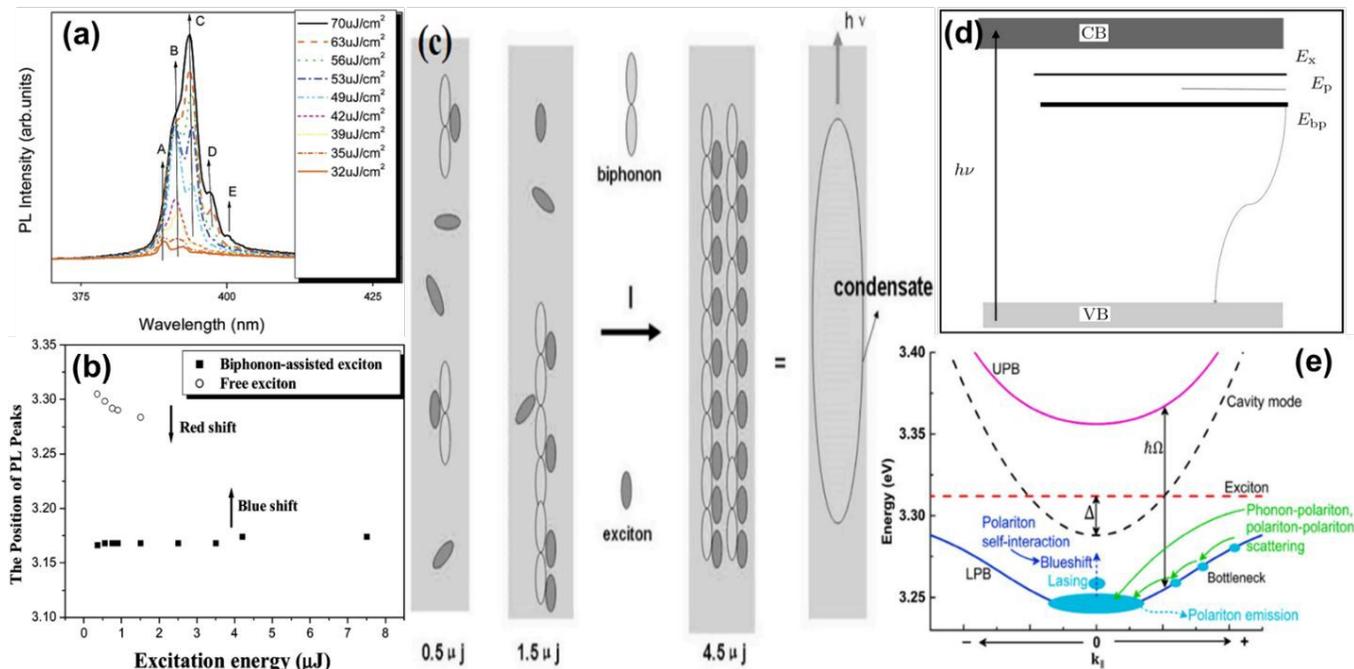
Figure 12: (a) The detailed variation of lasing multi-modes with the pump fluence increase in ZnO nanowires. The direction of arrows shows the increase of pump fluence; the mode marked by arrowhead B appears latter than A with pump fluence increase, and further, the modes marked by arrowheads C, D, and E appear. (b) The photoluminescence peak position from free exciton and 2LO phonon-assisted complex, respectively, showing their dependence on the excitation power, whose magnitude corresponding to the exciton density in the nanowires. Photoluminescence spectra at various pumping energies of ZnO nanowires, Copyright © 2006 ACS Publishing [342]. (c) The electronic states and optical processes of ZnO:Mn nanowires. (d) The dependence of peak positions of the photoluminescence from free exciton and 2LO phonon-assisted complex on the excitation energy corresponding to the carrier density in nanowire, Copyright © 2011 IOP [307]. (e) Schematic illustration of the polariton dispersion, polariton relaxation, emission and lasing process. The horizontal dashed line (in red) shows the uncoupled exciton energy, and the curve dashed line (in black) shows the uncoupled cavity photon mode. The lines represent the upper polariton branch (UPB, in magenta) and lower polariton branch (LPB, in blue), respectively. $\hbar\Omega$ is the Rabi splitting energy. Δ is the cavity detuning, Copyright © 2020 Elsevier [336].

Liu et al. reveals the lasing behavior in Mn doped ZnO due to condensation of magnetic polaronic exciton in 1D NWs prepared by VLS mechanism [307]. To understand the condensation of polaronic exciton, we have to understand the all-possible transition state for host material. For low excitation

power, the exciton and exciton-phonon related peak becomes prominent in the spectra, whereas, the high excitation power the exciton-phonon interaction dominant and originate the polaronic exciton (bound exciton). Lasing phenomena in Mn doped ZnO is owing to bound exciton much likely an emission of Bose-Einstein Condensation (BEC) exciton as shown in Figure 12c. Figure 12d show the change in electronic properties of ZnO with incorporation of dopant ion. Low doping profile show the strong electron-phonon interaction due to 2LO of A1 mode coupled with exciton. FM coupling with coherent exciton show the magnetic polaronic exciton interaction that condensate by fs laser to realize the BEC in real confined space. Another important key factor related lasing is Mn doping in host crystal. High concentration has high lasing threshold value than the low doping samples. Therefore, free exciton, coupled spins and bi-phonon lead to the exciton magnetic polaron formation and condensation related emission are the function of doping and pump power for ZnO:Mn lasing; thereby the intra and inter-band transition need to understand for shift of emission spectra under different condition. Phonon-exciton complex has higher binding energy than free exciton and two-phonon, therefore, both free exciton and bi-phonon related emission appears at low excitation pump power is owing to high thermal stability at room temperature. For BEC existence in ZnO:Mn doped nanostructure existence due to (i) free exciton transform efficiently into bi-polaronic exciton (ii) NW side reflection may confine the high exciton that reduces the diffusion or expansion effect and (iii) aggregation of free exciton with coherent 2LO A1 mode at high density. For 1D nanostructure crystal orientation is also an important factor that can lead the reduction of exciton energy in their attraction interaction and limited the bi-phonon related emission. For parallel orientation, the dipole repulsion increase the exciton energy that exhibits the redshift at low excitation pump power. Meanwhile, coupled exciton aggregate and related repulsion increase at parallel orientation will enhance the bipolaronic exciton at high density is characteristic of dynamics BEC emits light coherently without other available states [5].

Optical characterization tools such as PL provide suitable exciton information under different powers. For low Mn concentration, the free exciton are depleted by coupling of LO phonons and spins ions at high power that may leading to the formation of EMP in large exciton binding energy and strong electron-phonon coupling semiconductors such as ZnO. Strong exciton-phonon coupling materials normally reflected an increase in LO mode phonon by adding impurity ion. Thus, the LO phonon mode coupled with bound exciton expresses the polariton-exciton emission. For Mn:ZnO exhibits the EMP corresponding to 2LO-exciton state at low excitation energy due

to multiphonon exciton but 3LO and LO coupled exciton emission band not coupled with free exciton. EMP is attained higher thermal stability due to high exciton binding energy than thermal energy (26 meV). High exciton binding energy semiconductors possess higher stability of exciton-phonon coupling and exciton-spin interaction at room temperature. High doping concentration enhances the exciton-phonon coupling and increases trapped states with bandgap. Under such conditions, the emission spectra reflect the forbidden selection rule for one-phonon transition and allow two-phonon transition or facilitate the bi-polaron process that may lead to non-linear interaction in 1D structures. Therefore, the bosonic nature phonon and exciton dominant the coherent excitonic state of bound exciton in polar semiconductor prevailing the EMP emission. EMP peak show fast enhancement, narrowing FWHM and slightly blue shift under power influence due to exciton-exciton interaction and coherent two-phonon-exciton coupled with spin. Bi-polaron exciton transformation in 1D nanostructures is produced by temporal, coherent and high-density exciton as excited by fs laser. High-density exciton in 1D dependent on crystal face reflection or aggregation of free-exciton perform coherency in specific orientation or crystal direction. For wurzite structure, the polarization of light-matter interaction show the orientation dependent exciton emission due to change of dipole force along parallel or perpendicular direction. For spin dependent semiconductors, the FM spin exchange coupling in magnetic field change the dipole force and aggregation of exciton or spin ion responsible for EMP formation in 1D nanostructures. Therefore, bi-polaronic exciton aggregate at high density emits coherent light, which resembles a characteristic of dynamic exciton BEC state (some like Cooper pairs in a superconductor) in a semiconductor 1D NW structure. Recently, Zou et al. explained the identification of coupled spins in 1D NWs and its origin. With magnetic measurement, the origin of FM coupled with spin inside the host lattice is doubtful. While, the ns time-delay PL spectra provide the PL relaxation to the local d-d transition. Strong electron-phonon coupling and spin ion in host lattice indicate the FM coupling in polariton-exciton emission with energy position indicating origin of ferromagnetism in DMS. Moreover, NW cavity demonstrate that exciton decay into a very narrow mode of coupling which strength enough to produce polariton lasing and polariton condensation in 1D nanostructures. This long-range elementary excitation has spin-polarized character, and can give collective EMPs condensate at high density. For QDs, EMP can even be easily formed, but without long-range LO phonon coupling as observed difference in PL behaviors. PL can be able to identify the spin ion FM coupled aggregate d-d transition in 1D

structure with slightly redshift with its FM spin cluster. Such type of cluster in 1D nano/micrometer sized structures favors the EMP formation and give strong single mode lasing from the BEC-like state of collective EMPs in DMS structure [5]. Zhao et al. achieved the low threshold lasing in thin 1D pure ZnO NW WGM at room temperature through surface Plasmon promoted by single mode polariton [336]. Figure 12e shows the schematic diagram of polariton dispersion for lasing corresponding to relaxation and emission of coherent plasmon-polariton in cavity mode ZnO. The horizontal dashed line (in red) shows the uncoupled energy (exciton energy), and the curve dashed line (in black) shows the uncoupled cavity photon mode. The upper polariton branch (UPB, in magenta) and lower polariton branch (LPB, in blue), respectively show the Rabi splitting energy ($\hbar\Omega$) and cavity detuning (Δ). Nano-laser of ZnO NW on graphene-insulator-metal platform exhibits gate modulated lasing based on surface Plasmon polariton sensitive to cavity effect. The electric field distribution on integrated circuits at nanoscale have potential application as function of gate voltage. Under applied voltage, the electric field is shifted away from the metal surface that result internal loss of lasing. Therefore, high-applied voltage modulate low lasing threshold and vice versa. The PL related peak intensities that is obtained in the repeatability test over five periods, where VG set as 6V and 0 V in the on-state and off-state, respectively, and the switching period was 1 s. Each positive cycle of 6V, the on state accumulate the surface electron at the metal surface that may increases the plasma frequency at metal side and resultant is internal loss of surface Plasmon polariton mode at fixed pumping power. Therefore, the lasing signal could be dynamically modulated by gate switching [343].

4.1.2 Solar Cell

Solar cell convert the light into electricity through excitation of e-h formation in semiconductor. Currently, the solar energy major source is Silicon base solar cell having efficiency around 25 % but expensive manufacturing cost. Therefore, others materials such as II-VI semiconductors are introduced for high efficiency, cost effective and low manufacturing cost. So, the 1D II-VI nanostructure are highly crystalline, large surface to volume ratio and photo-active in wide range spectrum (form UV to IR regions) and consider the next generation photovoltaic devices [16,31,39,344]. Law and co-worker reported the organic, organic and inorganic hybrid and dye-sensitized cell for solar energy conversion based on ZnO NWs, ZnO particles and TiO$_2$ particles [345]. Figure 13 show the vertical align ZnO NW array for dye-sensitized cell scanning electron microscopy cross-

section image on FTO. Moreover, the NWs are in direct contact with the substrate and no other intervening particle layer present. ZnO NW array compare with NP in Figure 13b, where light intensity is the function of short-circuit current density, and efficiency of two solar cell. Array like structure provide direct charge extraction but more trap directly effect on transport of carrier as discuss above. Also, the array like geometry allow the formation of full depletion layer at semiconductor-electrode interface that may leading the formation electric field assisted charge separation which provide better charge transport in comparison with NPs. Another factor that directly affect the performance of solar efficiency is the surface roughness. NW array of ZnO has less surface roughness in comparison with NP film. Therefore, the low surface roughness, high trap occupation density and low light absorption than film like structure provide more efficiency for vertically align NWs like structures as shown in Figure 13c [302,345].

Tang et al. reported the single CdS NW show good response than planar devices [55]. High crystalline single CdS radial NW p-n junction exhibits the 0.6 V open circuits and 80% fill factor as shown in Figure 13f. CdS/Cu$_2$S core-shell NWs show higher values than planar devices at low open circuit voltage with reduced light intensity (Figure 13d-e). Interfacial junction between core-shell materials should be high quality and VLS mechanism should provide the high crystalline interface between CdS/Cu$_2$S that calculated the overall efficiency of 5.6 % with lower current density (Figure 13g, h). Moreover, the solar cell efficiency also dependent on the thickness of shell materials; the increases of shell thickness would lead the absorption within the interface as well as the efficiencies of radial solar cell. Additionally, horizontal devices has ability to study the uniformity of charge collection as function of orientation and single NW. For this purpose, the scanning photocurrent mapping (SPCM) of horizontal NW demonstrate that core-shell region is more active for charge separation, while edge exhibits the sharp drop-off. Radial p-n junction has benefits of charge collection from CdS that suffers from low minority diffusion length. Moreover, multiple devices for parallel and series configurations on core-shell single NW provide flexible absorption range at low cost and better photonic device performance than planar device. CdS/CdO core shell and other ternary II-VI nanostructure are potential material for future photonic application [75,174].
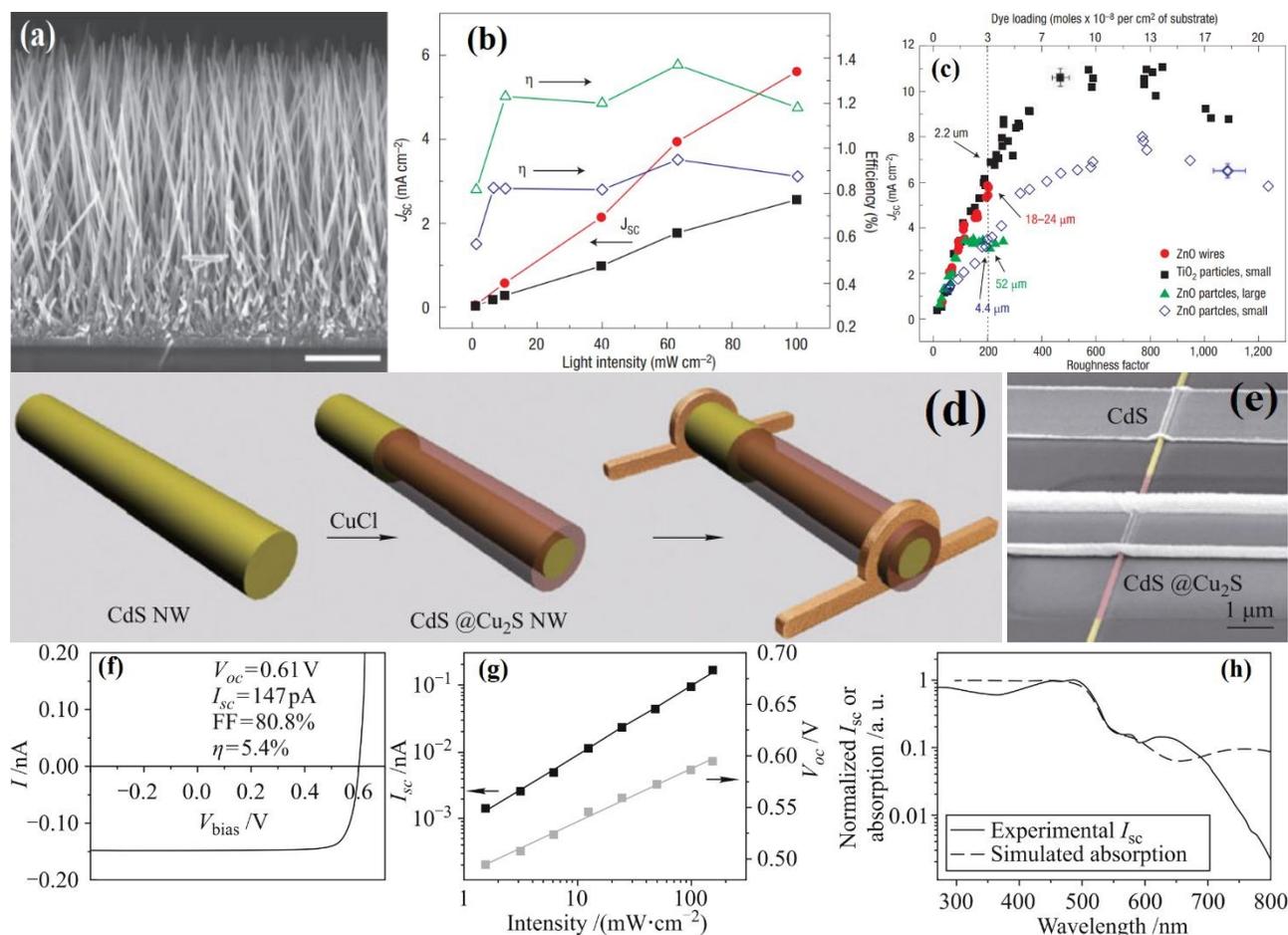
Figure 13: (a) ZnO nanowire array for dye-sensitized cell scanning electron microscopy cross-section image on FTO. The wires are in direct contact with the substrate, with no intervening particle layer. (b) The short-circuit current density and efficiency against light intensity for cells with roughness factors from 75 to 200. Each of the four parameters is represented by data from two different devices in order to provide an estimate of the range of their variability. Active cell size: 0.8 cm^2. (c) Short-circuit current density versus roughness factor for cells based on ZnO wires, small TiO$_2$ particles, and large and small ZnO particles, Copyright © 2005 Nature [345]. (d) Schematic diagram of Core-shell CdS/Cu$_2$S single NW. (e) SEM image of a single NW. (f) I–V curve of a single-NW under 1 sun (AM 1.5 G) irradiation. (g) Variation of I$_{sc}$ and V$_{oc}$ on light intensity (h) Wavelength dependence of photocurrent compared with simulated absorption, Copyright © 2011 Nature [55].

4.1.3 Photodetector

1D nanostructure has gained much attention due to their unique optical and electrical behavior at nanoscale. High surface to volume ratio and improved crystal quality provide additional benefit to charge carrier transportation for photoelectric device. 1D nanostructure based on CdS, ZnO, CdSe, ZnCdSe and others II-VI semiconductor has been used for tunable photodetector [201,346–348]. The synthesis of $Zn_xCd_{1-x}Se$ alloyed NWs for variable wavelength detection synthesized by CVD method. Yoon and co-worker successfully shown the tunable emission by adjusting the composition gradient as discuss above but only they first claimed the successful representation of wavelength controllable optoelectronic device of II-VI ternary alloyed NWs [328]. CdSe show slow response is owing to adsorption of ambient gas molecules at the surface like other n-type semiconductor (like ZnO). Thus, capture of oxygen ion at the surface generates depletion layer from the surface or increase resistance that is responsible for slow response time other than ZnSe and $Zn_{0.72}Cd_{0.28}Se$, respectively. Both other photodetector has less active surface to ambient environment and practically applicable to variable wavelength photodetector covering the wide range of visible spectrum ranging from blue to red [328]. Figure 14 show the CdSSe ship sensor respond to moisture, the humidity dependent I-V curves in dark and light condition under bias condition shown in Figure 14a, b. At 5 V (dark), the current increases from 3.36×10^{-7} to 1.15×10^{-6} A with the relative humidity increasing from 25 to 80%. Under illumination, the photocurrent changing from 7.48×10^{-6} to 1.38×10^{-5} A. The inset show the IV characteristics response under different moisture condition. The polyimide (PI) on the surface tighten the contact between CdSSe NW layers and under proper bias voltage give good response in light and dark (Figure 14c, e). Figure 14d show the resistance of the sensor for different humidity level show the linear dependence for both dark and light suggest the feasibility and convenient to predict the humidity of moisture. The relative humidity of moisture dependent resistance in the dark field can be well fitted with a linear function ($R_2 = 0.9779$) and with illumination ($R_2 = 0.9948$) [188,189].

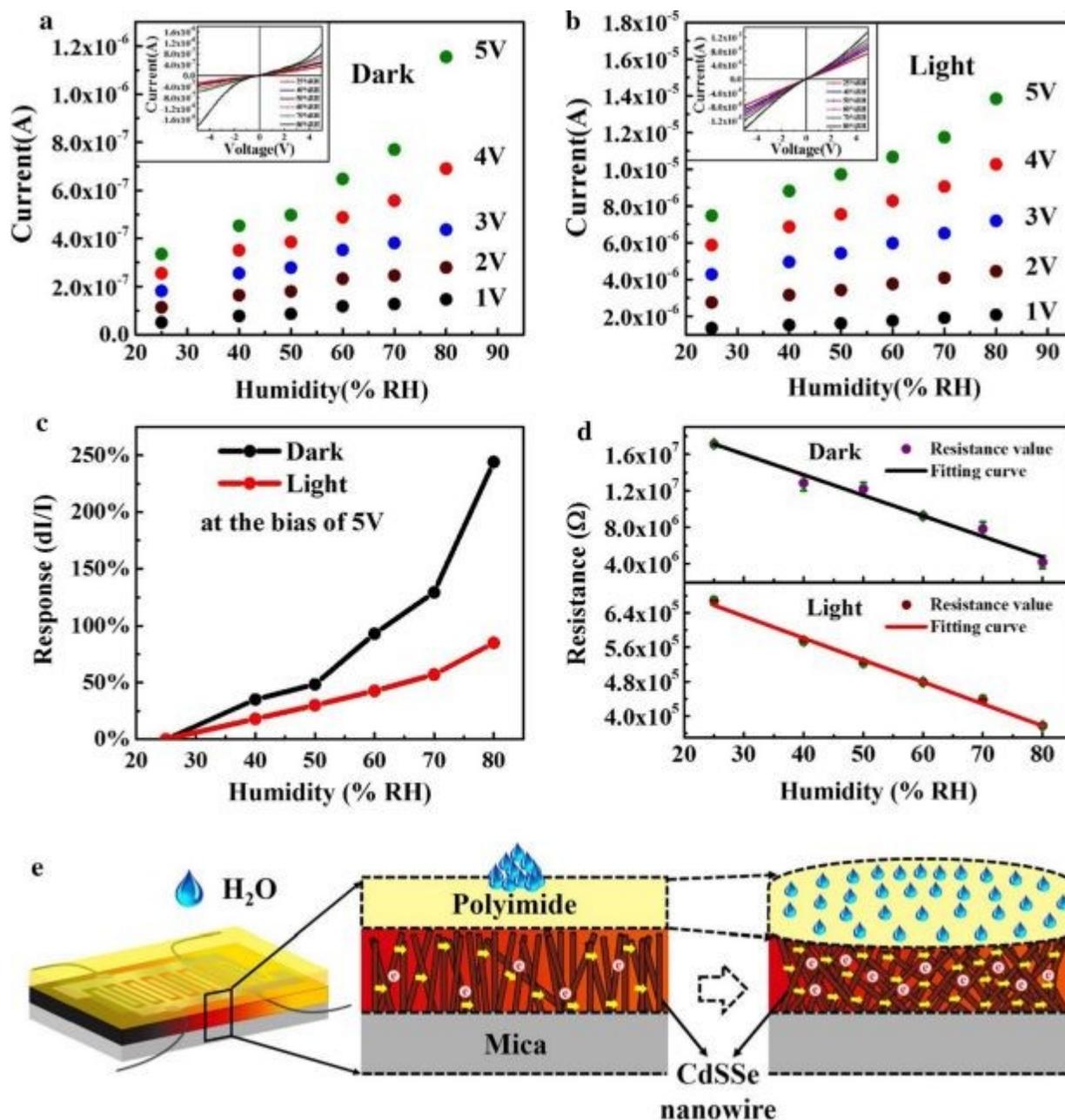**Materials Advances Accepted Manuscript**

Figure 14: (a) Dark current (b) photo-current at various humidity levels under different bias, inset of IV characteristics in the dark (a) and light (b) surrounded by different relative humidity. (c) Relative humidity dependent moisture responsivity of the sensor in the dark and bright felds, respectively. (d) Resistance at various relative humidity of the sensor in the dark and bright felds, respectively. (e) The schematically theoretical diagram of humidity sensing of the sensor [188].

Recently, many groups working on flexible photodetector based on 1D and 2D structure. For II-VI 1D nanostructure both ZnO and CdS has many articles related its photo detection properties

depend upon (i) composition gradient (ii) doping incorporation and (iii) synthesized mechanism. 1D CdS NW and WSe$_2$ 2D flakes use on substrate for photodetector by Lin and co-workers [347]. Both Lin and Du highlighted the importance of Van der Waals heterostructure growth [347,349]. Xiong group for the growth of various II-VI semiconductors nanostructures has reported Van der Waals epitaxial growth by VLS mechanism extensively [10]. The photo response as the function of time and illumination intensity. As, the illumination intensity increases, the photo response of the device is decreasing due to interface trap states. The I-t characteristic curve show the stability of photodetector under different illumination intensity at fixed bias condition of $V_D = +2$ V. Inset of Figure show the response time is less than 1s, switching behavior retain after multiple cycle test under strain. Similarly, the light and without light I-V characteristic curve for flexible photodetector under different strain and inset show the difference of strain on the output characteristic curve of photodetector. From these results, CdS NW current increase under illumination but no such impact of strain on the performance of device. Lou et al also fabricated the 1D ZnO-SnO$_2$ photodetector for UV photodetection on PI substrate [350]. ZnO-SnO$_2$ devices show excellence UV photodetection under ambient condition. Both materials conductivity improve due to oxygen at the surface enhance the carrier response that may improve the high I_{ON}-I_{OFF} ratio, fast response time and good reversibility [350]. Moreover, the Yang et al. reported the ZnO NW covers the broad range of spectrum detection under different laser excitation and exhibits the ultrahigh sensitivity, fast response speed and good flexibility for future optoelectronic circuits, switches and so on [60,301,351]. Guo et al. synthesized the highly crystalline tin doped CdS NW for tunable optical loss and multi-band photodetection by using CVD method [96,173,188]. CdS NWs show pump power dependent propagation loss of near band edge emission and defect related emission. At low temperature PL measurement, the calculated activation energy is 34.29 meV that illustrate carrier decay owing to exciton recombination. High photoresponse (51.2 A/W), high gain (313.3) and stable optical switching at $V_{DS} = 3$V reveals the importance of 1D II-VI semiconductor for integrated optical interconnection chip design [96]. Lieber et al. CdS NW on Silicon produces nanoscale injection laser to covers the wide range of spectra but also integrated as single or multiple color laser in silicon microelectronics and single wire on-chip devices [40,352–354]. CdS single NWs has high injection rate due to cavity formation and same issues can also be address by axial composition, core-shell heterostructure, composition gradient and TM ion doping or metal doping at the surface of 1D nanostructure. Moreover, the radial p-n junction of n-CdS and p-Si

NW for avalanche photodiode demonstrates ultrahigh sensitivity with detection limits of less than 100 photons for ultra-dense integrated systems, sensing and imaging applications [353].

4.1.4 Waveguide

II–VI 1D nanostructures is functionalized to confine and propagate electromagnetic waves into specific directions. II–VI semiconductors covers wide range of spectrum along with large dielectric constants and refractive index than their surroundings that allows the light to transmit with low loss through total internal reflection. Such inherent properties make II–VI 1D nanostructures suitable for various optical application at nanoscale. Moreover, ternary alloy of 1D II–VI semiconductors reveals bandgaps engineering as well as metal ion doping with large dielectric constants and higher refractive index facilitate the propagation in unified direction. Several groups demonstrates waveguides behavior in II–VI 1D binary, ternary and metal dopant in II-VI nanostructures in last decade. Pan et al. show the single crystalline NB of CdS exhibits the waveguide behavior prepared by CVD method [77,175,355]. Johnson, et al. and others described the significance of ZnO NWs in wave guiding behavior, whereas simultaneously behave as optical cavities (like FP cavity) and presence of flat and parallel end faces act as reflector [333,340,356]. Lieber and co-worker presented the future prospective of CdS NWs that entertain a single wire as active photonics circuit elements for guiding light at sub-wavelength scales. [352,354,357] Active wave guiding in 1D NWs are operated near the band edge demonstrated by the Zou group for CdS nanoribbons and CdSe NWs [89,175,355,358]. TM ion doping or metal doping (such as tin) enhanced the cavity emission near IR related with metal ion [89,96,359]. Figure 15a shows the waveguide demonstration of CdS_xSe_{1-x} nanoribbons and Figure 15b show the branched NW emission spectra. Figure 15c shows the PL emission spectra recorded different marked points in Figure 15b. The light is emitted in the wide spectrum range in one branched NW; one end is excited with band edge emission and light propagate along it; while other end of NW act as waveguide mode. Moreover, the emission is only seen at the extreme end of branch NWs that indicates the guided nature of light as shown in Figure 15a, the magnitude of the redshift in the spectra is strongly related to (i) composition gradient and (ii) crystallization degree of the nanostructures at nanoscle. Figure 15c shows that different emission in branched CdS_xSe_{1-x} nanoribbons is related with above mention points. The understanding of waveguides in 1D NWs/ribbons offers the opportunity of using it in

highly integrated and compact photonic circuits with improve speed limitation and power dissipation in current electronics. Therefore, the manipulation of light from UV to IR spectra helps us to develop favorable single NW integrated photonic circuits of binary, ternary and metal ion doped II-VI materials [78]. Figure 15d show the optical waveguide in straight, bent or kink CdS NWs reported by Lieber group using scanning optical microscopy [352,357]. Light propagation through single structure only show moderate loss through sharp and acute angle bend due to (i) surface roughness or (ii) change of refractive index at interfacing angle.
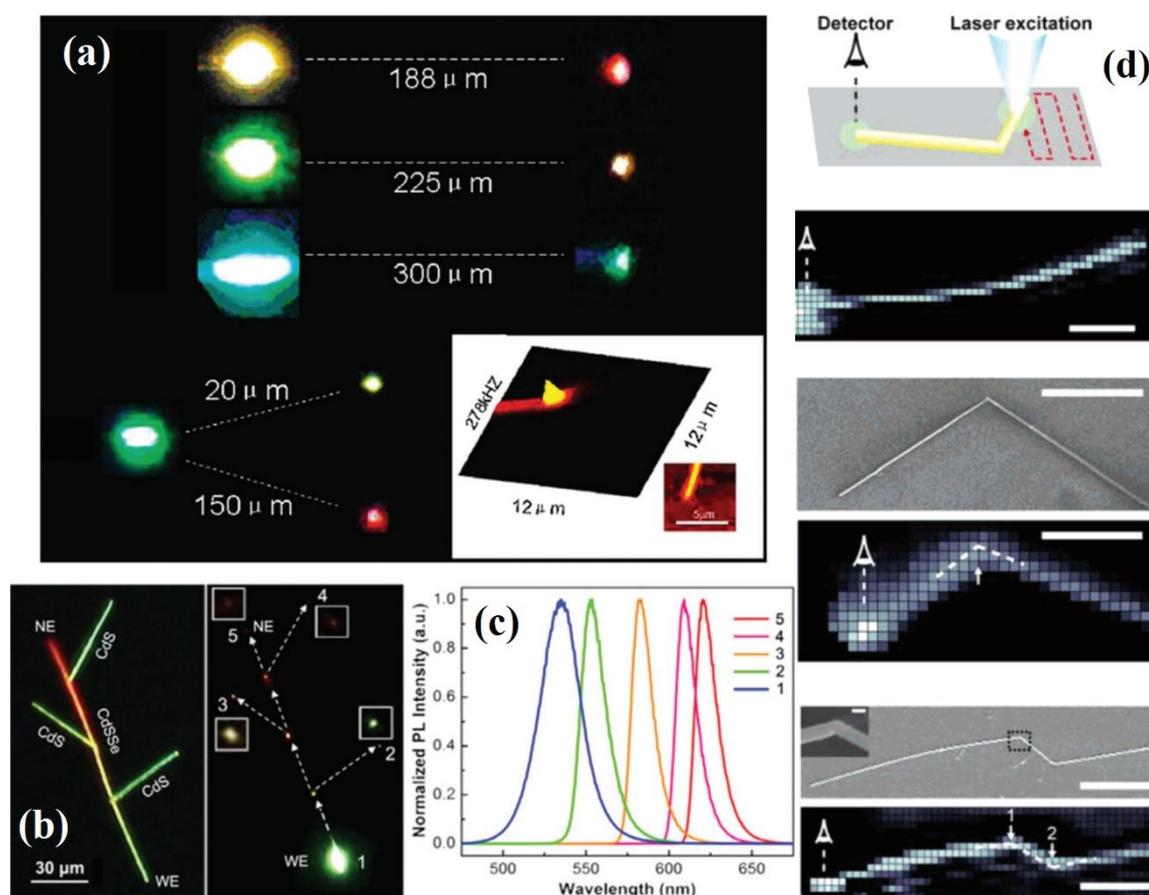

Figure 15: (a) Waveguide demonstration of CdS_xSe_{1-x} nanoribbons. Copyright © 2007 American Chemical Society. (b) Selective waveguide from the branched architecture of the CdS_xSe_{1-x} nanostructures and (c) PL spectra of mention location in (fig. 15b), Copyright © 2012 American Chemical Society [78]. (d) Characterization of optical wave guiding in straight and bent nanowires. (Top) Schematic diagram (2nd) scanning optical microscopy (SOM) illustrating focused laser spot scanned over the sample while monitoring light emission from one end of the nanowire. (3rd) SEM image of a single CdS nanowire (4th) corresponding SOM image. (5th) SEM image of a single kink

CdS nanowire (Last) corresponding SOM image under different position (Mark 1 and 2), Copyright © 2004 American Chemical Society [352].

For wide bandgap with cylinder geometry or hexagonal structure with large dielectric constant show good waveguide nature with Sn doping in CdS that activate as superlattice 1D nano/micro-wire as shown in Figure 16a. Inset shows the optical micrograph of Sn doped CdS. Its optical behavior shows much like 1D photonic crystal (PC). Figure 16b show the schematic diagram of CdS/CdS:SnS$_2$ junction within single wire like structure. CdS segment in superlattice wire confine the transport photons; while large refractive index of SnS$_2$ act as reflector to trap the light within optical micro-cavities. Periodic bright emission arise from the interference of coherently scattered light wave within coupled cavities not related with Fabry-Perot mode (Figure 16c-h) [194]. The different emission modes with varied wavelength can be imaged with this 1D PC, to behaved local photon bunch. Each single mode comes from the neighboring two cavities, and can propagate in a very long distance. Their macroscopic mode number can follow the Bloch oscillation character in their broad emission range, which indicate a strong nonlinear photonic structure for exciton-photon interactions. Moreover, the Sn (IV) incorporation in CdS lattice show the bandgap edge and trap state emission due to nonlinear electron-phonon coupling or anharmonicity effect. Exciton trapped by local impurity states related to paired states or deep trapped state involve different recombination rate of relaxation as shown in Figure 16i [194,196,359]. Similar behavior of color-tunable period spatial emission is observed in ZnO/FeZn$_2$O$_4$ and CdS$_{1-x}$Se$_x$/Sn:CdS$_{1-x}$Se$_x$ superlattice by varying the composition gradient from 0 to 0.4 [96,196,360–362]. The light transports along the axis and is periodically emitted at the adjacent joint segment. The change of the refractive index of CdSSe and Sn formed the neighboring alloy segment, which acts as microcavity through reflection interface where partially light leaks through the joints. The periodic bright emissions arise from the interference of coherently oscillated light within the coupled microcavities, producing the multi-peaks at the low energy side. The strong absorption above bandgap cannot transport long within the wire, so it cannot produce waveguide modes. Figure 16i shows that PL emission exhibits strong band edge emission at ~551 nm and several accompanying shoulder related coupled cavity modes. The mapping profile of the wavelength range 606-626 nm is shown in Figure 16h. The photonic modulation and possible exciton coherent emission are combined in different optical microcavities. Thus, we can accomplish that these emission contours were produced by the

combined contributions of coupled optical microcavity modes and local excitons within this 1D photonic crystal wire [362].
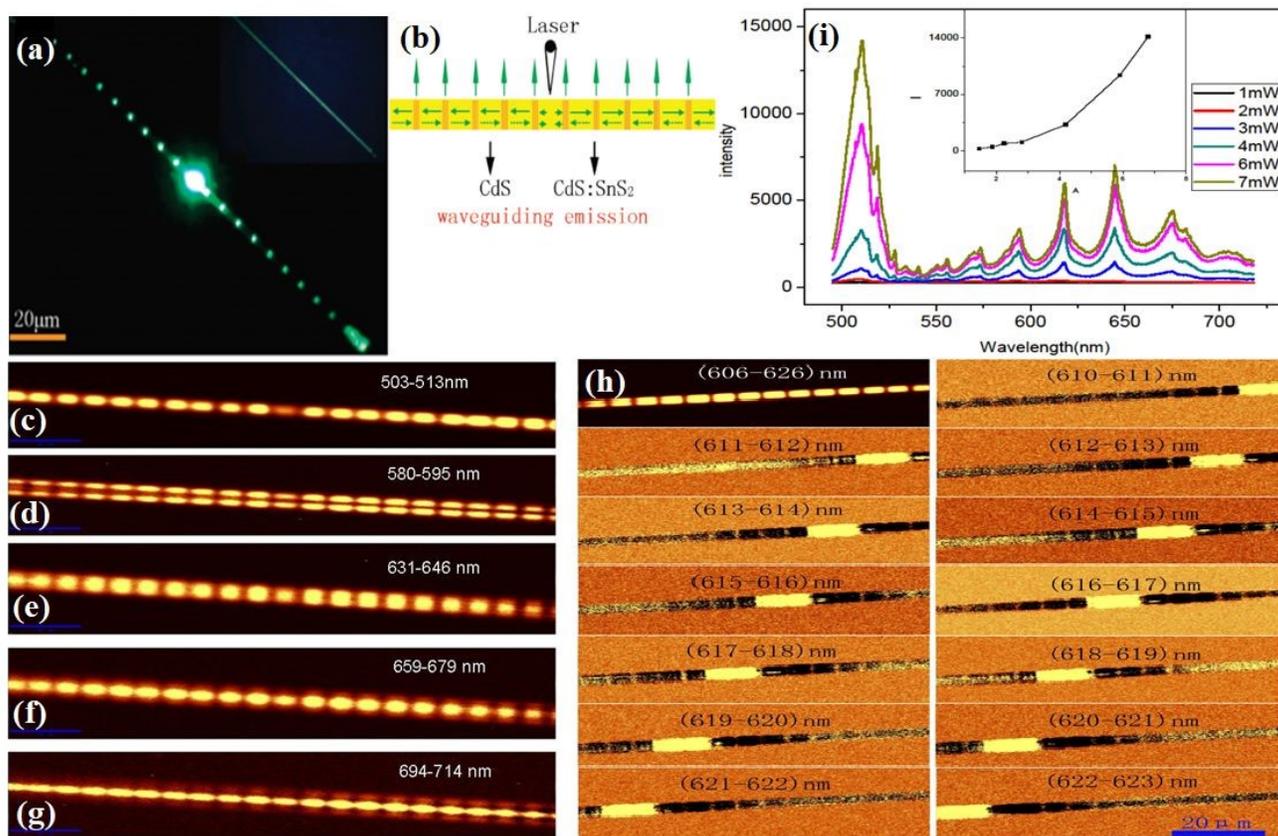

Figure 16: Far-field PL images of an excited sample with different reaction times: (a) 20 min; (b) 30 min. Insets in (a) and (b) are corresponding optical images. (c) Schematic representation of emission process of the 1D superlattice wire, Copyright © 2010 American Chemical Society [194]. (d) Schematic diagram of the branched nanostructure of 355 nm laser incident (inset is the optical microscope image); (e–g) Real-color dark-field photograph under the illumination of the 355 nm laser with increasing pumping power density, with a scale bar of 20 μm Copyright © 2012 Wiley-VCH.

Branched like nanostructure are extensively used for various application as suggested by Lieber and Yang group. Liu et al. also show the nanoscale laser array of branched like structure of CdS doped with Sn as shown in Figure 17a-d. Sn act as the junction that split into multichannel nanostructure and demonstrate as the effective light confinement and oscillation. Under excitation, strong band-edge emission and Sn reflected light scattered out of the branch segment. Thus, the

oscillation of light within branch and trunks show the multi-point lasing of high quality factor up to 990 with low threshold. Waveguide performance of the hierarchical trunk-branches CdS NWs array excited by UV light shows the bright green emission that propagates along the branch and emits from tips as shown in Figure 17b. As the central part is excited, the light propagating from tips of branches is stronger than the trunk-branch (Figure 17b) due to propagation distance, as shown in Figure 17c. From Figure 17b, c, the branch-like structure shows the waveguide nature, and the propagating distance shows the marginal damping in emission. The trunk excited shows the efficient light coupled between the trunk and branches in a monolithic structure, as shown in Figure 17d. Such exceptional optical coupling motivates optical integrated device applications such as active waveguide trunk−branch cavities for 1D NWs to hundreds of branch wires [89,96,100,359,363].
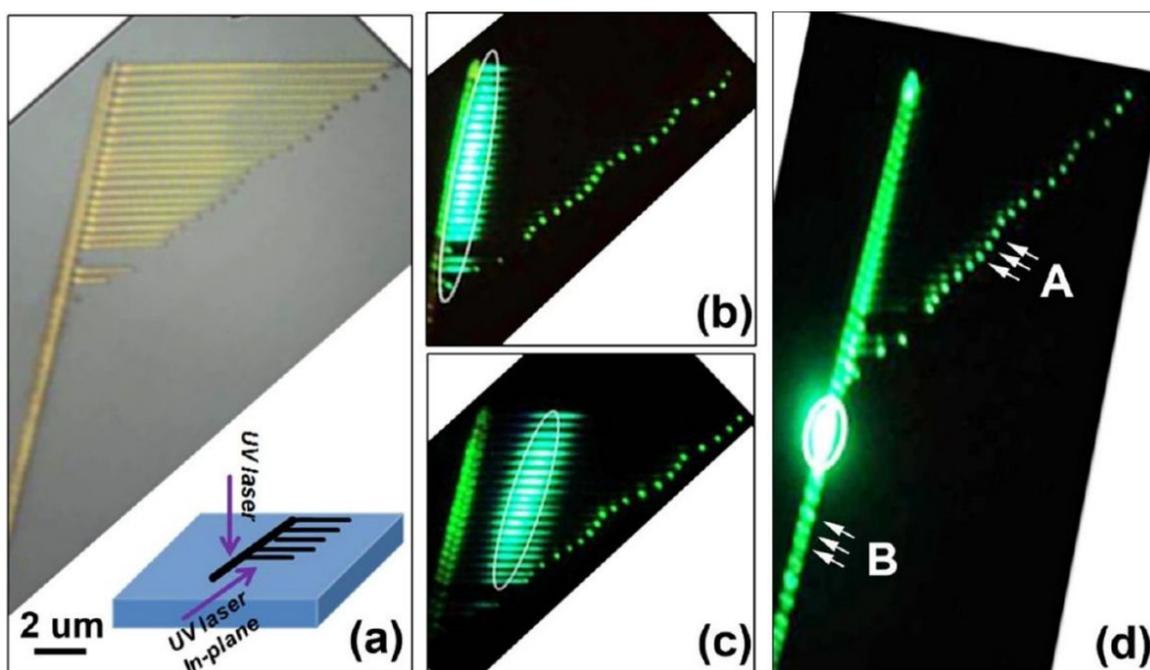
Figure 17: (a) Optical microscopy image of the yellowish CdS comb structure on a Si wafer. The inset schematically shows the different illumination directions and areas of the UV laser (GaN laser diode at 405 nm wavelength). (b) Green photoluminescence with lateral (in-plane) illumination collimated at the trunk−branch junctions, (c) at the central part of the branches, and (d) vertically collimated as indicated by the white ellipses. Note that the arrows marked by B indicate the periodic emission of light resulting from the Fabry−Perot cavity for lasing; the arrows

marked by A indicate the light emission from the end-tip of the branches, Copyright © 2013 ACS publication [89].

4.1.5 LED

II-VI semiconductor 1D nanostructures show good electricity drives and light emission due to carrier injection through radiation recombination. For homoepitaxial growth of same II-VI material show poor performance as reported in ZnO. Although the lattice mismatching related defect overcome in homostructure growth but overall performance compromise. Most of research available for LED formation in II-VI materials based on growth mechanism and dimensional growth [364]. Radical heterojunction and homojunction device performance is quite better than other 1D growth. Major research related LED is reported for QDs, NCs and NPs related heterostructure of binary, ternary and metal ion dopant dependent. QDs based ZnSe/ZnS core-shell Type-I exhibits the high quantum yield ranging from 45 to 65 % [365,366]. ZnSe/ZnS NRs Type-I show 50% quantum yield for heterojunction having emission wavelength 421-485 nm [367]. For Type-II, CdSe/Te NW core-shell like structure quantum yield is about 20-60% and cover wide range of spectrum 530-760 nm [368]. Similarly, type II double shell structure of ZnSe/CdS/ZnS have quantum efficiency 43-61 % for broad-spectrum range of 470-760 nm [369]. 1D growth of NWs and NBs like structure make junction with other nanostructure or grow of substrate for display and electroluminescence. ZnO, CdO, are normally exhibits the n-type conductivity; CdTe and ZnTe are inherently p-type conductivity semiconductors. Therefore, the junction for electroluminescence study must be among II-VI n-type conductivity materials with p-type or p-type III-V semiconductor like GaN [370,371]. So, electroluminescence in II-VI has great deal of attention and easily integrated with electronic devices for wide range of LED, display panel and etc. 1D II-VI nanostructure has advantages over other synthesized growth dimension that direct bandgap can be tuned by their large bandgap coverage, tunable bandgap, large aspect ratio, small size, and high crystalline quality. Tunable bandgap emission facilitates to cover broad-spectrum range from UV to IR. Their large aspect ratio can encourage the influence of their device integration and their small size can generate a smaller emission beam spot; which can facilitate the higher display resolution. In addition, their high crystalline quality progresses the proficiency of radiative recombination. In spite of advantages, the only challenge currently face is improving conversion efficiency and device stability. Lieber and co-workers have comprehended explain the n-CdS NW on a p-Si

substrate green emission is owing to FP cavity modes formed inside the NWs during growth in VLS mechanism. Green light lasing of n-CdS NW heterojunction with p-Si show good conversion efficiency [334,352].
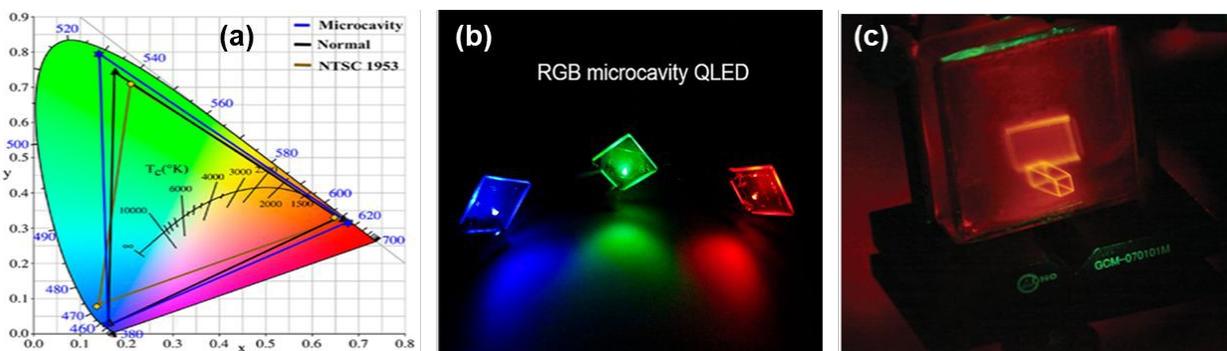

Figure 18: (a) EL performances of best performance RGB QLEDs. (a) CIE characteristics. (b) Image of RGB MQLEDs, Copyright © 2020 ACS publication [372]. (c) Digital camera images for holographic reconstruction of cuboid under room light, Copyright © 2014 Wiley-VCH [373].

The electroluminescence (EL) of CdSe/ZnS QD (QLED) and multilayer micro cavity based QD (MQLED) used to study the performance of green and blue LED (Figure 18b-c). MQLED CIF diagram show efficiency achieved for different colors for RBG (Figure 18a). The significantly improved optoelectronic performances of MQLEDs demonstrate that the optimization of optical properties plays the same important role in determining the EL performance as that of electrical properties. Meanwhile, microcavity structure can be applied in low-threshold laser, cavity quantum electrodynamics, biological detection, and high-performance filters. Further improvement in its Q value can lead to an extremely narrow FWHM and a low-loss optical resonator, which indicates that a high Q microcavity is a promising and practical structure for achieving electrically pumped QD lasers [372]. QDs as display medium for holographic 3D applications with hydrogel composites exhibit very attractive properties such as high transparency, highly saturated color, fast response, low cost, simple process as well as scalable and healable characteristics. From results, the fabricated PVA hydrogels with different QDs are potential smart display mediums for colorful, real-time 3D display and potential in other intelligent optical devices [373].

4.2 Electronic and Sensing Application

4.2.1 FET

Field effect transistors (FETs) are building blocks in many devices such as integrated circuits, digital data storage devices and flat panel displays. FET device fabricated from 1D single nanostructure such as NWs/nanoribbons has been established to demonstration superior performances owing to its high crystal quality, reduced phonon scattering, device material decoupled from substrate material, large surface-to-volume ratio and quantum confinement [14,18,39,374]. Jie et al. fabricated the CdSe NR on SiO_2/p$^+$-Si for single nanostructure FET on substrate and measured the gate dependent current and voltage relation also known as gating effect [375,376]. The conductance of nanostructure increases with increases of gate voltage for n-CdSe is owing to selenium vacancies. Under illumination, the generation of e-h pairs significantly increase the conductivity that is related with carrier concentration increment under light, which may shifts threshold voltage in negative direction along with decrease of on-off current ratio. Moreover, 1D system has high surface to volume ratio that directly affected the transport properties by the surface absorption and desorption of atmosphere. Surface absorption from atmosphere increase the resistance or in other words depletion layer is formed near the surface that decrease the carrier concentration/ conductivity under bias condition. So, 1D nanostructure can be effectively utilized for gas sensing, chemical sensing and biological detection. Binary and ternary II-VI materials single nanoFETs has been extensively used for potential application [377–382]. Nano-network FETs or integrated nanoFETs are promising materials for logic circuit, storage and sensing application. Figure 19a show the schematic diagram of CdSe nanoribbon as logic circuit in which the real intensity measurement system with the fiber tips together with a photomultiplier tube as detector units attached around the single structure. Upper inset (Figure 19a); the dark field image of a square nanostructure having size of 25 × 25 μm. The fiber tips with diameter 250 nm has been arranged around the nanostructure. Lower right inset (Figure 19a); show the schematic diagram from the top view measurement. Emission intensity at the edges is position-dependent that changes along the top edge (Black Square) and right-side edge (red circle) clockwise, respectively as shown in Figure 19b above threshold intensity level. The first four columns represent different excitation position, (1000) for region I, (0100) for region II, and so on. The columns with number from 0 to 7 represent actual emitting-out states at eight different edge positions corresponding to the different excitation regions. In each table unit, the real emission intensity is given in brackets as shown in

Figure 19c. Therefore, the directional light propagation and its emission along normal and perpendicular axis to form the localized light selection. Based on light distribution pattern guided rule, optically logic encoder has been developed successfully by Li et al. The basic logic element '1' is defined by the real intensity of the illumination part being higher than the threshold, while '0' corresponds to the dark noise level [383]. The large high-intensity difference assurances the validity of a signal for communication. Moreover, integration of nanodevices demonstrated by Ma et al. in which nanoinverters with a high voltage gain has been fabricated by combing two CdS NW MESFETs for NOR and NAND gates as integrating devices [379]. He et al. also described the realization of logic circuits by synchronized two top-gate CdSe:In NW FETs, which are proficient improve the inherent photoresponse properties of CdSe NWs [378]. The I_{DS}-V_{GS} curves of two gated FETs show the hysteresis sweeping rate of 6 V/s. Series and parallel connection of two gate FETs act as basic logic circuit of 'AND' and 'OR', respectively. The logic circuits demonstrated great performance gain, stability, operational speed and high reproducibility. CdS_xSe_{1-x} nanoribbon with lateral heterostructures demonstrated as high-performance photo-detection with higher I_{ON} - I_{OFF} (10^6) [73]. Li and Junpeng also reported the CdS_xSe_{1-x} nanoribbon and CdS_xSe_{1-x} NB based FET, respectively. Under illumination, overall performance of ternary and metal-doped binary and ternary alloy improved due to e-h pair generation that increases the overall device conductivity. Therefore, the integrated circuit with binary and ternary II-VI alloy experimentally performed but high density and without compromising individual structure performance is still a challenge that need to be address at low cost technology device fabrication. Because the high-density integration at nanoscale for multiple nanostructure involve complicated fabrication steps that not only costly but also manipulate the performance of individual nanostructure [377,384].

(c)

(Unit 10⁴)

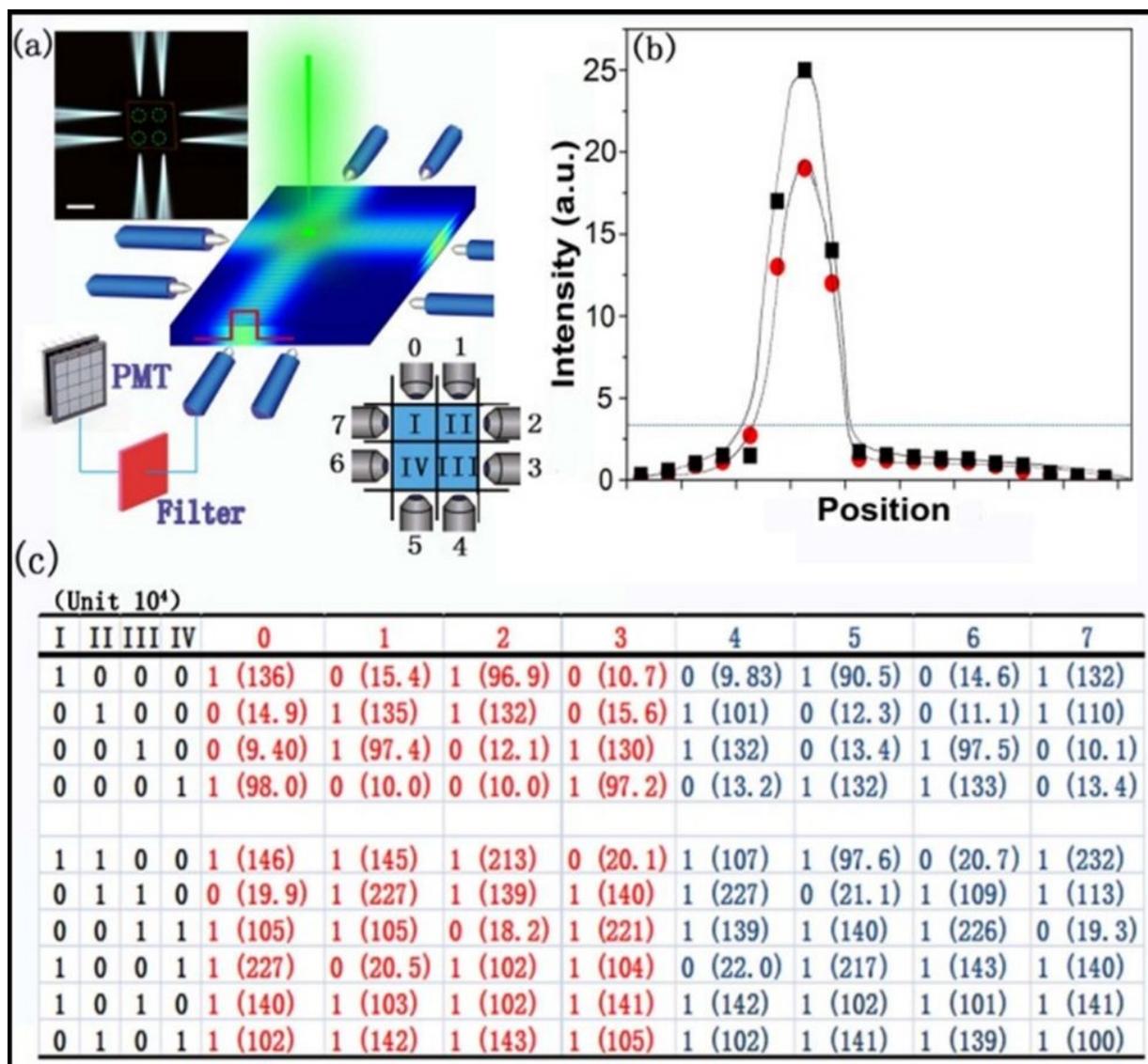| I	II	III	IV	0	1	2	3	4	5	6	7
1	0	0	0	1 (136)	0 (15.4)	1 (96.9)	0 (10.7)	0 (9.83)	1 (90.5)	0 (14.6)	1 (132)
0	1	0	0	0 (14.9)	1 (135)	1 (132)	0 (15.6)	1 (101)	0 (12.3)	0 (11.1)	1 (110)
0	0	1	0	0 (9.40)	1 (97.4)	0 (12.1)	1 (130)	1 (132)	0 (13.4)	1 (97.5)	0 (10.1)
0	0	0	1	1 (98.0)	0 (10.0)	0 (10.0)	1 (97.2)	0 (13.2)	1 (132)	1 (133)	0 (13.4)
1	1	0	0	1 (146)	1 (145)	1 (213)	0 (20.1)	1 (107)	1 (97.6)	0 (20.7)	1 (232)
0	1	1	0	0 (19.9)	1 (227)	1 (139)	1 (140)	1 (227)	0 (21.1)	1 (109)	1 (113)
0	0	1	1	1 (105)	1 (105)	0 (18.2)	1 (221)	1 (139)	1 (140)	1 (226)	0 (19.3)
1	0	0	1	1 (227)	0 (20.5)	1 (102)	1 (104)	0 (22.0)	1 (217)	1 (143)	1 (140)
1	0	1	0	1 (140)	1 (103)	1 (102)	1 (141)	1 (142)	1 (102)	1 (101)	1 (141)
0	1	0	1	1 (102)	1 (142)	1 (143)	1 (105)	1 (102)	1 (141)	1 (139)	1 (100)

Figure 19: (a) Schematic diagram of a real-intensity measurement system with the fiber tips together with a photomultiplier tube as detector units based on a square nanoplate (dark blue). Upper inset: the real dark-field image of a square nanoplate with size 25 × 25 μm. The fiber tips with diameter 250 nm were arranged around the nanoplate. Scale bar is 10 μm. Lower right inset: simple schematic diagram from the top view of whole microsystem. (b) Lighting position-dependent intensity change along the top edge (Black Square) and right side edge (red circle) clockwise, respectively. The x-axis represents the scanning position. The line corresponds to threshold-intensity level. (c) Detailed state of each fiber together with excitation position. The first four columns represent different excitation position, (1000) for region I, (0100) for region II, and so on. The columns with number from 0 to 7 represent actual emitting-out states at eight different

edge positions corresponding to the different excitation regions. In each table unit, the real emission intensity is given in brackets, Copyright © 2017 IOP Publishing [383].

4.2.2 Sensing in Bio-medical application

Lieber and co-worker extensively reported nanoscale transistor work as nano-bioelectronics that combine interdisciplinary field of biology and nanoscale electronics to address and overcome the existing challenges in bioelectronics [14,18,28]. Nanoscale device exhibits more sensitivity and biocompatibility that open new horizon for fundamental biology and healthcare. Device as the size of molecules reveals various advantages such as high surface to volume ratio, real-time sensitive detection of protein and others is owing to high performance FETs. The surface of a nano-FET is functionalized with biomolecule receptors that can selectively bind to biomolecule targets. By applying electric potential at gate, nano-FET charge through biomolecules and thus the charge carrier density tuned and leads to an electrical conductivity change associated with bio-molecular binding events in real time. Same diameter of both acceptor and receiver provide more sensitivity detection that can be further improved with array of NWs for multiplex detection in the same way. Such method is quite effective for detection and recognition of various chemical and biological systems [40,51,385].

FET Sensor: Same like planar FETs, nanoFET can be controlled by applying electric potential to control the conduction in the channel that make nano-FETs ideal candidates for chemical and biological sensing [374]. For example, p-type Si NW, the receptors (chemical/bio-molecule) binding of molecules with negative charges leads the formation of accumulation layer in the channel increase in conductance. However, binding of molecules with positive charges will deplete holes in the active layer will reduce the conductance. Thus, the NW FETs allow real-time directional electrical give information of biological events related to binding/unbinding, enzymatic reactions, and electron transfer, capabilities that are ultimate for emerging platform to investigate biological samples. SiO_2 layer on Si NW surface is nontoxic and can sense the hydrogen detection in lipid bilayers with and without ligand-gated, amino groups and silanol groups (Si−OH). Silicon NW are extensively used is owing to mature material in comparison with other II-VI materials and widely used for bio-molecular sensing. However, the ZnO NW also has been used for the development of FET biosensors [351,386].

Protein Sensor: The sensitive detection of proteins related with disease markers and offers substantial potential to diagnosis and treatment, first demonstrated real-time protein sensing in 2001. Nano FETs has capability to sense biotin receptors, detect streptavidin (concentrations down to 10 pM), biotin-monoclonal antibiotin binding and calmodulin in real time. More recent study, basic approach has been used to demonstrate successful concentration-dependent detection of cardiac troponin T390, SARS virus nucleocapsid proteins, and bovine serum albumin along with genomics and proteomics for diagnosing complex diseases such as cancers. Moreover, the availability of altered biomarkers matched with different phases of diseases could help for initial detection and robust diagnosis [18,28,387].

Nucleic acid Detection: A major difference between nucleic acid and protein detection is the high density of negative charges on the nucleic acid phosphate strengths high ionic strength barriers to screen the repulsion in the active channel region and to allow for binding; when DNA or RNA is used as the probe molecule. However, high ionic strength solutions have short Debye screening which can make detection difficult. Therefore, the solution that have high ionic strength binding/screening involves using neutral charge peptide nucleic acids (PNAs), which exhibit excellent binding affinity with DNA at lower ionic strengths. Si NWs with PNA probe molecules exhibit time-dependent conductance changes is associated with selective binding of complementary target DNA at low concentrations (10 fM). In addition to sensing protein binding/unbinding, real−time detection of nucleic acids (e.g., DNAs and RNAs) has been successfully carried out by Si and GaN NW FET devices [387,388]. Multisegment CdTe−Au− CdTe NW are used in devices in which Au segments are modified with thiol-terminated DNA probes and binding to these probes induces a conductance change in the overall device structure [389,390].

Virus Detection: Viruses are the main origin of infectious diseases, which continue the world's foremost cause of death. Successful treatment of viral diseases often depends upon quick and precise identification of viruses at ultralow concentrations in living organism. Si NW based first nanoFET-based successfully detect the virus influenza A. By recording the analogous electrical conductance fluctuations upon binding/unbinding of virus particles to monoclonal-antibody-modified Si NWs, the selective detection of influenza A at the single-particle level has demonstrated sucessfully. Another example of virus detection is the identification of dengue. Specific nucleic acid fragment with 69 base pairs derived from dengus serotype 2 virus genome

sequence was selected as the target DNA and amplified by the reverse transcription polymerase chain reaction (RT-PCR). The hybridization of the target DNA and PNA functionalized Si NW FET sensors increases the device resistance, leading to a sensitivity limit down to 10 fM [18,29,389,391].

4.3 Spintronic

Spintronics based devices open chapter in electronic device scale down on single chip to follow the Moore's law that controlled by spin degree of freedom of charge carriers. Realization of such devices in 1925 become true after continue optimization the nature of TM ion in various semiconductors. Still there is room of improvement to explore its fascinating functionality for various electronics application especially for 1D systems. Unique optical response of low dimensional and spin controlled behavior open new horizon in spintronics device based on spin dependent electronic properties of FM behavior [392]. TM ion incorporation in II-VI semiconductors exhibits the spin splitting of conduction and valance band through exchange coupling of sp-d between delocalized carriers and core spin. Wide bandgap semiconductor such as GaN, ZnO and others also exhibits the spin-carrier interaction above room temperature. Ternary alloy formation or heterojunction devices can be frequently used for spin dependent transport across the interface between different materials. Mn ions introduce spins and holes to the valance band in GaAs, point defect in in SnTe, MnTe, etc. and shallow acceptor impurities in CdMnTe, ZnMnTe at which the polarized electrons permits injection of spins to normal semiconductors. FM order of spin ion is mediated by carriers in Mn based DMS in II-VI semiconductor. Spin-spin interaction become dominant by divalent of Mn ion through hybridization between anion and d-states of TM ion. Super-exchange of divalent TM ion may lead the formation of AFM coupling [393,394]. Spin-carrier interaction for n-type and p-type semiconductor related with spin-polarized electrons or holes in DMS. Spin polarization of injected carriers can be detectable by optically circular polarized also known as spin LED. However, as the spin relaxation time for the holes is much shorter than that for the electrons for QW based spin-LED. Moreover, the neuromorphic computing uses brain-inspired principles to design circuits perform computational tasks with superior power efficiency based on spintronics nano-devices at which electronic devices to create artificial neurons and synapses with efficient energy integrated circuits. Spintronics based neuromorphic computing can effectively recognition pattern in an associative memory [395].

At low temperature (5k), CdTe/ZnTe QDs doped with Cr ion shows spin relaxation under strong resonant field that can tuned the Cr ion due to stark effect. The exchange interaction between spin atom and exciton further split the Cr energy level due to high polarizability of crystal field. For carrier dynamics, understanding with transient absorption spectroscopy to observe the relaxation time and non-equilibrium distribution of Cr spin population with circularly polarized luminescence spectra. Cr ion interaction with phonon within the system show strong spin-phonon coupling at 5k, which is an important step forward to control the TM ion coherent spin for future spintronic device. Similarly, Cr spin is coupled with exciton near valance band and show the Nano-magnetic behavior due to optical pumping of electron-Cr and hole-Cr. Resonance and non-resonance optical pumping can directly use as the spin memory (write and erase). Therefore, the spin channel can be studied with polarized emission that respond to relaxation channel of Cr ion in II-VI semiconductors. Therefore, optical pumping and power dependent PL intensity related temperature effect is directly affected the hole-Cr spin near valance band and electron-Cr local generation of phonons [158].

4.4 Future Research Direction

In this Review, we will focus on low-dimensional II-VI semiconductors Nanostructure optical properties for potential application over past two decade that gain numerous attention at nanoscale active and passive devices in optoelectronics, bioelectronics and electrochemical applications. The interdisciplinary nature of the research offered here signifies the future of scientific discovery, where the boundaries between chemistry, physics, biology, and engineering are no longer relevant. We tried to cover the intensive researches on 1D II-VI semiconductor binary, ternary alloy and TM doping and understand its luminescence properties related with excitons, photons and phonons within nanostructures and their coupling with quanta such as photons and plasmons. The light-matter interaction provides fascinating information and tunable optical emission from molar ratio and ferromagnetic semiconductors, which usually arises from carrier-spin interaction, spin-spin coupling and sp-d hybridization between anions. Therefore, the realization of chemistry and physics of nanostructure is reasonably supportive to control the growth pattern, crystal structure and compositional complexity for practical applications of materials toward novel technologies. Luminescence behavior shows magnetic ion's dynamic nature through spin-splitting, bandgap narrowing and magnetic polaron. Transition metal ion doping in II-VI semiconductors exhibits the phonon-spin, spin-spin and exciton-spin interaction that show EMP, BMP or LEMP and exciton

antiferromagnetic polarons in 1D and 2D systems. The pulse laser produces the bosonic lasing owing to coherent magnetic exciton Bose-Einstein condensation in a low doping profile, which favors the ferromagnetic coupling. Moreover, the high doping profile scatter coherent EMP due to bound exciton, coexisting EMPs and e-h plasma formation at the surface of nanostructure. The coupled optical microcavity effect produces enhanced photonic Bloch oscillation in 1D nanostructures with multipeak emission or lasing at low threshold pumping depending on the spatial distribution of photon corresponding to exciton-polariton formation. The importance of nanostructures such as axial, radical/coaxial modulated, branched and kink are subsequent generation building blocks for bioelectronics, photonics and electronics circuits. Increasing number of device on single chip without compromising its properties is important to understand semiconductor/metal/insulator interfacial or hybrid structure with organic semiconductors or 2D materials that could lead to enhance the device performance with improved responsivity, detectivity and quantum efficiency. Therefore, the different advanced synthesis techniques implied to control the size, morphology and composition of II-VI semiconductor nanostructure to ensure reproducibility, yield high quality and cost effective materials suitable for large-scale device fabrication. Spin behavior in II-VI semiconductor open new horizon for DMS research direction for flexible electronics, wearable devices, and bio-sensing platforms, leveraging their unique optical and electronic properties. Yang, Leiber and other research groups focused on 1D nanostructures analogous to biomedical application such as biochemical sensors, extracellular and intracellular electrical sensor, molecules delivery, injectable electronics, biosynthesis and optical neuromodulation.

5. Outlook

In this review, we have provided an overview of TM ion doping in II-VI semiconductors, their fundamentals properties especially its exceptional optical properties and the promising optoelectronic applications. Moreover, we have highlighted the rapid and prominent development in research activities within last two decades that conscious about increasingly importance of 1D nanostructure in current technology market. Recent advances in 1D nanostructures such as NW, NB and others open up opportunities for future generation nanodevice applications. The interdisciplinary nature of the research offered here signifies the future of scientific discovery, where the boundaries between chemistry, physics, biology, and engineering are no longer relevant.

In this review, we focus on 1D nanostructures luminescence comportment based on binary and ternary alloy of II-VI semiconductors and their composition gradient, along with the TM ion doping in 1D II-VI nanostructures. Based on these following, we highlighted some important issues for promoting the practical applications of II-VI nanostructures:

1-   In the past decade, researchers have attained substantial progresses in the synthesis and characterization of II-VI nanostructures in the forms of NW/NT/NB that have been grown by both physical and chemical methods. The properties of nanostructures are strongly determined by their geometries, stoichiometric ratio, structures, and surface states. Chemical synthesis for NPs, QDs and others exhibits unique electronic and optical properties due to quantum size effect is owing to nanoscale at low cost and less energy consumption but compromising the crystal quality and surface effect. Physical synthesis such as VLS mechanism for 1D has offered highly crystalline and controlled nanostructure with composition, orientation and reproducibility still challenging at high temperature. 1D nanostructures of II-VI ternary alloys have inspired by the rapid development of technology during the last decade; research progress regarding the material synthesis, fundamentals of optical properties, and promising electronic for optoelectronic and photonic applications. Although most of the ternary alloy nanostructures and their corresponding applications are new and infancy of technological development but still the research on ternary alloy is highly attractive and rewarding. Recently, many researchers have realized the advantages of quaternary alloys, blended organic-inorganic hybrid devices and TM ion incorporation to fulfil the future device applications demand.

2-   TM ion doping in 1D nanostructure exhibits unique optical properties and promotes various electronic and photonic applications. Incorporation of TM ion exhibits spin-carrier injection, spin-spin coupling among TM ion and p-d hybridization (involving p-orbital anions and d-orbital of TM ions) which make II-VI semiconductors suitable for DMS. Exciton magnetic polarons and Bound magnetic polarons or Localized EMPs are outstanding zones for DMS that need an enormous ground of study to explore for Zn chalcogenides and Cd chalcogenides for 1D system.

a) TM ion doping in 1D II-VI semiconductors is suitable candidate for DMS related applications. TM ion concentration can tune the luminescence spectra under different laser excitation power. Low TM concentration may lead to the interaction between spin ion with free exciton and phonon to form independent EMPs. Even low TM doping can tune

bandgap and related d-d transition in the emission spectra at room temperature. Low TM concentration with high laser excitation can show the bosonic lasing apparent owing to coherent collective EMP transition from magnetic exciton Bose-Einstein condensation at room temperature. LO phonon and spins ion interaction exhibits the bosonic lasing reported in 1D nanostructures that appears for long range coherent coupling of local EMPs. Moreover, the high TM ion doping scatter the coherent EMP due to (i) bound carriers (ii) coexisting EMPs and (iii) e-h plasma formation at the surface of nanostructures.

b) For low dimensional system, the free exciton or polaronic exciton or bound exciton will be prominent with TM ion doping in II-VI semiconductor at room temperature. Moreover, the doping profile will enhance the electron-phonon interaction especially for 1D NWs. For ZnO:Mn, the polaronic exciton bind with free exciton for large excitonic binding energy material to show bipolaronic exciton condensate under fs laser excitation. For coherent and high power favors the multimode lasing emission at room temperature. Moreover, the LO phonon in c-axis contribute the condensate formation for BEC of exciton at room temperature.

c) Optical characterization tools has capability to observe the dynamic nature of magnetic ions that can provide strong evidence of spin splitting, bandgap narrowing and bound magnetic polarons in nanostructure. Strong spin-spin interaction demonstrate additional broadening of bandwidth or strong inhomogeneous broadening that is standard electron paramagnetic resonance of spin ions in DMS. Raman scattering provides suitable information about the bound magnetic polarons at low temperature that show the strength of antiferromagnetic interaction between nearest neighbor d-d interaction. Time-resolved spectroscopy provide dynamic of local spin ordering reveals with either bound magnetic polaron or self-trapped related with exciton magnetic polaron.

d) A detailed comprehension and deeper understanding of material properties and device behavior is required to find significance of performance reliability and revolutionary applications from the novel and innovative fundamental properties manifested at the nanoscale. In particular, more demanding for 1D nanostructure research should be devoted to gaining deeper and comprehension understanding of the interaction properties of excitons, plasmons and phonons within the II–VI semiconductors. Therefore, we can explore their coupling mechanism with other quanta that has been influenced by its optical

properties and related applications that is greatly influenced by the interactions and coupling strongly on optical and emissive properties of II-VI materials.

e) Additionally, the development of 1D II–VI nanostructures with CVD is important for various photonic applications. Doping in 1D structures can afford active photonic waveguide to tune its emission and propagation light wavelength with propagation distance, and issuing at the wire end with tunable wavelength. The tunability come from the strong exciton-phonon coupling during the light propagation. Such as Sn:CdS, CdSSe NWs array and branched like structure for 1D periodic photonic application related with exciton-polariton. Coupled optical microcavity effect produce enhanced photonic Bloch oscillation in such wire and multipeak emission or lasing at low threshold pumping. Photonic propagation within the wire show clear spatial dependent photon distribution and correlation.

3-   1D nanostructures of II-VI ternary alloys have inspired by the rapid development of technology during the last decade; research progress regarding the material synthesis, fundamentals of optical properties, and promising electronic for optoelectronic and photonic applications. Although most of the ternary alloy nanostructures and their corresponding applications are new and infancy of technological development but still the research on ternary alloy is highly attractive and rewarding. As an important foundation is developing efficient and low-cost technology for ternary II–VI 1D nanostructures synthesized with high quality and large quantities. Therefore, it is necessary to adopt effective preparation techniques that is more controllable with simultaneous precision of composition, orientation, location, alignment and dimension. Therefore, physical properties of nanostructures are more suitable for massive-scale device integration for single structure. To achieve the following task, ternary and quaternary or polycompounds are designed and synthesized to enable a full spectrum response. Recently, many researchers have realized the advantages of quaternary alloys. Additionally, the development of ternary II–VI 1D nanostructures is also important for tunable bandgap applicable in electronic and optoelectronic circuits. High Surface-sensitive is owning to large surface to volume ratio in 1D system make it appropriate for high-sensitivity gas, chemical and biological detectors. 1D hybrid nanostructures are highly appropriately in various optoelectronic applications such as Type-I or Type-II junctions; Type-I junction exhibits high fluorescence and light emitter yield (LED and Laser), while Type-II junction facilitate the formation of e–h pairs with improved energy

conversion efficiency (photodetector and solar cell). Different prototypes have capability to assemble and integrate individual structure into functional devices on a large scale. To achieve high-density large-scale integrated devices at low cost is still a bottleneck.

4- Another important emerging phenomenon in 1D II-VI material research is the essential for large-scale architectures engineered at low cost without compromising the material properties at the nanoscale rather than focus on individual structure. For commercial adaptation of 1D system, the devices design development must be emphasis at low cost, environment friendly and minimum waste in utilization of more expensive elements along with the necessary spatial and temporal resolution to implement quality control throughout fabrication processes. Such control will facilitate the development of next era nanotechnology in the field of environment, biomedical, and economic benefits to society and realized on a global scale. Lieber group synthesized the IV, III-V and II-VI 1D nanostructures analogous to biological systems and biomedical application, along with detailed understanding of individual nanostructure and its interfacial interactions for biochemical sensors, extracellular and intracellular electrical sensor, molecules delivery, injectable electronics, biosynthesis and optical neuromodulation for brain science.

6. Conclusion & Future Prospective

In this review, we discuss the magnetic polaron and their interaction with exciton, electron and spin ion for TM ion doped in various II-VI semiconductors for 1D DMS nanostructures. Moreover, we explore the formation of EMP, BMP and LEMP related dynamics spectral response along with collective response such as bipolaronic BEC exciton at room temperature. Strong electron-phonon interaction materials coupled with spin ion to show the stable EMP formation. High excitation with low concentration of magnetic ion may lead the formation of bosonic lasing due to collective EMPs that has interesting application for future spin related optical device at room temperature. The active photonic waveguide property come from strong electron-phonon coupling during light propagation. Coupled optical microcavity effect produce enhanced photonic Bloch oscillation in such wire and multipeak emission or lasing at low threshold pumping. TM ion doping in II-VI ternary alloy nanostructures are still in the infancy of technological development. In particular, we believe that more comprehend and intensive research studies must be devoted to gain deep and better understanding of luminescence properties related with of excitons and phonons within the II–VI 1D nanostructures and their coupling with quanta such as photons and plasmons. Better and

deeper understanding of luminescence properties of binary, ternary alloy, heterojunctions and architectures along with metal ion doping of II–VI 1D nanostructures need to realization for overall optical and emissive properties for emergence of revolutionary applications from the novel fundamental properties. Each of these applications of 1D II-VI nanostructures has been developed based on years of research and fundamental understanding of entire materials related chemistry, physics, and engineering to practical implementation.

AUTHOR DECLARATIONS

Conflict of Interest

The authors have no conflict of interests to disclose.

DATA AVAILABILITY: The data that supports the findings of this study are available within the review article.

Materials Advances Accepted Manuscript

References

(1)   Khan, M. S.; Zou, B.; Shi, L. J.; Yao, S.; Bukhtiar, A.; Huang, W. G.; Lu, Y.; Cao, J. J.;
Zheng, B. Carrier-Mediated Ferromagnetism in Mn(II)-Doped ZnTe Thin Films and Their
Optical Properties: A First-Principles Study. *J. Alloys Compd.* **2023**, *964*, 171316.
https://doi.org/10.1016/j.jallcom.2023.171316.

(2)   Sheraz Khan, M.; Zou, B.; Yao, S.; Bukhtiar, A.; Huang, W. G.; Zhou, Z. Computational
Study of Electronic, Magnetic, and Optical Properties of Fe(II) Mono-Doped and (Fe(II),
Al) Co-Doped ZnTe. *J. Magn. Magn. Mater.* **2023**, *567*, 170344.
https://doi.org/10.1016/j.jmmm.2022.170344.

(3)   Zou, S.; Kamran, M. A.; Shi, L. J.; Liu, R.; Guo, S.; Kavokin, A.; Zou, B. Bosonic Lasing
from Collective Exciton Magnetic Polarons in Diluted Magnetic Nanowires and
Nanobelts. *ACS Photonics* **2016**, *3* (10), 1809–1817.
https://doi.org/10.1021/acsphotonics.6b00289.

(4)   Liu, R.; Shi, L.; Zou, B. Magnetic Exciton Relaxation and Spin-Spin Interaction by the
Time-Delayed Photoluminescence Spectra of ZnO:Mn Nanowires. *ACS Appl. Mater.
Interfaces* **2014**, *6* (13), 10353–10366. https://doi.org/10.1021/am501835j.

(5)   Zou, B.; Tian, Y.; Shi, L.; Liu, R.; Zhang, Y.; Zhong, H. Excitonic Magnetic Polarons in
II-VI Diluted Magnetic Semiconductor Nanostructures. *J. Lumin.* **2022**, *252*, 119334.
https://doi.org/10.1016/j.jlumin.2022.119334.

(6)   Ferrand, D.; Wasiela, A.; Tatarenko, S.; Cibert, J.; Richter, G.; Grabs, P.; Schmidt, G.;
Molenkamp, L. W.; Dietl, T. Applications of II-VI Diluted Magnetic Semiconductors for
Magneto-Electronics. *Solid State Commun.* **2001**, *119*, 237–244.
https://doi.org/10.1016/S0038-1098(01)00174-0.

(7)   Dietl, T.; Ohno, H. Dilute Ferromagnetic Semiconductors: Physics and Spintronic
Structures. *Rev. Mod. Phys.* **2014**, *86* (1), 187–251.
https://doi.org/10.1103/RevModPhys.86.187.

(8)   Wolf, S. A.; Awschalom, D. D.; Buhrman, R. A.; Daughton, J. M.; Von Molnár, S.;

Roukes, M. L.; Chtchelkanova, A. Y.; Treger, D. M. Spintronics: A Spin-Based Electronics Vision for the Future. *Science (80-.).* **2001**, *294* (5546), 1488–1495. https://doi.org/10.1126/science.1065389.

(9)   Lu, J.; Liu, H.; Zhang, X.; Sow, C. H. One-Dimensional Nanostructures of II-VI Ternary Alloys: Synthesis, Optical Properties, and Applications. *Nanoscale* **2018**, *10*, 17456–17476. https://doi.org/10.1039/c8nr05019h.

(10)   Utama, M. I. B.; Zhang, J.; Chen, R.; Xu, X.; Li, D.; Sun, H.; Xiong, Q. Synthesis and Optical Properties of II-VI 1D Nanostructures. *Nanoscale* **2012**, *4*, 1422–1435. https://doi.org/10.1039/c1nr11612f.

(11)   Jie, J.; Zhang, W.; Bello, I.; Lee, C. S.; Lee, S. T. One-Dimensional II-VI Nanostructures: Synthesis, Properties and Optoelectronic Applications. *Nano Today* **2010**, *5*, 313–336. https://doi.org/10.1016/j.nantod.2010.06.009.

(12)   Zhang, Q.; Li, H.; Ma, Y.; Zhai, T. ZnSe Nanostructures: Synthesis, Properties and Applications. *Prog. Mater. Sci.* **2016**, *83*, 472–535. https://doi.org/10.1016/j.pmatsci.2016.07.005.

(13)   Lieber, C. M. One-Dimensional Nanostructures: Chemistry, Physics & Applications. *Solid State Commun.* **1998**, *107* (11), 607–616. https://doi.org/10.1016/S0038-1098(98)00209-9.

(14)   Tian, B.; Lieber, C. M. Nanowired Bioelectric Interfaces. *Chem. Rev.* **2019**, *119* (15), 9136–9152. https://doi.org/10.1021/acs.chemrev.8b00795.

(15)   Xia, B. Y.; Yang, P.; Sun, Y.; Wu, Y.; Mayers, B.; Gates, B.; Yin, Y.; Kim, F.; Yan, H. One-Dimensional Nanostructures : Synthesis , Characterization , and Applications. *Adv. Mater.* **2003**, *15* (5), 353–389. https://doi.org/https://doi.org/10.1002/adma.200390087.

(16)   Quan, L. N.; Kang, J.; Ning, C. Z.; Yang, P. Nanowires for Photonics. *Chem. Rev.* **2019**, *119* (15), 9153–9169. https://doi.org/10.1021/acs.chemrev.9b00240.

(17)   Ning, C. Z.; Dou, L.; Yang, P. Bandgap Engineering in Semiconductor Alloy Nanomaterials with Widely Tunable Compositions. *Nat. Rev. Mater.* **2017**, *2*, 1–15. https://doi.org/10.1038/natrevmats.2017.70.

Materials Advances Accepted Manuscript

(18)   Zhang, A.; Lieber, C. M. Nano-Bioelectronics. *Chem. Rev.* **2016**, *116* (1), 215–257. https://doi.org/10.1021/acs.chemrev.5b00608.

(19)   Kolasinski, K. W. Catalytic Growth of Nanowires: Vapor-Liquid-Solid, Vapor-Solid-Solid, Solution-Liquid-Solid and Solid-Liquid-Solid Growth. *Curr. Opin. Solid State Mater. Sci.* **2006**, *10* (3–4), 182–191. https://doi.org/10.1016/j.cossms.2007.03.002.

(20)   Hou, L.; Zhou, W.; Zou, B.; Zhang, Y.; Han, J.; Yang, X.; Gong, Z.; Li, J.; Xie, S.; Shi, L. J. Spin-Exciton Interaction and Related Micro-Photoluminescence Spectra of ZnSe:Mn DMS Nanoribbon. *Nanotechnology* **2017**, *28* (10), 105202. https://doi.org/10.1088/1361-6528/aa58f1.

(21)   Chen, D.; Wang, A.; Buntine, M. A.; Jia, G. Recent Advances in Zinc-Containing Colloidal Semiconductor Nanocrystals for Optoelectronic and Energy Conversion Applications. *ChemElectroChem* **2019**, *6* (18), 4709–4724. https://doi.org/10.1002/celc.201900838.

(22)   Zhang, L. De; Fang, X. S. Controlled Growth and Characterization Methods of Semiconductor Nanomaterials. *J. Nanosci. Nanotechnol.* **2008**, *8* (1), 149–201. https://doi.org/10.1166/jnn.2008.N02.

(23)   Zhai, T.; Fang, X.; Li, L.; Bando, Y.; Golberg, D. One-Dimensional CdS Nanostructures: Synthesis, Properties, and Applications. *Nanoscale* **2010**, *2* (2), 168–187. https://doi.org/10.1039/b9nr00415g.

(24)   Lu, W.; Lieber, C. M. Semiconductor Nanowires. *J. Phys. D. Appl. Phys.* **2006**, *39*, R387–R406. https://doi.org/10.1088/0022-3727/39/21/R01.

(25)   Jang, E.; Jang, H. Review: Quantum Dot Light-Emitting Diodes. *Chem. Rev.* **2023**, *123* (8), 4663–4692. https://doi.org/10.1021/acs.chemrev.2c00695.

(26)   Zhao, Y.; Yao, J.; Xu, L.; Mankin, M. N.; Zhu, Y.; Wu, H.; Mai, L.; Zhang, Q.; Lieber, C. M. Shape-Controlled Deterministic Assembly of Nanowires. *Nano Lett.* **2016**, *16* (4), 2644–2650. https://doi.org/10.1021/acs.nanolett.6b00292.

(27)   Viveros, R. D.; Zhou, T.; Hong, G.; Fu, T. M.; Lin, H. Y. G.; Lieber, C. M. Advanced One- and Two-Dimensional Mesh Designs for Injectable Electronics. *Nano Lett.* **2019**, *19*

(6), 4180–4187. https://doi.org/10.1021/acs.nanolett.9b01727.

(28)   Duan, X.; Lieber, C. M. Nanoscience and the Nano-Bioelectronics Frontier. *Nano Res.*
       2015, *8* (1), 1–22. https://doi.org/10.1007/s12274-014-0692-8.

(29)   Zhou, W.; Dai, X.; Lieber, C. M. Advances in Nanowire Bioelectronics. *Reports Prog.*
       Phys. **2017**, *80*, 016701. https://doi.org/10.1088/0034-4885/80/1/016701.

(30)   Dai, X.; Hong, G.; Gao, T.; Lieber, C. M. Mesh Nanoelectronics: Seamless Integration of
       Electronics with Tissues. *Acc. Chem. Res.* **2018**, *51* (2), 309–318.
       https://doi.org/10.1021/acs.accounts.7b00547.

(31)   Xia, Y.; Yang, P. Chemistry and Physics of Nanowires. *Adv. Mater.* **2003**, *15* (5), 351–
       352. https://doi.org/10.1002/adma.200390086.

(32)   Law, M.; Goldberger, J.; Yang, P. Semiconductor Nanowires and Nanotubes. *Annu. Rev.*
       Mater. Res. **2004**, *34* (2), 83–122.
       https://doi.org/10.1146/annurev.matsci.34.040203.112300.

(33)   Duan, X.; Lieber, C. M. General Synthesis of Compound Semiconductor Nanowires. *Adv.*
       Mater. **2000**, *12* (4), 298–302. https://doi.org/10.1002/(SICI)1521-
       4095(200002)12:4<298::AID-ADMA298>3.0.CO;2-Y.

(34)   Sonkar, R.; Mondal, N. J.; Thakur, S.; Saikia, E.; Ghosh, M. P.; Chowdhury, D. Cobalt-
       Substituted ZnS QDs: A Diluted Magnetic Semiconductor and Efficient Photocatalyst.
       Nanoscale Adv. **2023**, *5* (24), 7042–7056. https://doi.org/10.1039/d3na00836c.

(35)   Shim, H. S.; Ko, M.; Nam, S.; Oh, J. H.; Jeong, S.; Yang, Y.; Park, S. M.; Do, Y. R.;
       Song, J. K. InP/ZnSeS/ZnS Quantum Dots with High Quantum Yield and Color Purity for
       Display Devices. *ACS Appl. Nano Mater.* **2023**, *6* (2), 1285–1294.
       https://doi.org/10.1021/acsanm.2c04936.

(36)   Wagner, R. S.; Ellis, W. C. Vapor-Liquid-Solid Mechanism of Single Crystal Growth.
       Appl. Phys. Lett. **1964**, *4* (5), 89–90. https://doi.org/10.1063/1.1753975.

(37)   Kim, B. J.; Tersoff, J.; Wen, C. Y.; Reuter, M. C.; Stach, E. A.; Ross, F. M. Determination
       of Size Effects during the Phase Transition of a Nanoscale Au-Si Eutectic. *Phys. Rev. Lett.*

Materials Advances Accepted Manuscript

2009, *103*, 155701. https://doi.org/10.1103/PhysRevLett.103.155701.

(38) Kim, B. J.; Tersoff, J.; Kodambaka, S.; Reuter, M. C.; Stach, E. A.; Ross, F. M. Kinetics of Individual Nucleation Events Observed in Nanoscale Vapor-Liquid-Solid Growth. *Science (80-.).* **2008**, *322* (5904), 1070–1073. https://doi.org/10.1126/science.1163494.

(39) Deng, J.; Su, Y.; Liu, D.; Yang, P.; Liu, B.; Liu, C. Nanowire Photoelectrochemistry. *Chem. Rev.* **2019**, *119* (15), 9221–9259. https://doi.org/10.1021/acs.chemrev.9b00232.

(40) Lieber, C. M. Semiconductor Nanowires: A Platform for Nanoscience and Nanotechnology. *MRS Bull.* **2011**, *36* (12), 1052–1063. https://doi.org/10.1557/mrs.2011.269.

(41) Avetissov, I. C.; Mozhevitina, E. N.; Khomyakov, A. V.; Avetisov, R. I.; Davydov, A. A.; Chegnov, V. P.; Chegnova, O. I.; Zhavoronkov, N. V. Homogeneity Limits and Nonstoichiometry of Vapor Grown ZnTe and CdTe Crystals. *CrystEngComm* **2015**, *17* (3), 561–568. https://doi.org/10.1039/c4ce00623b.

(42) Dubrovskii, V. G.; Sibirev, N. V.; Harmand, J. C.; Glas, F. Growth Kinetics and Crystal Structure of Semiconductor Nanowires. *Phys. Rev. B - Condens. Matter Mater. Phys.* **2008**, *78*, 235301. https://doi.org/10.1103/PhysRevB.78.235301.

(43) Wu, Y.; Yang, P. Direct Observation of Vapor-Liquid-Solid Nanowire Growth. *J. Am. Chem. Soc.* **2001**, *123* (13), 3165–3166. https://doi.org/10.1021/ja0059084.

(44) Kodambaka, S.; Tersoff, J.; Reuter, M. C.; Ross, F. M. Diameter-Independent Kinetics in the Vapor-Liquid-Solid Growth of Si Nanowires. *Phys. Rev. Lett.* **2006**, *96*, 096105. https://doi.org/10.1103/PhysRevLett.96.096105.

(45) De La Mata, M.; Magen, C.; Gazquez, J.; Utama, M. I. B.; Heiss, M.; Lopatin, S.; Furtmayr, F.; Fernández-Rojas, C. J.; Peng, B.; Morante, J. R.; Rurali, R.; Eickhoff, M.; Fontcuberta I Morral, A.; Xiong, Q.; Arbiol, J. Polarity Assignment in ZnTe, GaAs, ZnO, and GaN-AlN Nanowires from Direct Dumbbell Analysis. *Nano Lett.* **2012**, *12* (5), 2579–2586. https://doi.org/10.1021/nl300840q.

(46) Utama, M. I. B.; De La Mata, M.; Magen, C.; Arbiol, J.; Xiong, Q. Twinning-, Polytypism-, and Polarity-Induced Morphological Modulation in Nonplanar

Nanostructures with van Der Waals Epitaxy. *Adv. Funct. Mater.* **2013**, *23* (13), 1636–1646. https://doi.org/10.1002/adfm.201202027.

(47)   Rueda-Fonseca, P.; Bellet-Amalric, E.; Vigliaturo, R.; Den Hertog, M.; Genuist, Y.; André, R.; Robin, E.; Artioli, A.; Stepanov, P.; Ferrand, D.; Kheng, K.; Tatarenko, S.; Cibert, J. Structure and Morphology in Diffusion-Driven Growth of Nanowires: The Case of ZnTe. *Nano Lett.* **2014**, *14* (4), 1877–1883. https://doi.org/10.1021/nl4046476.

(48)   Utama, M. I. B.; De La Mata, M.; Zhang, Q.; Magen, C.; Arbiol, J.; Xiong, Q. The Growth of Ultralong ZnTe Micro/Nanostructures: The Influence of Polarity and Twin Direction on the Morphogenesis of Nanobelts and Nanosheets. *Cryst. Growth Des.* **2013**, *13* (6), 2590–2596. https://doi.org/10.1021/cg4003498.

(49)   Dasgupta, N. P.; Sun, J.; Liu, C.; Brittman, S.; Andrews, S. C.; Lim, J.; Gao, H.; Yan, R.; Yang, P. 25th Anniversary Article: Semiconductor Nanowires - Synthesis, Characterization, and Applications. *Adv. Mater.* **2014**, *26* (14), 2137–2184. https://doi.org/10.1002/adma.201305929.

(50)   Kamran, M. A.; Majid, A.; Alharbi, T.; Iqbal, M. W.; Ismail, K.; Nabi, G.; Li, Z. A.; Zou, B. Novel Cd-CdS Micro/Nano Heterostructures: Synthesis and Luminescence Properties. *Opt. Mater. (Amst).* **2017**, *73*, 527–534. https://doi.org/10.1016/j.optmat.2017.09.005.

(51)   Chen, L.; Lu, W.; Lieber, C. M. *Semiconductor Nanowire Growth and Integration*; 2015; Vol. 11. https://doi.org/10.1039/9781782625209-00001.

(52)   Yeh, C. Y.; Lu, Z. W.; Froyen, S.; Zunger, A. Zinc-Blendewurtzite Polytypism in Semiconductors. *Phys. Rev. B* **1992**, *46* (16), 10086–10097. https://doi.org/10.1103/PhysRevB.46.10086.

(53)   Wang, F.; Yu, H.; Jeong, S.; Pietryga, J. M.; Hollingsworth, J. A.; Gibbons, P. C.; Buhro, W. E. The Scaling of the Effective Band Gaps in Indium-Arsenide Quantum Dots and Wires. *ACS Nano* **2008**, *2* (9), 1903–1913. https://doi.org/10.1021/nn800356z.

(54)   Sun, J.; Wang, L. W.; Buhro, W. E. Synthesis of Cadmium Telluride Quantum Wires and the Similarity of Their Effective Band Gaps to Those of Equidiameter Cadmium Telluride Quantum Dots. *J. Am. Chem. Soc.* **2008**, *130* (25), 7997–8005.

https://doi.org/10.1021/ja800837v.

(55) Tang, J.; Huo, Z.; Brittman, S.; Gao, H.; Yang, P. Solution-Processed Core-Shell Nanowires for Efficient Photovoltaic Cells. *Nat. Nanotechnol.* **2011**, *6* (9), 568–572. https://doi.org/10.1038/nnano.2011.139.

(56) Meir, I.; Horani, F.; Zuri, S.; Lifshitz, E. The Tuning of Exciton-Phonon Coupling in Colloidal Nanocrystals by a Dielectric Medium. *Adv. Opt. Mater.* **2022**, *10*, 2200230. https://doi.org/10.1002/adom.202200230.

(57) Zhao, H.; Hu, H.; Zheng, J.; Qie, Y.; Yu, K.; Zhu, Y.; Luo, Z.; Lin, L.; Yang, K.; Guo, T.; Li, F. One-Pot Synthesis of InP Multishell Quantum Dots for Narrow-Bandwidth Light-Emitting Devices. *ACS Appl. Nano Mater.* **2023**, *6* (5), 3797–3802. https://doi.org/10.1021/acsanm.2c05498.

(58) Yang, G.; Ma, Z.; Zhong, H.; Zou, S.; Chen, C.; Han, J.; Zou, B. Probing Exciton Move and Localization in Solution-Grown Colloidal CdSexS1-x Alloyed Nanowires by Temperature- and Time-Resolved Spectroscopy. *J. Phys. Chem. C* **2015**, *119* (39), 22709–22717. https://doi.org/10.1021/acs.jpcc.5b07198.

(59) Heo, Y. W.; Kang, B. S.; Tien, L. C.; Norton, D. P.; Ren, F.; LA Roche, J. R.; Pearton, S. J. UV Photoresponse of Single ZnO Nanowires. *Appl. Phys. A Mater. Sci. Process.* **2005**, *80* (3), 497–499. https://doi.org/10.1007/s00339-004-3045-8.

(60) Huang, M. H.; Mao, S.; Feick, H.; Yan, H.; Wu, Y.; Kind, H.; Weber, E.; Russo, R.; Yang, P. Room-Temperature Ultraviolet Nanowire Nanolasers. *Science (80-.).* **2001**, *292*, 1897–1899. https://doi.org/10.1126/science.1060367.

(61) Wu, Y.; Yan, H.; Yang, P. Semiconductor Nanowire Array : Potential Substrates for Photocatalysis and Photovoltaics. *Top. Catal.* **2002**, *19* (2), 197–202. https://doi.org/10.1023/A:1015260008046.

(62) Kempa, T. J.; Kim, S. K.; Day, R. W.; Park, H. G.; Nocera, D. G.; Lieber, C. M. Facet-Selective Growth on Nanowires Yields Multi-Component Nanostructures and Photonic Devices. *J. Am. Chem. Soc.* **2013**, *135* (49), 18354–18357. https://doi.org/10.1021/ja411050r.

(63)   Kempa, T. J.; Day, R. W.; Kim, S. K.; Park, H. G.; Lieber, C. M. Semiconductor Nanowires: A Platform for Exploring Limits and Concepts for Nano-Enabled Solar Cells. *Energy Environ. Sci.* **2013**, *6* (3), 719–733. https://doi.org/10.1039/c3ee24182c.

(64)   Kempa, T. J.; Cahoon, J. F.; Kim, S. K.; Day, R. W.; Bell, D. C.; Park, H. G.; Lieber, C. M. Coaxial Multishell Nanowires with High-Quality Electronic Interfaces and Tunable Optical Cavities for Ultrathin Photovoltaics. *PNAS* **2012**, *109* (5), 1407–1412. https://doi.org/10.1073/pnas.1120415109.

(65)   Gu, F.; Yang, Z.; Yu, H.; Xu, J.; Wang, P.; Tong, L.; Pan, A. Spatial Bandgap Engineering along Single Alloy Nanowires. *J. Am. Chem. Soc.* **2011**, *133* (7), 2037–2039. https://doi.org/10.1021/ja110092a.

(66)   Guo, P.; Zhuang, X.; Xu, J.; Zhang, Q.; Hu, W.; Zhu, X.; Wang, X.; Wan, Q.; He, P.; Zhou, H.; Pan, A. Low-Threshold Nanowire Laser Based on Composition-Symmetric Semiconductor Nanowires. *Nano Lett.* **2013**, *13* (3), 1251–1256. https://doi.org/10.1021/nl3047893.

(67)   Ertekin, E.; Greaney, P. A.; Chrzan, D. C.; Sands, T. D. Equilibrium Limits of Coherency in Strained Nanowire Heterostructures. *J. Appl. Phys.* **2005**, *97*, 114325. https://doi.org/10.1063/1.1903106.

(68)   Wang, D.; Qian, F.; Yang, C.; Zhong, Z.; Lieber, C. M. Rational Growth of Branched and Hyperbranched Nanowire Structures. *Nano Lett.* **2004**, *4* (5), 871–874. https://doi.org/10.1021/nl049728u.

(69)   Dai, G.; Gou, G.; Wu, Z.; Chen, Y.; Li, H.; Wan, Q.; Zou, B. Fabrication and Micro-Photoluminescence Property of CdSe/CdS Core/Shell Nanowires. *Appl. Phys. A Mater. Sci. Process.* **2015**, *119* (1), 343–349. https://doi.org/10.1007/s00339-014-8973-3.

(70)   Pan, A. L.; Lide, Y.; Qin, Y.; Yang, Y.; Kim, D. S.; Richeng, Y.; Bingsuo, Z.; Werner, P.; Zacharias, M.; Gösele, U. Si-CdSSe Core/Shell Nanowires with Continuously Tunable Light Emission. *Nano Lett.* **2008**, *8* (10), 3413–3417. https://doi.org/10.1021/nl802202e.

(71)   Dai, G.; Yang, S.; Yan, M.; Wan, Q.; Zhang, Q.; Pan, A.; Zou, B. Simple Synthesis and Growth Mechanism of Core/Shell CdSe/SiOx Nanowires. *J. Nanomater.* **2010**, *5*, 427689.

Materials Advances Accepted Manuscript

https://doi.org/10.1155/2010/427689.

(72) Xu, J.; Ma, L.; Guo, P.; Zhuang, X.; Zhu, X.; Hu, W.; Duan, X.; Pan, A. Room-Temperature Dual-Wavelength Lasing from Single-Nanoribbon Lateral Heterostructures. *J. Am. Chem. Soc.* **2012**, *134* (30), 12394–12397. https://doi.org/10.1021/ja3050458.

(73) Guo, P.; Hu, W.; Zhang, Q.; Zhuang, X.; Zhu, X.; Zhou, H.; Shan, Z.; Xu, J.; Pan, A. Semiconductor Alloy Nanoribbon Lateral Heterostructures for High-Performance Photodetectors. *Adv. Mater.* **2014**, *26* (18), 2844–2849. https://doi.org/10.1002/adma.201304967.

(74) Dong, A.; Wang, F.; Daulton, T. L.; Buhro, W. E. Solution-Liquid-Solid (SLS) Growth of ZnSe-ZnTe Quantum Wires Having Axial Heterojunctions. *Nano Lett.* **2007**, *7* (5), 1308–1313. https://doi.org/10.1021/nl070293v.

(75) Pan, A.; Wang, X.; He, P.; Zhang, Q.; Wan, Q.; Zacharias, M.; Zhu, X.; Zou, B. Color-Changeable Optical Transport through Se-Doped CdS 1D Nanostructures. *Nano Lett.* **2007**, *7* (10), 2970–2975. https://doi.org/10.1021/nl0710295.

(76) Zhang, Q.; Liu, H.; Guo, P.; Li, D.; Fan, P.; Zheng, W.; Zhu, X.; Jiang, Y.; Zhou, H.; Hu, W.; Zhuang, X.; Liu, H.; Duan, X.; Pan, A. Vapor Growth and Interfacial Carrier Dynamics of High-Quality CdS-CdSSe-CdS Axial Nanowire Heterostructures. *Nano Energy* **2017**, *32*, 28–35. https://doi.org/10.1016/j.nanoen.2016.12.014.

(77) Pan, A.; Liu, R. bin; Wang, F.; Xie, S.; Zou, B. suo; Zacharias, M.; Wang, Z. L. High-Quality Alloyed CdSxSe1-x Whiskers as Waveguides with Tunable Stimulated Emission. *J. Phys. Chem. B* **2006**, *110*, 22313–22317. https://doi.org/https://doi.org/10.1021/jp064664s.

(78) Xu, J.; Zhuang, X.; Guo, P.; Zhang, Q.; Huang, W.; Wan, Q.; Hu, W.; Wang, X.; Zhu, X.; Fan, C.; Yang, Z.; Tong, L.; Duan, X.; Pan, A. Wavelength-Converted/Selective Waveguiding Based on Composition-Graded Semiconductor Nanowires. *Nano Lett.* **2012**, *12* (9), 5003–5007. https://doi.org/10.1021/nl302693c.

(79) Sinova, J.; Jungwirth, T. Dilute Magnetic Semiconductors. In *Frontiers in Magnetic Materials*; 2005; pp 185–208. https://doi.org/10.1007/3-540-27284-4_7.

(80)   Wei, S. H.; Zunger, A. Total-Energy and Band-Structure Calculations for the
         Semimagnetic Cd1-XMnxTe Semiconductor Alloy and Its Binary Constituents. *Phys. Rev.
         B* **1987**, *35* (5), 2340–2365. https://doi.org/10.1103/PhysRevB.35.2340.

(81)   Dietl, T. Dilute Magnetic Semiconductors: Functional Ferromagnets. *Nat. Mater.* **2003**, *2*
         (10), 646–648. https://doi.org/10.1038/nmat989.

(82)   Ohno, H. Making Nonmagnetic Semiconductors Ferromagnetic. *Science (80-.)*. **1998**, *281*
         (5379), 951–956. https://doi.org/10.1126/science.281.5379.951.

(83)   Kobayashi, A.; Sankey, O. F.; Dow, J. D. Deep Energy Levels of Defects in the Wurtzite
         Semiconductors AIN, CdS, CdSe, ZnS, and ZnO. *Phys. Rev. B* **1983**, *28* (2), 946–956.
         https://doi.org/10.1103/PhysRevB.28.946.

(84)   Lipari, N. O. Exciton Energy Levels in Wurtzite-Type Crystals. *Phys. Rev. B* **1971**, *4* (12),
         4535–4538. https://doi.org/10.1103/PhysRevB.4.4535.

(85)   Mang, A.; Reimann, K.; Rübenacke, S. Band Gaps, Crystal-Field Splitting, Spin-Orbit
         Coupling, and Exciton Binding Energies in ZnO under Hydrostatic Pressure. *Solid State
         Commun.* **1995**, *94* (4), 251–254. https://doi.org/10.1016/0038-1098(95)00054-2.

(86)   Woggon, U.; Hild, K.; Gindele, F.; Langbein, W.; Hetterich, M.; Grün, M.; Klingshirn, C.
         Huge Binding Energy of Localized Biexcitons in CdS/ZnS Quantum Structures. *Phys.
         Rev. B - Condens. Matter Mater. Phys.* **2000**, *61* (19), 12632–12635.
         https://doi.org/10.1103/PhysRevB.61.12632.

(87)   Zheng, Q.; Zhou, W.; Peng, Y.; Yin, Y.; Zhong, M.; Zhao, Z.; Zhang, Q.; Tang, D.; Zeng,
         R.; Zou, B. Surface Polarons and Optical Micro-Cavity Modulated Broad Range Multi-
         Mode Emission of Te-Doped CdS Nanowires. *Nanotechnology* **2018**, *29*, 465709.
         https://doi.org/10.1088/1361-6528/aadf64.

(88)   Wang, X.; Zou, B.; Zhang, Q.; Lei, A.; Zhang, W.; Ren, P. Synthesis and
         Photoluminescence of Wurtzite CdS and ZnS Architectural Structures via a Facile
         Solvothermal Approach in Mixed Solvents. *J. Alloys Compd.* **2011**, *509* (41), 9959–9963.
         https://doi.org/10.1016/j.jallcom.2011.08.001.

(89)   Liu, R.; Li, Z. A.; Zhang, C.; Wang, X.; Kamran, M. A.; Farle, M.; Zou, B. Single-Step

Synthesis of Monolithic Comb-like CdS Nanostructures with Tunable Waveguide Properties. *Nano Lett.* **2013**, *13* (6), 2997–3001. https://doi.org/10.1021/nl401726z.

(90)   Weisbuch, C.; Nishioka, M.; Ishikawa, A.; Arakawa, Y. Observation of the Coupled Exciton-Photon Mode Splitting in a Semiconductor Quantum Microcavity. *Phys. Rev. Lett.* **1992**, *69* (23), 3314–3317. https://doi.org/10.1103/PhysRevLett.69.3314.

(91)   Van Vugt, L. K.; Piccione, B.; Cho, C. H.; Nukala, P.; Agarwal, R. One-Dimensional Polaritons with Size-Tunable and Enhanced Coupling Strengths in Semiconductor Nanowires. *PNAS* **2011**, *108* (25), 10050–10055. https://doi.org/https://doi.org/10.1073/pnas.1102212108.

(92)   Guo, S.; Zhao, F. Y.; Li, Y.; Song, G. L.; Li, A.; Chai, K.; Liang, L.; Ma, Z.; Weller, D.; Liu, R. B. Individual Dual-Emitting CdS Multi-Branched Nanowire Arrays under Various Pumping Powers. *Appl. Phys. Lett.* **2016**, *109*, 162101. https://doi.org/10.1063/1.4964879.

(93)   Leite, R. C. C.; Scott, J. F.; Damen, T. C. Multiple-Phonon Resoanant Raman Scattering in CdS. *Phys. Rev. Lett.* **1969**, *22* (15), 780–782. https://doi.org/https://doi.org/10.1103/PhysRevLett.22.780.

(94)   Kamran, M. A.; Nabi, G.; Majid, A.; Iqbal, M. W.; Alharbi, T.; Zhang, Y.; Zou, B. Tunable Emission and Conductivity Enhancement by Tellurium Doping in CdS Nanowires for Optoelectronic Applications. *Phys. E Low-Dimensional Syst. Nanostructures* **2017**, *86*, 81–87. https://doi.org/10.1016/j.physe.2016.10.009.

(95)   Khan, M. S.; Shi, L.; Zou, B. First Principle Calculations on Electronic, Magnetic and Optical Properties of Mn Doped and N Co-Doped CdS. *Mater. Res. Express* **2019**, *6*, 116126. https://doi.org/10.1088/2053-1591/ab4e40.

(96)   Guo, S.; Wang, L.; Ding, C.; Li, J.; Chai, K.; Li, W.; Xin, Y.; Zou, B.; Liu, R. Tunable Optical Loss and Multi-Band Photodetection Based on Tin Doped CdS Nanowire. *J. Alloys Compd.* **2020**, *835*, 155330. https://doi.org/10.1016/j.jallcom.2020.155330.

(97)   Radovanovic, P. V.; Barrelet, C. J.; Gradečak, S.; Qian, F.; Lieber, C. M. General Synthesis of Manganese-Doped II-VI and III-V Semiconductor Nanowires. *Nano Lett.* **2005**, *5* (7), 1407–1411. https://doi.org/10.1021/nl050747t.

(98)   Ge, F. J.; Peng, H.; Tian, Y.; Fan, X. Y.; Zhang, S.; Wu, X. X.; Liu, X. F.; Zou, B. S. Magnetic Polaron-Related Optical Properties in Ni(II)-Doped CdS Nanobelts: Implication for Spin Nanophotonic Devices. *Chinese Phys. B* **2022**, *31*, 017802. https://doi.org/10.1088/1674-1056/ac0782.

(99)   Zhang, L.; Zhang, Y.; Guo, Y.; Wang, Y.; Liu, R.; Chen, B.; Zhong, H.; Zou, B. Growth of CdS Nanotubes and Their Strong Optical Microcavity Effects. *Nanoscale* **2019**, *11* (12), 5325–5329. https://doi.org/10.1039/c8nr10323b.

(100)   Zhang, L.; Liu, R.; Zou, B. Sn-Doped CdS Nanowires with Low-Temperature Lasing by CW-Laser Excitation. *ACS Appl. Electron. Mater.* **2020**, *2* (1), 282–289. https://doi.org/10.1021/acsaelm.9b00766.

(101)   Kindig, N. B.; Spicer, W. E. Band Structure of Cadmium Sulfide-Photoemission Studies. *Phys. Rev.* **1965**, *138* (2A), A561. https://doi.org/10.1103/PhysRev.138.A561.

(102)   Kamran, M. A.; Liu, R.; Shi, L. J.; Li, Z. A.; Marzi, T.; Schöppner, C.; Farle, M.; Zou, B. Tunable Emission Properties by Ferromagnetic Coupling Mn(II) Aggregates in Mn-Doped CdS Microbelts/Nanowires. *Nanotechnology* **2014**, *25*, 385201. https://doi.org/10.1088/0957-4484/25/38/385201.

(103)   Delikanli, S.; He, S.; Qin, Y.; Zhang, P.; Zeng, H.; Zhang, H.; Swihart, M. Room Temperature Ferromagnetism in Mn-Doped CdS Nanorods. *Appl. Phys. Lett.* **2008**, *93*, 132501. https://doi.org/10.1063/1.2982583.

(104)   Dietl, T.; Ohno, H.; Matsukura, F.; Cibert, J.; Ferrand, D. Zener Model Description of Ferromagnetism in Zinc-Blende Magnetic Semiconductors. *Science (80-.)*. **2000**, *287* (5455), 1019–1022. https://doi.org/10.1126/science.287.5455.1019.

(105)   Dietl, T. A Ten-Year Perspective on Dilute Magnetic Semiconductors and Oxides. *Nat. Mater.* **2010**, *9* (12), 965–974. https://doi.org/10.1038/nmat2898.

(106)   Wojtowicz, T.; Kolenik, S.; Miotkowski, I.; Furdyna, J. K. Magnetization of Bound Magnetic Polarons: Direct Determination via Photomemory Effect. *Phys. Rev. Lett.* **1993**, *70* (15), 2317–2320. https://doi.org/10.1103/PhysRevLett.70.2317.

(107)   Kamran, M. A.; Zou, B.; Liu, R.; Saeed, M. A.; Majid, A.; Alharbi, T.; Iqbal, M. W.;

Shah, T. U. H. Single-Channel Dual Tunable Emission in the Visible and near-Infrared Region Using Aggregations of Mn(II) Ions in an Individual Mn-Doped CdS Nanosheet. *J. Phys. Chem. Solids* **2019**, *132*, 197–203. https://doi.org/10.1016/j.jpcs.2019.04.034.

(108) Bhattacharyya, S.; Estrin, Y.; Rich, D. H.; Zitoun, D.; Koltypin, Y.; Gedanken, A. Luminescent and Ferromagnetic CdS:Mn2+/C Core - Shell Nanocrystals. *J. Phys. Chem. C* **2010**, *114*, 22002–22011. https://doi.org/https://doi.org/10.1021/jp107083f.

(109) Nag, A.; Cherian, R.; Mahadevan, P.; Gopal, A. V.; Hazarika, A.; Mohan, A.; Vengurlekar, A. S.; Sarma, D. D. Size-Dependent Tuning of Mn2+ d Emission in Mn 2+-Doped CdS Nanocrystals: Bulk vs Surface. *J. Phys. Chem. C* **2010**, *114* (43), 18323–18329. https://doi.org/10.1021/jp105688w.

(110) Zuo, T.; Sun, Z.; Zhao, Y.; Jiang, X.; Gao, X. The Big Red Shift of Photoluminescence of Mn Dopants in Strained CdS: A Case Study of Mn-Doped MnS-CdS Heteronanostructures. *J. Am. Chem. Soc.* **2010**, *132* (19), 6618–6619. https://doi.org/10.1021/ja100136a.

(111) Bhattacharjee, A.; Benoit a la Guillaume, C. Exciton Magnetic Polaron in Semimagnetic Semiconductor Nanocrystals. *Phys. Rev. B - Condens. Matter Mater. Phys.* **1997**, *55* (16), 10613–10620. https://doi.org/10.1103/PhysRevB.55.10613.

(112) Yang, G.; Xu, G.; Chen, B.; Zou, S.; Liu, R.; Zhong, H.; Zou, B. General Synthesis and White Light Emission of Diluted Magnetic Semiconductor Nanowires Using Single-Source Precursors. *Chem. Mater.* **2013**, *25* (15), 3260–3266. https://doi.org/10.1021/cm401864d.

(113) Hazarika, A.; Layek, A.; De, S.; Nag, A.; Debnath, S.; Mahadevan, P.; Chowdhury, A.; Sarma, D. D. Ultranarrow and Widely Tunable Mn2+-Induced Photoluminescence from Single Mn-Doped Nanocrystals of ZnS-CdS Alloys. *Phys. Rev. Lett.* **2013**, *110*, 267401. https://doi.org/10.1103/PhysRevLett.110.267401.

(114) Kamran, M. A. Role of Ni2+ (D8) Ions in Electrical, Optical and Magnetic Properties of CdS Nanowires for Optoelectronic and Spintronic Applications. *Nanotechnology* **2018**, *29*, 265602. https://doi.org/10.1088/1361-6528/aabdc2.

(115) Deka, K.; Kalita, M. P. C. Structural Phase Controlled Transition Metal (Fe, Co, Ni, Mn)
       Doping in CdS Nanocrystals and Their Optical, Magnetic and Photocatalytic Properties. *J.
       Alloys Compd.* **2018**, *757*, 209–220. https://doi.org/10.1016/j.jallcom.2018.04.323.

(116) Kamran, M. A.; Zou, B.; Zhang, K.; Yang, X.; Ge, F.; Shi, L.; Alharbi, T. Dual-Color
       Lasing Lines from EMPs in Diluted Magnetic Semiconductor CdS:NiI Structure.
       Research **2019**, *2019*, 6956937. https://doi.org/10.34133/2019/6956937.

(117) Zou, M.; Wang, J.; Khan, M. S.; Mahmood, A.; Zhang, L.; Guo, Y.; Zhang, K.; Wang, S.;
       Zou, B. Spin-Related Optical Behaviors of Dilute Magnetic Semiconductor ZnSe:Ni(II)
       Nanobelts. *Nanotechnology* **2020**, *31*, 325002. https://doi.org/10.1088/1361-6528/ab7cec.

(118) Godlewski, M.; Yatsunenko, S.; Khachapuridze, A.; Ivanov, V. Y.; Gołacki, Z.;
       Karczewski, G.; Bergman, P. J.; Klar, P. J.; Heimbrodt, W.; Phillips, M. R. Mechanism of
       Intra-Shell Recombination of Transition Metal and Rare Earth Ions in Nanostructures of
       II-VI Compounds. *J. Alloys Compd.* **2004**, *380*, 45–49.
       https://doi.org/10.1016/j.jallcom.2004.03.020.

(119) Bonanni, A.; Navarro-Quezada, A.; Li, T.; Wegscheider, M.; Matěj, Z.; Holý, V.;
       Lechner, R. T.; Bauer, G.; Rovezzi, M.; D'Acapito, F.; Kiecana, M.; Sawicki, M.; Dietl,
       T. Controlled Aggregation of Magnetic Ions in a Semiconductor: An Experimental
       Demonstration. *Phys. Rev. Lett.* **2008**, *101*, 135502.
       https://doi.org/10.1103/PhysRevLett.101.135502.

(120) Kamran, M. A.; Liu, R.; Shi, L. J.; Zou, B.; Zhang, Q. Near Infrared Emission Band and
       Origin in Ni(II)-Doped CdS Nanoribbons by CVD Technique. *J. Phys. Chem. C* **2013**, *117*
       (34), 17777–17785. https://doi.org/10.1021/jp402831n.

(121) Heitz, R.; Hoffmann, A.; Broser, I. Magneto-Optics of Ni-Bound Shallow States in ZnS
       and CdS. *Phys. Rev. B* **1993**, *48* (12), 8672–8682.
       https://doi.org/10.1103/PhysRevB.48.8672.

(122) Zhang, K.; Zhao, D.; Wang, J.; Zhang, L.; Zou, M.; Guo, Y.; Wang, S.; Zou, B.; Zou, B.
       Bosonic Lasing of Collective Exciton Magnetic Polarons in CuCl2-Doped CdS
       Nanoribbons: Implications for Quantum Light Sources. *ACS Appl. Nano Mater.* **2020**, *3*

Materials Advances Accepted Manuscript

(6), 5019–5032. https://doi.org/10.1021/acsanm.9b02324.

(123) Tian, Y.; Yao, S.; Lin, W.; Peng, H.; Zhang, Y.; Zou, B. Effect of Quantum Confinement on Polarization Anisotropy Emission in Sn-Doped CdS Microcones. *Mater. Adv.* **2022**, *3* (5), 8407–8412. https://doi.org/10.1039/d2ma00883a.

(124) Tolbert, S. H.; Alivisatos, A. P. The Wurtzite to Rock Salt Structural Transformation in CdSe Nanocrystals under High Pressure. *J. Chem. Phys.* **1995**, *102* (11), 4642–4656. https://doi.org/10.1063/1.469512.

(125) Rosen, D. L.; Li, Q. X.; Alfano, R. R. Native Defects in Undoped Semi-Insulating CdSe Studied by Photoluminescence and Absorption. *Phys. Rev. B* **1985**, *31* (4), 2396–2403. https://doi.org/10.1103/PhysRevB.31.2396.

(126) Jin, W.; Liu, Y.; Yuan, K.; Zhang, K.; Ye, Y.; Wei, W.; Dai, L. Barrier Height Inhomogeneity in Mixed-Dimensional Graphene/Single CdSe Nanobelt Schottky Junctions. *IEEE Electron Device Lett.* **2019**, *40* (1), 119–122. https://doi.org/10.1109/LED.2018.2880476.

(127) Deng, Z.; Cao, L.; Tang, F.; Zou, B. A New Route to Zinc-Blende CdSe Nanocrystals: Mechanism and Synthesis. *J. Phys. Chem. B* **2005**, *109* (35), 16671–16675. https://doi.org/10.1021/jp052484x.

(128) Dai, G.; Zhang, Q.; Peng, Z.; Zhou, W.; Xia, M.; Wan, Q.; Pan, A.; Zou, B. One-Step Synthesis of Low-Dimensional CdSe Nanostructures and Optical Waveguide of CdSe Nanowires. *J. Phys. D. Appl. Phys.* **2008**, *41*, 135301. https://doi.org/10.1088/0022-3727/41/13/135301.

(129) Kuno, M.; Lee, J. K.; Dabbousi, B. O.; Mikulec, F. V.; Bawendi, M. G. The Band Edge Luminescence of Surface Modified CdSe Nanocrystallites: Probing the Luminescing State. *J. Chem. Phys.* **1997**, *106* (23), 9869–9882. https://doi.org/10.1063/1.473875.

(130) Pan, A.; Liu, R.; Zhang, Q.; Wan, Q.; He, P.; Zacharias, M.; Zou, B. Fabrication and Red-Color Lasing of Individual Highly Uniform Single-Crystal CdSe Nanobelts. *J. Phys. Chem. C* **2007**, *111* (38), 14253–14256. https://doi.org/10.1021/jp0740548.

(131) Achtstein, A. W.; Scott, R.; Kickhöfel, S.; Jagsch, S. T.; Christodoulou, S.; Bertrand, G.

H. V.; Prudnikau, A. V.; Antanovich, A.; Artemyev, M.; Moreels, I.; Schliwa, A.; Woggon, U. P -State Luminescence in CdSe Nanoplatelets: Role of Lateral Confinement and a Longitudinal Optical Phonon Bottleneck. *Phys. Rev. Lett.* **2016**, *116*, 116802. https://doi.org/10.1103/PhysRevLett.116.116802.

(132) Jin, W.; Mu, X.; Zhang, K.; Shang, Z.; Dai, L. Influence of Interface Inhomogeneity on the Electrical Transport Mechanism of CdSe Nanowire/Au Schottky Junctions. *Phys. Chem. Chem. Phys.* **2018**, *20* (30), 19932–19937. https://doi.org/10.1039/c8cp02859a.

(133) Mirov, S.; Fedorov, V.; Moskalev, I.; Martyshkin, D.; Kim, C. Progress in Cr2+ and Fe2+ Doped Mid-IR Laser Materials. *Laser Photonics Rev.* **2010**, *4* (1), 21–41. https://doi.org/10.1002/lpor.200810076.

(134) An, Q.; Meng, X.; Xiong, K.; Qiu, Y. A High-Performance Fully Nanostructured Individual CdSe Nanotube Photodetector with Enhanced Responsivity and Photoconductive Gain. *J. Mater. Chem. C* **2017**, *5* (28), 7057–7066. https://doi.org/10.1039/c7tc01650f.

(135) Miethe, J. F.; Schlosser, A.; Eckert, J. G.; Lübkemann, F.; Bigall, N. C. Electronic Transport in CdSe Nanoplatelet Based Polymer Fibres. *J. Mater. Chem. C* **2018**, *6* (40), 10916–10923. https://doi.org/10.1039/c8tc03879a.

(136) Yu, J. H.; Liu, X.; Kweon, K. E.; Joo, J.; Park, J.; Ko, K. T.; Lee, D. W.; Shen, S.; Tivakornsasithorn, K.; Son, J. S.; Park, J. H.; Kim, Y. W.; Hwang, G. S.; Dobrowolska, M.; Furdyna, J. K.; Hyeon, T. Giant Zeeman Splitting in Nucleation-Controlled Doped CdSe:Mn2+ Quantum Nanoribbons. *Nat. Mater.* **2010**, *9* (1), 47–53. https://doi.org/10.1038/nmat2572.

(137) Awschalom, D. D.; Samarth, N. Spin Dynamics and Quantum Transport in Magnetic Semiconductor Quantum Structures. *J. Magn. Magn. Mater.* **1999**, *200*, 130–147. https://doi.org/10.1016/S0304-8853(99)00424-2.

(138) Žutić, I.; Fabian, J.; Sarma, S. Das. Spintronics: Fundamentals and Applications. *Rev. Mod. Phys.* **2004**, *76* (2), 323–410. https://doi.org/10.1103/RevModPhys.76.323.

(139) Yu, D.; Wehrenberg, B. L.; Yang, I.; Kang, W.; Guyot-Sionnest, P. Magnetoresistance of

N-Type Quantum Dot Solids. *Appl. Phys. Lett.* **2006**, *88*, 072504.
https://doi.org/10.1063/1.2174089.

(140) Hoffman, D. M.; Meyer, B. K.; Ekimov, A. I.; Merkulov, I. A.; Efros, A. L.; Rosen, M.;
Couino, G.; Gacoin, T.; Boilot, J. P. Giant Internal Magnetic Fields in Mn Doped
Nanocrystal Quantum Dots. *Solid State Commun.* **2000**, *114* (10), 547–550.
https://doi.org/10.1016/S0038-1098(00)00089-2.

(141) Babunts, R. A.; Uspenskaya, Y. A.; Romanov, N. G.; Orlinskii, S. B.; Mamin, G. V.;
Shornikova, E. V.; Yakovlev, D. R.; Bayer, M.; Isik, F.; Shendre, S.; Delikanli, S.; Demir,
H. V.; Baranov, P. G. High-Frequency EPR and ENDOR Spectroscopy of Mn2+ Ions in
CdSe/CdMnS Nanoplatelets. *ACS Nano* **2023**, *17* (5), 4474–4482.
https://doi.org/10.1021/acsnano.2c10123.

(142) Erwin, S. C.; Zu, L.; Haftel, M. I.; Efros, A. L.; Kennedy, T. A.; Norris, D. J. Doping
Semiconductor Nanocrystals. *Nature* **2005**, *436* (7047), 91–94.
https://doi.org/10.1038/nature03832.

(143) Mikulec, F. V.; Kuno, M.; Bennati, M.; Hall, D. A.; Griffin, R. G.; Bawendi, M. G.
Organometallic Synthesis and Spectroscopic Characterization of Manganese Doped CdSe
Nanocrystals. *J. Am. Chem. Soc.* **2000**, *122* (11), 2532–2540.
https://doi.org/https://doi.org/10.1021/ja991249n.

(144) Yu, J.; Chen, R. Optical Properties and Applications of Two-Dimensional CdSe
Nanoplatelets. *InfoMat* **2020**, *2* (5), 905–927. https://doi.org/10.1002/inf2.12106.

(145) Chen, R.; Bakti Utama, M. I.; Peng, Z.; Peng, B.; Xiong, Q.; Sun, H. Excitonic Properties
and Near-Infrared Coherent Random Lasing in Vertically Aligned CdSe Nanowires. *Adv.
Mater.* **2011**, *23* (11), 1404–1408. https://doi.org/10.1002/adma.201003820.

(146) Biadala, L.; Louyer, Y.; Tamarat, P.; Lounis, B. Direct Observation of the Two Lowest
Exciton Zero-Phonon Lines in Single CdSe/ZnS Nanocrystals. *Phys. Rev. Lett.* **2009**, *103*,
037404. https://doi.org/10.1103/PhysRevLett.103.037404.

(147) Akimov, V. A.; Kozlovskii, V. I.; Korostelin, Y. V; Landman, A. I.; Podmar'kov, Y. P.;
Skasyrsky, Y. K.; Frolov, M. P. Efficient Cw Lasing in a Cr2+:CdSe Crystal. *Quantum*

Electron. **2007**, *37* (11), 991–992. https://doi.org/10.1070/qe2007v037n11abeh013715.

(148) Akimov, V. A.; Kozlovskii, V. I.; Korostelin, Y. V; Landman, A. I.; Podmar'kov, Y. P.; Skasyrskii, Y. K.; Frolov, M. P. Efficient Pulsed Cr2+:CdSe Laser Continuously Tunable in the Spectral Range from 2.26 to 3.61 Mm. *Quantum Electron.* **2008**, *38* (3), 205–208. https://doi.org/10.1070/qe2008v038n03abeh013707.

(149) Grim, J. Q.; Christodoulou, S.; Di Stasio, F.; Krahne, R.; Cingolani, R.; Manna, L.; Moreels, I. Continuous-Wave Biexciton Lasing at Room Temperature Using Solution-Processed Quantum Wells. *Nat. Nanotechnol.* **2014**, *9* (11), 891–895. https://doi.org/10.1038/nnano.2014.213.

(150) Jiang, T.; Wang, T.; Meng, X. Synthesis and Characterization of Twin Crystal CdTe Nanowires. *J. Cryst. Growth* **2019**, *526*, 125202. https://doi.org/10.1016/j.jcrysgro.2019.125202.

(151) Bellet-Amalric, E.; Panciera, F.; Patriarche, G.; Travers, L.; Den Hertog, M.; Harmand, J. C.; Glas, F.; Cibert, J. Regulated Dynamics with Two Monolayer Steps in Vapor-Solid-Solid Growth of Nanowires. *ACS Nano* **2022**, *16* (3), 4397–4407. https://doi.org/10.1021/acsnano.1c10666.

(152) Tang, Z.; Kotov, N. A.; Giersig, M. Spontaneous Organization of Single CdTe Nanoparticles into Luminescent Nanowires. *Science (80-.).* **2002**, *297* (5579), 237–240. https://doi.org/10.1126/science.1072086.

(153) Neretina, S.; Hughes, R. A.; Britten, J. F.; Sochinskii, N. V.; Preston, J. S.; Mascher, P. Vertically Aligned Wurtzite CdTe Nanowires Derived from a Catalytically Driven Growth Mode. *Nanotechnology* **2007**, *18*, 275301. https://doi.org/10.1088/0957-4484/18/27/275301.

(154) Hiesinger, P.; Suga, S.; Willmann, F.; Dreybrodt, W. Excitation Spectra of Exciton Luminescence in CdTe. *Phys. Status Solidi* **1975**, *67* (2), 641–652. https://doi.org/10.1002/pssb.2220670227.

(155) Kurchatov, I. S.; Bulychev, N. A.; Bundyuk, A. V.; Kazaryan, M. A.; Kustov, D. M. Study of Spectral Characteristics of Materials for IR Lasers Based on II–VI

Semiconductors Doped with Iron-Group Ions. *Bull. Lebedev Phys. Inst.* **2015**, *42* (4), 107–109. https://doi.org/10.3103/S1068335615040041.

(156) Bukivskii, A. P.; Gnatenko, Y. P.; Bukivskij, P. M.; Furier, M. S.; Tarahan, L. M.; Gamernyk, R. V. Photoluminescence and Photoelectric Properties of CdTe Crystals Doped with Mo. *Phys. B Condens. Matter* **2020**, *576*, 411737. https://doi.org/10.1016/j.physb.2019.411737.

(157) Besombes, L.; Boukari, H. Resonant Optical Pumping of a Mn Spin in a Strain-Free Quantum Dot. *Phys. Rev. B - Condens. Matter Mater. Phys.* **2014**, *89* (8), 085315. https://doi.org/10.1103/PhysRevB.89.085315.

(158) Lafuente-Sampietro, A.; Utsumi, H.; Boukari, H.; Kuroda, S.; Besombes, L. Resonant Optical Control of the Spin of a Single Cr Atom in a Quantum Dot. *Phys. Rev. B* **2017**, *95* (3), 035303. https://doi.org/10.1103/PhysRevB.95.035303.

(159) Lafuente-Sampietro, A.; Boukari, H.; Besombes, L. Resonant Photoluminescence of a Positively Charged Mn-Doped Quantum Dot. *Phys. Stat. Sol.* **2016**, *13* (7–9), 546–550. https://doi.org/10.1002/pssc.201.

(160) Le Gall, C.; Brunetti, A.; Boukari, H.; Besombes, L. Electron-Nuclei Spin Dynamics in II-VI Semiconductor Quantum Dots. *Phys. Rev. B - Condens. Matter Mater. Phys.* **2012**, *85* (19), 195312. https://doi.org/10.1103/PhysRevB.85.195312.

(161) Varghese, B.; Boukari, H.; Besombes, L. Dynamics of a Mn Spin Coupled to a Single Hole Confined in a Quantum Dot. *Phys. Rev. B - Condens. Matter Mater. Phys.* **2014**, *90* (11), 115307. https://doi.org/10.1103/PhysRevB.90.115307.

(162) Kasprzak, J.; Richard, M.; Kundermann, S.; Baas, A.; Jeambrun, P.; Keeling, J. M. J.; Marchetti, F. M.; Szymánska, M. H.; André, R.; Staehli, J. L.; Savona, V.; Littlewood, P. B.; Deveaud, B.; Dang, L. S. Bose-Einstein Condensation of Exciton Polaritons. *Nature* **2006**, *443* (7110), 409–414. https://doi.org/10.1038/nature05131.

(163) Huang, R.; Yamamoto, Y.; Yamamoto, Y.; André, R.; Bleuse, J.; Muller, M.; Ulmer-Tuffigo, H. Exciton-Polariton Lasing and Amplification Based on Exciton-Exciton Scattering in CdTe Microcavity Quantum Wells. *Phys. Rev. B - Condens. Matter Mater.*

Phys. **2002**, *65* (16), 1653141–1653147. https://doi.org/10.1103/PhysRevB.65.165314.

(164) Haizheng, Z.; Nagy, M.; Jones, M.; Scholes, G. D. Electronic States and Exciton Fine Structure in Colloidal CdTe Nanocrystals. *J. Phys. Chem. C* **2009**, *113* (24), 10465–10470. https://doi.org/10.1021/jp901995c.

(165) Li, Q.; Lian, T. Exciton Spatial Coherence and Optical Gain in Colloidal Two-Dimensional Cadmium Chalcogenide Nanoplatelets. *Acc. Chem. Res.* **2019**, *52* (9), 2684–2693. https://doi.org/10.1021/acs.accounts.9b00252.

(166) Yang, P. D. From Nanowire Lasers to Quantum Wire Lasers. In *Proc. SPIE Physics and Simulation of Optoelectronic Devices XII*; 2004; Vol. 5349, pp 18–23. https://doi.org/10.1117/12.529975.

(167) Hu, J.; Odom, T. W.; Lieber, C. M. Chemistry and Physics in One Dimension: Synthesis and Properties of Nanowires and Nanotubes. *Acc. Chem. Res.* **1999**, *32* (5), 435–445. https://doi.org/10.1021/ar9700365.

(168) Pan, A.; Liu, R.; Yang, Q.; Zhu, Y.; Yang, G.; Zou, B.; Chen, K. Stimulated Emissions in Aligned CdS Nanowires at Room Temperature. *J. Phys. Chem. B* **2005**, *109* (51), 24268–24272. https://doi.org/10.1021/jp055164m.

(169) Liu, B.; Chen, R.; Xu, X. L.; Li, D. H.; Zhao, Y. Y.; Shen, Z. X.; Xiong, Q. H.; Sun, H. D. Exciton-Related Photoluminescence and Lasing in CdS Nanobelts. *J. Phys. Chem. C* **2011**, *115* (26), 12826–12830. https://doi.org/10.1021/jp203551f.

(170) Aubert, T.; Cirillo, M.; Flamee, S.; Deun, R. Van; Lange, H.; Thomsen, C.; Hens, Z. Homogeneously Alloyed CdSe1−xSx Quantum Dots (0≤x≤1): An Efficient Synthesis for Full Optical Tunability. *Chem. Mater.* **2013**, *25*, 2388–2390. https://doi.org/https://doi.org/10.1021/cm401019t.

(171) Shukla, R. S.; Zala, V. B.; Gupta, S. K.; Gajjar, P. N. ZnS/CdX (X = S, Se, Te) Core/Shell Nanowires: An Attempt at Tuning the Electronic Bandgaps and SQ Efficiencies. *J. Mater. Chem. C* **2021**, *9* (20), 6605–6617. https://doi.org/10.1039/d0tc05574c.

(172) Zhou, W.; Liu, R.; Tang, D.; Zou, B. Surface Polarity Induced Three-Dimensional Wurtzite ZnS/ZnSxSe1-x Nano-Heterostructures with Integrating Emission Property.

Materials Advances Accepted Manuscript

CrystEngComm **2013**, *15* (46), 9988–9994. https://doi.org/10.1039/c3ce41873a.

(173) Guo, P.; Yang, Q.; Shen, X.; Lv, Q.; Hao, Y.; Xiao, L.; Ho, J. C.; Yu, K. M. Room-Temperature Broad-Wavelength-Tunable Single-Mode Lasing from Alloyed CdS1-XSex Nanotripods. *ACS Nano* **2022**, *16* (8), 12767–12776. https://doi.org/10.1021/acsnano.2c04632.

(174) Zou, S.; Zhou, W.; Liu, R.; Zou, B. Cavity-Enhanced Microphotoluminescence in a Core-Shell n-p CdS/CdO Micrometer Wire and Its Efficient Surface Photovoltage Responses in the Whole Visible Range. *J. Phys. Chem. C* **2017**, *121* (26), 14349–14358. https://doi.org/10.1021/acs.jpcc.7b04053.

(175) Pan, A.; Liu, D.; Liu, R.; Wang, F.; Zhu, X.; Zou, B. Optical Waveguide through CdS Nanoribbons. *Small* **2005**, *1* (10), 980–983. https://doi.org/10.1002/smll.200500112.

(176) Yang, G.; Zhong, H.; Bai, Z.; Liu, R.; Zou, B. Ultralong Homogeneously Alloyed CdSexS1-x Nanowires with Highly Polarized and Color-Tunable Emissions. *Adv. Opt. Mater.* **2014**, *2* (9), 885–891. https://doi.org/10.1002/adom.201400138.

(177) Keene, J. D.; McBride, J. R.; Orfield, N. J.; Rosenthal, S. J. Elimination of Hole-Surface Overlap in Graded CdSxSe1-x Nanocrystals Revealed by Ultrafast Fluorescence Upconversion Spectroscopy. *ACS Nano* **2014**, *8* (10), 10665–10673. https://doi.org/10.1021/nn504235w.

(178) Garrett, M. D.; Dukes, A. D.; McBride, J. R.; Smith, N. J.; Pennycook, S. J.; Rosenthal, S. J. Band Edge Recombination in CdSe, CdS and CdSxSe1-x Alloy Nanocrystals Observed by Ultrafast Fluorescence Upconversion: The Effect of Surface Trap States. *J. Phys. Chem. C* **2008**, *112* (33), 12736–12746. https://doi.org/10.1021/jp803708r.

(179) Pan, A.; Yang, H.; Liu, R.; Yu, R.; Zou, B.; Wang, Z. Color-Tunable Photoluminescence of Alloyed CdSxSe1-x Nanobelts. *J. Am. Chem. Soc* **2006**, *37* (5), 15692–15693. https://doi.org/10.1002/chin.200605008.

(180) Ruberu, T. P. A.; Vela, J. Expanding the One-Dimensional CdS-CdSe Composition Landscape: Axially Anisotropic CdS1-XSex Nanorods. *ACS Nano* **2011**, *5* (7), 5775–5784. https://doi.org/10.1021/nn201466b.

(181) Singh, S.; Singh, A.; Palaniappan, K.; Ryan, K. M. Colloidal Synthesis of Homogeneously Alloyed CdSexS1−x Nanorods with Compositionally Tunable Photoluminescence. *Chem. Commun.* **2013**, *49* (87), 10293–10295. https://doi.org/10.1039/c3cc45497e.

(182) Al-Salim, N.; Young, A. G.; Tilley, R. D.; McQuillan, A. J.; Xia, J. Synthesis of CdSeS Nanocrystals in Coordinating and Noncoordinating Solvents: Solvent's Role in Evolution of the Optical and Structural Properties. *Chem. Mater.* **2007**, *19* (21), 5185–5193. https://doi.org/10.1021/cm070818k.

(183) Padilha, L. A.; Stewart, J. T.; Sandberg, R. L.; Bae, W. K.; Koh, W. K.; Pietryga, J. M.; Klimov, V. I. Carrier Multiplication in Semiconductor Nanocrystals: Influence of Size, Shape, and Composition. *Acc. Chem. Res.* **2013**, *46* (6), 1261–1269. https://doi.org/10.1021/ar300228x.

(184) Cohen, E.; Sturge, M. D. Fluorescence Line Narrowing, Localized Exciton States, and Spectral Diffusion in the Mixed Semiconductor CdSxSe1-X. *Phys. Rev. B* **1982**, *25* (6), 3828–3840. https://doi.org/10.1103/PhysRevB.25.3828.

(185) Cunningham, P. D.; Boercker, J. E.; Foos, E. E.; Lumb, M. P.; Smith, A. R.; Tischler, J. G.; Melinger, J. S. Enhanced Multiple Exciton Generation in Quasi-One-Dimensional Semiconductors. *Nano Lett.* **2011**, *11* (8), 3476–3481. https://doi.org/10.1021/nl202014a.

(186) Lei, Y.; Du, B.; Du, P.; Wu, Y.; Wang, Y.; Li, C.; Luo, L.; Zou, B. The Effects of Se/S Ratio on the Photoelectric Properties of Nitrogen -Doped Graphene Quantum Dots Decorated CdSxSe1-x Composites. *Ceram. Int.* **2022**, *48* (4), 5280–5288. https://doi.org/10.1016/j.ceramint.2021.11.071.

(187) Guo, S.; Li, Z.; Song, G.; Zou, B.; Wang, X.; Liu, R. Large-Area Photodetector with High-Sensitivity and Broadband Spectral Response Based on Composition-Graded CdSSe Nanowire-Chip. *J. Alloys Compd.* **2015**, *649*, 793–800. https://doi.org/10.1016/j.jallcom.2015.07.179.

(188) Zhang, M.; Guo, S.; Weller, D.; Hao, Y.; Wang, X.; Ding, C.; Chai, K.; Zou, B.; Liu, R. CdSSe Nanowire-Chip Based Wearable Sweat Sensor. *J. Nanobiotechnology* **2019**, *17*, 42. https://doi.org/10.1186/s12951-019-0480-4.

(189) Ding, C.; Lu, T.; Wazir, N.; Ma, W.; Guo, S.; Xin, Y.; Li, A.; Liu, R.; Zou, B. New Type of Thermoelectric CdSSe Nanowire Chip. *ACS Appl. Mater. Interfaces* **2021**, *13* (26), 30959–30966. https://doi.org/10.1021/acsami.1c04206.

(190) Zeng, R.; Zhang, T.; Liu, J.; Hu, S.; Wan, Q.; Liu, X.; Peng, Z.; Zou, B. Aqueous Synthesis of Type-II CdTe/CdSe Core-Shell Quantum Dots for Fluorescent Probe Labeling Tumor Cells. *Nanotechnology* **2009**, *20*, 095102. https://doi.org/10.1088/0957-4484/20/9/095102.

(191) Li, Y.; Zhong, H.; Li, R.; Zhou, Y.; Yang, C.; Li, Y. High-Yield Fabrication and Electrochemical Characterization of Tetrapodal CdSe, CdTe, and CdSexTe1-x Nanocrystals. *Adv. Funct. Mater.* **2006**, *16* (13), 1705–1716. https://doi.org/10.1002/adfm.200500678.

(192) Gao, Y.; Li, M.; Delikanli, S.; Zheng, H.; Liu, B.; Dang, C.; Sum, T. C.; Demir, H. V. Low-Threshold Lasing from Colloidal CdSe/CdSeTe Core/Alloyed-Crown Type-II Heteronanoplatelets. *Nanoscale* **2018**, *10* (20), 9466–9475. https://doi.org/10.1039/c8nr01838c.

(193) Lo, S. S.; Major, T. A.; Petchsang, N.; Huang, L.; Kuno, M. K.; Hartland, G. V. Charge Carrier Trapping and Acoustic Phonon Modes in Single CdTe Nanowires. *ACS Nano* **2012**, *6* (6), 5274–5282. https://doi.org/10.1021/nn3010526.

(194) Dai, G.; Zou, B.; Wang, Z. Preparation and Periodic Emission of Superlattice CdS/CdS:SnS2 Microwires. *J. Am. Chem. Soc.* **2010**, *132* (35), 12174–12175. https://doi.org/10.1021/ja1037963.

(195) Dang, C.; Lee, J.; Breen, C.; Steckel, J. S.; Coe-Sullivan, S.; Nurmikko, A. Red, Green and Blue Lasing Enabled by Single-Exciton Gain in Colloidal Quantum Dot Films. *Nat. Nanotechnol.* **2012**, *7* (5), 335–339. https://doi.org/10.1038/nnano.2012.61.

(196) Peng, Y.; Luo, Y.; Zhou, W.; Zhong, X.; Yin, Y.; Tang, D.; Zou, B. Photoluminescence and Boosting Electron–Phonon Coupling in CdS Nanowires with Variable Sn(IV) Dopant Concentration. *Nanoscale Res. Lett.* **2021**, *16*, 19. https://doi.org/10.1186/s11671-021-03485-3.

(197) Tian, Y.; Peng, H.; Yao, S.; Zhou, Z.; Ke, B.; Lin, W.; Lu, F.; Yu, Z.; Jia, W.; Zhang, Y.; Zou, B. Repeatedly and Superbroad Wavelength Tuning Microcavity in a Single Sn-Doped CdS Microcone. *J. Phys. Chem. C* **2022**, *126* (30), 12696–12703. https://doi.org/10.1021/acs.jpcc.2c04142.

(198) Tian, Y.; Zhang, Y.; Peng, H.; Yao, S.; Huang, T.; Peng, C.; Yu, Z.; Ge, S.; Zou, B. Revealing the Quantum-Confined Free Exciton A Anisotropic Emission in a CdS/CdS:SnS2 Superlattice Nanocone via Angle-Resolved Photoluminescence Spectroscopy. *J. Phys. Chem. C* **2022**, *126* (2), 1064–1075. https://doi.org/10.1021/acs.jpcc.1c09755.

(199) Bao, Q.; Li, W.; Xu, P.; Zhang, M.; Dai, D.; Wang, P.; Guo, X.; Tong, L. On-Chip Single-Mode CdS Nanowire Laser. *Light Sci. Appl.* **2020**, *9*, 42. https://doi.org/10.1038/s41377-020-0277-0.

(200) Li, M.; Zhi, M.; Zhu, H.; Wu, W. Y.; Xu, Q. H.; Jhon, M. H.; Chan, Y. Ultralow-Threshold Multiphoton-Pumped Lasing from Colloidal Nanoplatelets in Solution. *Nat. Commun.* **2015**, *6*, 8513. https://doi.org/10.1038/ncomms9513.

(201) Tang, M.; Xu, P.; Wen, Z.; Chen, X.; Pang, C.; Xu, X.; Meng, C.; Liu, X.; Tian, H.; Raghavan, N.; Yang, Q. Fast Response CdS-CdSxTe1−x-CdTe Core-Shell Nanobelt Photodetector. *Sci. Bull.* **2018**, *63* (17), 1118–1124. https://doi.org/10.1016/j.scib.2018.08.003.

(202) Gorai, P.; Krasikov, D.; Grover, S.; Xiong, G.; Metzger, W. K.; Stevanović, V. A Search for New Back Contacts for CdTe Solar Cells. *Sci. Adv.* **2023**, *9* (8), 3761. https://doi.org/10.1126/sciadv.ade3761.

(203) Wojnar, P.; Płachta, J.; Reszka, A.; Lähnemann, J.; Kaleta, A.; Kret, S.; Baranowski, P.; Wójcik, M.; Kowalski, B. J.; Baczewski, L. T.; Karczewski, G.; Wojtowicz, T. Near-Infrared Emission from Spatially Indirect Excitons in Type II ZnTe/CdSe/(Zn,Mg)Te Core/Double-Shell Nanowires. *Nanotechnology* **2021**, *32* (49), 495202. https://doi.org/10.1088/1361-6528/ac218c.

(204) Wang, X.; Yu, J.; Chen, R. Optical Characteristics of ZnS Passivated CdSe/CdS Quantum

Materials Advances Accepted Manuscript

Dots for High Photostability and Lasing. *Sci. Rep.* **2018**, *8* (1), 17323.
https://doi.org/10.1038/s41598-018-35768-8.

(205) Kim, J. P.; Christians, J. A.; Choi, H.; Krishnamurthy, S.; Kamat, P. V. CdSeS Nanowires:
Compositionally Controlled Band Gap and Exciton Dynamics. *J. Phys. Chem. Lett.* **2014**,
5 (7), 1103–1109. https://doi.org/10.1021/jz500280g.

(206) Saenz, N.; Hamachi, L. S.; Wolock, A.; Goodge, B. H.; Kuntzmann, A.; Dubertret, B.;
Billinge, I.; Kourkoutis, L. F.; Muller, D. A.; Crowther, A. C.; Owen, J. S. Synthesis of
Graded CdS1−xSex Nanoplatelet Alloys and Heterostructures from Pairs of
Chalcogenoureas with Tailored Conversion Reactivity. *Chem. Sci.* **2023**, *14* (43), 12345–
12354. https://doi.org/10.1039/d3sc03384h.

(207) Liu, X. R.; Lei, Z. J.; Zhang, Y. Y.; Lu, H. L.; Zhao, F. G.; Liu, X.; Zhou, J. H.; Shen, Y.
M.; Peng, X. Photocatalytic Formation of P-S Bonds via CdSeS/CdZnS Quantum Dots
under Visible Light Irradiation. *Org. Chem. Front.* **2023**, *11*, 380–389.
https://doi.org/10.1039/d3qo01560b.

(208) Tao, A. R.; Habas, S.; Yang, P. Shape Control of Colloidal Metal Nanocrystals. *Small*
2008, *4* (3), 310–325. https://doi.org/10.1002/smll.200701295.

(209) Yang, G.; Zhong, H.; Liu, R.; Li, Y.; Zou, B. In Situ Aggregation of ZnSe Nanoparticles
into Supraparticles: Shape Control and Doping Effects. *Langmuir* **2013**, *29* (6), 1970–
1976. https://doi.org/10.1021/la304458q.

(210) Zhang, X. T.; Liu, Z.; Leung, Y. P.; Li, Q.; Hark, S. K. Growth and Luminescence of
Zinc-Blende-Structured ZnSe Nanowires by Metal-Organic Chemical Vapor Deposition.
Appl. Phys. Lett. **2003**, *83* (26), 5533–5535. https://doi.org/10.1063/1.1638633.

(211) Li, Q.; Gong, X.; Wang, C.; Wang, J.; Ip, K.; Hark, S. Size-Dependent Periodically
Twinned ZnSe Nanowires. *Adv. Mater.* **2004**, *16* (16), 1436–1440.
https://doi.org/10.1002/adma.200306648.

(212) Wang, Y. G.; Zou, B. S.; Wang, T. H.; Wang, N.; Cai, Y.; Chan, Y. F.; Zhou, S. X. I-V
Characteristics of Schottky Contacts of Semiconducting ZnSe Nanowires and Gold
Electrodes. *Nanotechnology* **2006**, *17* (9), 2420–2423. https://doi.org/10.1088/0957-

4484/17/9/059.

(213) Hou, L.; Chen, C.; Zhang, L.; Xu, Q.; Yang, X.; Farooq, M. I.; Han, J.; Liu, R.; Zhang, Y.; Shi, L.; Zou, B. Spin-Related Micro-Photoluminescence in Fe3+ Doped ZnSe Nanoribbons. *Appl. Sci.* **2017**, *7*, 39. https://doi.org/10.3390/app7010039.

(214) Sirkeli, V.; Radevici, I.; Sushkevich, K.; Huhtinen, H.; Nedeoglo, N.; Nedeoglo, D.; Paturi, P. Magnetic and Luminescent Properties of Nickel-Doped ZnSe Crystals. *Solid State Sci.* **2015**, *50*, 74–80. https://doi.org/10.1016/j.solidstatesciences.2015.10.018.

(215) Zhou, W.; Liu, R.; Tang, D.; Zou, B. The Effect of Dopant and Optical Micro-Cavity on the Photoluminescence of Mn-Doped ZnSe Nanobelts. *Nanoscale Res. Lett.* **2013**, *8*, 314. https://doi.org/10.1186/1556-276X-8-314.

(216) Zou, B.; Hou, L.; Tian, Y.; Han, J.; Peng, H.; Yang, X.; Shi, L. Anomalous Nonlinear Optical Effect and Enhanced Emission by Magnetic Excitons in CVD Grown Cobalt-Doped ZnSe Nanoribbon. *New J. Phys.* **2021**, *23*, 033019. https://doi.org/10.1088/1367-2630/abdb0a.

(217) Gan, C.; Zhang, Y.; Battaglia, D.; Peng, X.; Xiao, M. Fluorescence Lifetime of Mn-Doped ZnSe Quantum Dots with Size Dependence. *Appl. Phys. Lett.* **2008**, *92*, 241111. https://doi.org/10.1063/1.2945274.

(218) Acharya, S.; Sarkar, S.; Pradhan, N. Material Diffusion and Doping of Mn in Wurtzite ZnSe Nanorods. *J. Phys. Chem. C* **2013**, *117* (11), 6006–6012. https://doi.org/10.1021/jp400456t.

(219) Graf, C.; Hofmann, A.; Ackermann, T.; Boeglin, C.; Viswanatha, R.; Peng, X.; Rodríguez, A. F.; Nolting, F.; Rühl, E. Magnetic and Structural Investigation of ZnSe Semiconductor Nanoparticles Doped with Isolated and Core-Concentrated Mn2+ Ions. *Adv. Funct. Mater.* **2009**, *19* (15), 2501–2510. https://doi.org/10.1002/adfm.200801602.

(220) Vlaskin, V. A.; Janssen, N.; Van Rijssel, J.; Beaulac, R.; Gamelin, D. R. Tunable Dual Emission in Doped Semiconductor Nanocrystals. *Nano Lett.* **2010**, *10* (9), 3670–3674. https://doi.org/10.1021/nl102135k.

(221) Song, Y.; Sonntag, J.; Mirov, S. B.; Gmachl, C. F.; Khurgin, J. B. Mid-Infrared Light

Emission from a Fe2+:ZnSe Polycrystal Using Quantum Cascade Laser Pumping. *Appl. Phys. Lett.* **2014**, *105*, 141108. https://doi.org/10.1063/1.4897546.

(222) Luo, M.; Giles, N. C.; Roy, U. N.; Cui, Y.; Burger, A. Energy Transfer between Co2+ and Fe2+ Ions in Diffusion-Doped ZnSe. *J. Appl. Phys.* **2005**, *98*, 083507. https://doi.org/10.1063/1.2102069.

(223) Habura, K. H.; Afrassa, M. A.; Hone, F. G. Density Functional Theory Study of Zn(1-x)FexSe: Electronic Structure, Phonon, and Magnetic Properties. *AIP Adv.* **2023**, *13*, 035201. https://doi.org/10.1063/5.0133408.

(224) Shukla, G.; Abdullah, H. M.; Ray, A.; Tyagi, S.; Manchon, A.; Sanvito, S.; Schwingenschlögl, U. ZnSe and ZnTe as Tunnel Barriers for Fe-Based Spin Valves. *Phys. Chem. Chem. Phys.* **2023**, *25* (19), 13533–13541. https://doi.org/10.1039/d3cp00833a.

(225) Pradhan, N.; Peng, X. Efficient and Color-Tunable Mn-Doped ZnSe Nanocrystal Emitters: Control of Optical Performance via Greener Synthetic Chemistry. *J. Am. Chem. Soc.* **2007**, *129* (11), 3339–3347. https://doi.org/10.1021/ja068360v.

(226) Zhang, Y.; Gan, C.; Muhammad, J.; Battaglia, D.; Peng, X.; Xiao, M. Enhanced Fluorescence Intermittency in Mn-Doped Single ZnSe Quantum Dots. *J. Phys. Chem. C* **2008**, *112* (51), 20200–20205. https://doi.org/10.1021/jp805855m.

(227) Kulyuk, L. L.; Laiho, R.; Läshkul, A. V.; Lhderanta, E.; Nedeoglo, D. D.; Nedeoglo, N. D.; Radevici, I. V.; Siminel, A. V.; Sirkeli, V. P.; Sushkevich, K. D. Magnetic and Luminescent Properties of Iron-Doped ZnSe Crystals. *Phys. B* **2010**, *405* (20), 4330–4334. https://doi.org/10.1016/j.physb.2010.07.036.

(228) Liang, B. B.; Hou, L. P.; Zou, S. Y.; Zhang, L.; Guo, Y. C.; Liu, Y. T.; Farooq, M. U.; Shi, L. J.; Liu, R. B.; Zou, B. S. The Aggregation of Fe3+ and Their D-d Radiative Transitions in ZnSe:Fe3+ Nanobelts by CVD Growth. *RSC Adv.* **2018**, *8* (6), 3133–3139. https://doi.org/10.1039/c7ra11356k.

(229) Karipidou, A.; Nelkowski, H.; Roussos, G. Near Infrared Luminescence of Ni and Fe Doped ZnSe Crystals. *J. Cryst. Growth* **1982**, *59* (1–2), 307–311. https://doi.org/10.1016/0022-0248(82)90342-6.

(230) Nitsuk, Y. A.; Vaksman, Y. F.; Yatsun, V. V. Study of the Impurity Photoconductivity and Luminescence in ZnSe:Ni Crystals in the Visible Spectral Region. *Semiconductors* **2012**, *46* (10), 1265–1269. https://doi.org/10.1134/S1063782612100090.

(231) Kislov, A. N.; Mazurenko, V. G.; Sokolov, V. I.; Varaksin, A. N. Interaction of Nickel Donor and Acceptor Excitons with Defect Vibrations in ZnSe:Ni Crystals. *Phys. Solid State* **1997**, *39* (12), 1921–1924. https://doi.org/10.1134/1.1130200.

(232) Gudkov, V. V.; Lonchakov, A. T.; Tkach, A. V.; Zhevstovskikh, I. V.; Sokolov, V. I.; Gruzdev, N. B. Lattice Instability in ZnSe:Ni Crystal. *J. Electron. Mater.* **2004**, *33* (7), 815–818. https://doi.org/10.1007/s11664-004-0247-y.

(233) DeLoach, L. D.; Page, R. H.; Wilke, G. D.; Payne, S. A.; Krupke, W. F. Transition Metal-Doped Zinc Chalcogenides: Spectroscopy and Laser Demonstration of a New Class of Gain Media. *IEEE J. Quantum Electron.* **1996**, *32* (6), 885–895. https://doi.org/10.1109/3.502365.

(234) Robbins, A. D. J.; Dean, P. J.; West, C. L.; Hayes, W. The Deep Impurity Conduction Band Charge Transfer Transition In ZnSe:Co. *Philos. Trans. R. Soc. London. Ser. A* **1982**, *304* (1487), 499–531. https://doi.org/10.1098/rsta.1982.0019.

(235) Mierczyk, Z.; Majchrowski, A.; Kityk, I. V.; Gruhn, W. ZnSe:Co2+ - Nonlinear Optical Absorber for Giant-Pulse Eye-Safe Lasers. *Opt. Laser Technol.* **2003**, *35* (3), 169–172. https://doi.org/10.1016/S0030-3992(02)00167-6.

(236) Noras, J. M.; Szawelska, H. R.; Allen, J. W. Energy Levels of Cobalt in ZnSe and ZnS. *J. Phys. C Solid State Phys.* **1981**, *14* (22), 3255–3268. https://doi.org/10.1088/0022-3719/14/22/019.

(237) Norberg, N. S.; Parks, G. L.; Salley, G. M.; Gamelin, D. R. Giant Excitonic Zeeman Splittings in Colloidal Co2+-Doped ZnSe Quantum Dots. *J. Am. Chem. Soc.* **2006**, *128* (40), 13195–13203. https://doi.org/10.1021/ja063425f.

(238) Yang, X.; Lin, J.; Khan, M. S.; Zou, B.; Shi, L. Interstitial Zn-Modulated Ferromagnetism in Co-Doped ZnSe. *Mater. Res. Express* **2019**, *6*, 106121. https://doi.org/https://doi.org/10.1088/2053-1591/ab20de.

(239) Goetz, G.; Schulz, H. The 4T1(F) - 4A2(F) Luminescence of the Co2+ (D7) Impurity Centre in Zinc Selenide Crystals. *phys. stat. sol.* **1992**, *169*, 217–224. https://doi.org/https://doi.org/10.1002/pssb.2221690125.

(240) Robbins, D.; Dean, P.; Glasper, J.; Bishop, S. New High-Energy Luminescence Bands from Co2+ in ZnSe. *Solid State Commun.* **1980**, *36* (1), 61–67. https://doi.org/10.1016/0038-1098(80)90192-1.

(241) Luo, M.; Garces, N. Y.; Giles, N. C.; Roy, U. N.; Cui, Y.; Burger, A. Optical and Electron Paramagnetic Resonance Spectroscopies of Diffusion-Doped Co2+:ZnSe. *J. Appl. Phys.* **2006**, *99*, 073709. https://doi.org/10.1063/1.2188030.

(242) Zhou, W.; Liu, R.; Tang, D.; Wang, X.; Fan, H.; Pan, A.; Zhang, Q.; Wan, Q.; Zou, B. Luminescence and Local Photonic Confinement of Single ZnSe:Mn Nanostructure and the Shape Dependent Lasing Behavior. *Nanotechnology* **2013**, *24*, 055201. https://doi.org/10.1088/0957-4484/24/5/055201.

(243) Liu, Y. H.; Chen, H. Y.; Fan, H. F.; Chen, Y. H.; Wang, F. Unique Growth Pathway in Solution-Solid-Solid Nanowires: Cubic to Hexagonal Phase Transformation. *ACS Omega* **2020**, *5* (29), 18441–18448. https://doi.org/10.1021/acsomega.0c02302.

(244) Tran, M. T.; Du, N. V.; Tu, N.; Huyen, N. T.; Hung, N. D.; Viet, D. X.; Ha, N. N.; Trung, D. Q.; Huy, P. T. High-Quality Optically Defect-Free 1D ZnS Nanostructures by a Modified Thermal Evaporation Method. *Opt. Mater. (Amst).* **2022**, *124*, 111963. https://doi.org/10.1016/j.optmat.2021.111963.

(245) Barrelet, C. J.; Wu, Y.; Bell, D. C.; Lieber, C. M. Synthesis of CdS and ZnS Nanowires Using Single-Source Molecular Precursors. *J. Am. Chem. Soc.* **2003**, *125* (38), 11498–11499. https://doi.org/10.1021/ja036990g.

(246) Meng, X. M.; Liu, J.; Jiang, Y.; Chen, W. W.; Lee, C. S.; Bello, I.; Lee, S. T. Structure- and Size-Controlled Ultrafine ZnS Nanowires. *Chem. Phys. Lett.* **2003**, *382*, 434–438. https://doi.org/10.1016/j.cplett.2003.10.093.

(247) Ding, J. X.; Zapien, J. A.; Chen, W. W.; Lifshitz, Y.; Lee, S. T.; Meng, X. M. Lasing in ZnS Nanowires Grown on Anodic Aluminum Oxide Templates. *Appl. Phys. Lett.* **2004**, *85*

(12), 2361–2363. https://doi.org/10.1063/1.1791326.

(248) Wang, X.; Li, J.; Zhang, W.; Guo, S.; Zhang, Y.; Zou, B.; Liu, R. Synthesis and Characterization of Zinc Sulfide Nanobelts with Periodically Modulated Thickness. *Mater. Lett.* **2014**, *132*, 224–227. https://doi.org/10.1016/j.matlet.2014.06.102.

(249) Wang, X.; Huang, H.; Liang, B.; Liu, Z.; Chen, D.; Shen, G. ZnS Nanostructures: Synthesis, Properties, and Applications. *Crit. Rev. Solid State Mater. Sci.* **2013**, *38* (1), 57–90. https://doi.org/10.1080/10408436.2012.736887.

(250) Liu, Z.; Wang, X.; Zhu, H. A New Diluted Magnetic Semiconductor Based on the Expanded Phase of ZnS: Surmounting the Random Distribution of Magnetic Impurities. *Phys. Chem. Chem. Phys.* **2015**, *17* (19), 13117–13122. https://doi.org/10.1039/c4cp05739b.

(251) Qasem, A.; Xiong, P.; Ma, Z.; Peng, M.; Yang, Z. Recent Advances in Mechanoluminescence of Doped Zinc Sulfides. *Laser Photonics Rev.* **2021**, *15*, 2100276. https://doi.org/10.1002/lpor.202100276.

(252) Myoung, N.; Martyshkin, D. V.; Fedorov, V. V.; Mirov, S. B. Mid-IR Lasing of Iron-Cobalt Co-Doped ZnS(Se) Crystals via Co-Fe Energy Transfer. *J. Lumin.* **2013**, *133*, 257–261. https://doi.org/10.1016/j.jlumin.2011.10.004.

(253) Martyshkin, D. V.; Fedorov, V. V.; Kim, C.; Moskalev, I. S.; Mirov, S. B. Mid-IR Random Lasing of Cr-Doped ZnS Nanocrystals. *J. Opt. A* **2010**, *12*, 024005. https://doi.org/10.1088/2040-8978/12/2/024005.

(254) Chen, R.; Li, D.; Liu, B.; Peng, Z.; Gurzadyan, G. G.; Xiong, Q.; Sun, H. Optical and Excitonic Properties of Crystalline Zns Nanowires: Toward Efficient Ultraviolet Emission at Room Temperature. *Nano Lett.* **2010**, *10* (12), 4956–4961. https://doi.org/10.1021/nl102987z.

(255) Fernández, M.; Prete, P.; Lovergine, N.; Mancini, A.; Cingolani, R.; Vasanelli, L. Optical Properties of MOVPE-Grown ZnS Epilayers on (100) GaAs. *Phys. Rev. B - Condens. Matter Mater. Phys.* **1997**, *55* (12), 7660–7666. https://doi.org/10.1103/PhysRevB.55.7660.

Materials Advances Accepted Manuscript

(256) Hou, L.; Zhou, W.; Zou, B.; Zhang, Y.; Han, J.; Yang, X.; Gong, Z.; Li, J.; Xie, S.; Shi, L. J. Spin-Exciton Interaction and Related Micro-Photoluminescence Spectra of ZnSe:Mn DMS Nanoribbon. *Nanotechnology* **2017**, *28*, 105202. https://doi.org/10.1088/1361-6528/aa58f1.

(257) Kamran, M. A.; Majid, A.; Alharbi, T.; Iqbal, M. W.; Amjad, M. W.; Nabi, G.; Zou, S.; Zou, B. Large Tunable Luminescence by Mn(II) Aggregates in Mn-Doped ZnS Nanobelts. *J. Mater. Chem. C* **2017**, *5* (34), 8749–8757. https://doi.org/10.1039/c7tc02206a.

(258) Khan, M. S.; Zou, B.; Yao, S.; Haq, Z. ul; Abdulla, A. S.; Huang, W. G.; Zheng, B. Suppression of Ferromagnetism Due to N Co-Doping in Cr(II)-Doped ZnS Nanowires and Their Optical Properties: Insights from Density-Functional Calculations. *J. Magn. Magn. Mater.* **2023**, *582*, 171013. https://doi.org/10.1016/j.jmmm.2023.171013.

(259) Manojkumar, K.; Prasad, B.; Kranthi, Y.; Varma, J. S. K.; Vinay, K.; Amaranatha Reddy, D.; Subramanyam, K. Benchmark Analysis on Magnetic and Photoluminescence Properties of Selective Metal Ions Doped ZnS Nanoparticles. *J. Supercond. Nov. Magn.* **2019**, *32*, 2489–2500. https://doi.org/10.1007/s10948-018-4972-5.

(260) Patel, P. C.; Ghosh, S.; Srivastava, P. C. Bound Magnetic Polaron Driven Room-Temperature Ferromagnetism in Ni Doped ZnS Nanoparticles. *Mater. Chem. Phys.* **2018**, *216*, 285–293. https://doi.org/10.1016/j.matchemphys.2018.05.065.

(261) Basha, S. J.; Sarma, G. V. S. S.; Khidhirbrahmendra, V.; Rajyalakshmi, T.; Swetha, D.; Ravikumar, R. V. S. S. N. Enhanced Magnetic Properties of Fe3+ Doped ZnS Nanocrystals via Low Temperature Co-Precipitation: Spintronic and Nano-Device Applications. *Phys. Scr.* **2020**, *95*, 105802. https://doi.org/10.1088/1402-4896/abb41f.

(262) Patel, P. C.; Ghosh, S.; Mishra, P. K.; Srivastava, P. C. Enhanced Photocatalytic Activity and Low Temperature Magnetic/Transport Study of Cu-Doped ZnS-Based Diluted Magnetic Semiconductor Nanoparticles. *J. Electron. Mater.* **2019**, *48* (7), 4544–4551. https://doi.org/10.1007/s11664-019-07240-4.

(263) Ma, R.; Wei, X.; Wang, C.; Mao, S.; Chen, B.; Shao, Y.; Fu, Y.; Yan, K.; Peng, D. Reproducible Mechanical-to-Optical Energy Conversion in Mn (II) Doped Sphalerite ZnS.

J. Lumin. **2021**, *232*, 117838. https://doi.org/10.1016/j.jlumin.2020.117838.

(264) Patel, P. C.; Ghosh, S.; Srivastava, P. C. Unusual Ferromagnetic to Paramagnetic Change and Bandgap Shift in ZnS:Cr Nanoparticles. *J. Electron. Mater.* **2019**, *48* (11), 7031–7039. https://doi.org/10.1007/s11664-019-07507-w.

(265) Wang, X.; Zhang, Q.; Zou, B.; Lei, A.; Ren, P. Synthesis of Mn-Doped ZnS Architectures in Ternary Solution and Their Optical Properties. *Appl. Surf. Sci.* **2011**, *257* (24), 10898–10902. https://doi.org/10.1016/j.apsusc.2011.07.135.

(266) Li, Y. Q.; Zapien, J. A.; Shan, Y. Y.; Liu, Y. K.; Lee, S. T. Manganese Doping and Optical Properties of ZnS Nanoribbons by Postannealing. *Appl. Phys. Lett.* **2006**, *88*, 013115. https://doi.org/10.1063/1.2161073.

(267) Khan, M. S.; Shi, L.; Yang, X.; Ali, S.; Ullah, H.; Zou, B. Optoelectronic and Magnetic Properties of Mn-Doped and Mn-C Co-Doped Wurtzite ZnS: A First-Principles Study. *J. Phys. Condens. Matter* **2019**, *31* (39). https://doi.org/10.1088/1361-648X/ab2d98.

(268) Zou, M.; Wang, J.; Khan, M. S.; Mahmood, A.; Zhang, L.; Guo, Y.; Zhang, K.; Wang, S.; Zou, B. Spin-Related Optical Behaviors of Dilute Magnetic Semiconductor ZnSe:Ni(II) Nanobelts. *Nanotechnology* **2020**, *31* (32). https://doi.org/10.1088/1361-6528/ab7cec.

(269) Zou, B.; Hou, L.; Tian, Y.; Han, J.; Peng, H.; Yang, X.; Shi, L. Anomalous Nonlinear Optical Effect and Enhanced Emission by Magnetic Excitons in CVD Grown Cobalt-Doped ZnSe Nanoribbon. *New J. Phys.* **2021**, *23* (3). https://doi.org/10.1088/1367-2630/abdb0a.

(270) Kang, T.; Sung, J.; Shim, W.; Moon, H.; Cho, J.; Jo, Y.; Lee, W.; Kim, B. Synthesis and Magnetic Properties of Single-Crystalline Mn/Fe-Doped and Co-Doped ZnS. *J. Phys. Chem. C* **2009**, *113*, 5352–5357. https://doi.org/https://doi.org/10.1021/jp808433b.

(271) Wang, Y.; Ta, V. D.; Gao, Y.; He, T. C.; Chen, R.; Mutlugun, E.; Demir, H. V.; Sun, H. D. Stimulated Emission and Lasing from CdSe/CdS/ZnS Core-Multi-Shell Quantum Dots by Simultaneous Three-Photon Absorption. *Adv. Mater.* **2014**, *26* (18), 2954–2961. https://doi.org/10.1002/adma.201305125.

(272) Hou, L.; Zhang, Q.; Ling, L.; Li, C. X.; Chen, L.; Chen, S. Interfacial Fabrication of

Single-Crystalline ZnTe Nanorods with High Blue Fluorescence. *J. Am. Chem. Soc.* **2013**, *135* (29), 10618–10621. https://doi.org/10.1021/ja4047476.

(273) Wang, B. B.; Zhu, M. K.; Hu, N.; Li, L. J. Raman Scattering and Photoluminescence of Zinc Telluride Nanopowders at Room Temperature. *J. Lumin.* **2011**, *131* (12), 2550–2554. https://doi.org/10.1016/j.jlumin.2011.06.028.

(274) Yang, Y. W.; Li, T. Y.; Zhu, W. Bin; Ma, D. M.; Chen, D. Fabrication and Characterization of Single-Crystalline ZnTe Nanowire Arrays. *Chinese Phys. Lett.* **2013**, *30* (10), 12394–12398. https://doi.org/10.1088/0256-307X/30/10/108102.

(275) Janik, E.; Dłuzewski, P.; Kret, S.; Presz, A.; Kirmse, H.; Neumann, W.; Zaleszczyk, W.; Baczewski, L. T.; Petroutchik, A.; Dynowska, E.; Sadowski, J.; Caliebe, W.; Karczewski, G.; Wojtowicz, T. Catalytic Growth of ZnTe Nanowires by Molecular Beam Epitaxy: Structural Studies. *Nanotechnology* **2007**, *18* (47), 475606. https://doi.org/10.1088/0957-4484/18/47/475606.

(276) Bukhtiar, A.; Bingsuo, Z. Role of Growth Conditions on Optical Behavior of Mn Doped ZnTe by Using Chemical Vapor Deposition Route. *J. Nanosci. Nanotechnol.* **2018**, *13* (2), 281–288. https://doi.org/https://doi.org/10.1166/jno.2018.2187.

(277) Ogawa, H.; Nishio, M. Photoluminescence of ZnTe Homoepitaxial Layers Grown by Metalorganic Vapor-Phase Epitaxy at Low Pressure. *J. Appl. Phys.* **1989**, *66* (8), 3919–3921. https://doi.org/10.1063/1.344016.

(278) Shan, C. X.; Fan, X. W.; Zhang, J. Y.; Zhang, Z. Z.; Lu, Y. M.; Liu, Y. C.; Shen, D. Z. Temperature-Dependent Photoluminescence of ZnTe Films Grown on Si Substrates. *Chinese Phys. Lett.* **2003**, *20* (11), 2049–2052. https://doi.org/10.1088/0256-307X/20/11/042.

(279) Venghaus, H.; Dean, P. J. Shallow Acceptor Bound Exciton and Free Exciton States in High-Purity Zinc Telluride. *Solid State Commun.* **1979**, *31*, 897–900. https://doi.org/https://doi.org/10.1016/0038-1098(79)90413-7.

(280) Zhang, Q.; Liu, X.; Utama, M. I. B.; Zhang, J.; De La Mata, M.; Arbiol, J.; Lu, Y.; Sum, T. C.; Xiong, Q. Highly Enhanced Exciton Recombination Rate by Strong Electron-

Phonon Coupling in Single ZnTe Nanobelt. *Nano Lett.* **2012**, *12* (12), 6420–6427. https://doi.org/10.1021/nl3037867.

(281) Zhang, J.; Chen, P. C.; Shen, G.; He, J.; Kumbhar, A.; Zhou, C.; Fang, J. P-Type Field-Effect Transistors of Single-Crystal Zinc Telluride Nanobelts. *Angew. Chemie - Int. Ed.* **2008**, *47* (49), 9469–9471. https://doi.org/10.1002/anie.200804073.

(282) Wu, D.; Jiang, Y.; Zhang, Y.; Li, J.; Yu, Y.; Zhang, Y.; Zhu, Z.; Wang, L.; Wu, C.; Luo, L.; Jie, J. Device Structure-Dependent Field-Effect and Photoresponse Performances of p-Type ZnTe:Sb Nanoribbons. *J. Mater. Chem.* **2012**, *22* (13), 6206–6212. https://doi.org/10.1039/c2jm16632a.

(283) Li, S.; Jiang, Y.; Wu, D.; Wang, L.; Zhong, H.; Wu, B.; Lan, X.; Yu, Y.; Wang, Z.; Jie, J. Enhanced P-Type Conductivity of ZnTe Nanoribbons by Nitrogen Doping. *J. Phys. Chem. C* **2010**, *114* (17), 7980–7985. https://doi.org/10.1021/jp911873j.

(284) Zhou, W.; Tang, D.; Pan, A.; Zhang, Q.; Wan, Q.; Zou, B. Structure and Photoluminescence of Pure and Indium-Doped ZnTe Microstructures. *J. Phys. Chem. C* **2011**, *115* (5), 1415–1421. https://doi.org/10.1021/jp1069237.

(285) Bukhtiar, A.; BingSuo, Z. The Preparation and Optical Properties of Ni(II) and Mn(II) Doped in ZnTe Nanobelt/Nanorod by Using Chemical Vapor Deposition. *J. Nanosci. Nanotechnol.* **2018**, *18* (7), 4700–4713. https://doi.org/10.1166/jnn.2018.15283.

(286) Alhaddad, T.; Shoker, M. B.; Pagès, O.; Postnikov, A. V; Torres, V. J. B.; Polian, A.; Le Godec, Y.; Itié, J. P.; Broch, L.; Bouzourâa, M. B.; En Naciri, A.; Diliberto, S.; Michel, S.; Franchetti, P.; Marasek, A.; Strzałkowski, K. Raman Study of Cd1−xZnxTe Phonons and Phonon–Polaritons—Experiment and Ab Initio Calculations. *J. Appl. Phys.* **2023**, *133* (6), 65701. https://doi.org/10.1063/5.0134454.

(287) Zaleszczyk, W.; Janik, E.; Presz, A.; Piotr, D.; Kret, S.; Szuszkiewicz, W.; Morhange, J.; Dynowska, E.; Kirmse, H.; Neumann, W.; Petroutchik, A.; Baczewski, L. T.; Karczewski, G.; Wojtowicz, T. Zn1-XMnxTe Diluted Magnetic Semiconductor Nanowires Grown by Molecular Beam Epitaxy. *Nanoletters* **2008**, *8* (11), 4061–4065. https://doi.org/https://doi.org/10.1021/nl802449g.

(288) Kanazawa, K.; Nishimura, T.; Yoshida, S.; Shigekawa, H.; Kuroda, S. Real Space Probe of Short-Range Interaction between Cr in a Ferromagnetic Semiconductor ZnCrTe. *Nanoscale* **2014**, *6* (24), 14667–14673. https://doi.org/10.1039/c4nr04826a.

(289) Liu, Y. T.; Hou, L. P.; Zou, S. Y.; Zhang, L.; Liang, B. B.; Guo, Y. C.; Bukhtiar, A.; Farooq, M. U.; Zou, B. S. EMP Formation in the Co(II) Doped ZnTe Nanowires. *Chinese Phys. Lett.* **2018**, *35*, 037801. https://doi.org/10.1088/0256-307X/35/3/037801.

(290) Zhou, Y.; Tian, Y.; Bukhtiar, A.; Zhou, Z.; Zhao, H.; Lin, W.; Zhong, X.; Zou, B. Stable Near-Infrared Light and Microcavity of the ZnTe Microbelt and Different Emission Behaviors. *J. Phys. Chem. C* **2023**, *127* (14), 6906–6915. https://doi.org/10.1021/acs.jpcc.2c09006.

(291) Guo, J.; Xu, J.; Zhuang, X.; Wang, Y.; Zhou, H.; Shan, Z.; Ren, P.; Guo, P.; Zhang, Q.; Wan, Q.; Zhu, X.; Pan, A. Large Photoluminescence Redshift of ZnTe Nanostructures: The Effect of Twin Structures. *Chem. Phys. Lett.* **2013**, *576*, 26–30. https://doi.org/10.1016/j.cplett.2013.05.013.

(292) Iqbal, M. F.; Ain, Q. U.; Yaqoob, M. M.; Zhu, P.; Wang, D. Temperature Dependence of Exciton–Phonon Coupling and Phonon Anharmonicity in ZnTe Thin Films. *J. Raman Spectrosc.* **2022**, *53* (7), 1265–1274. https://doi.org/10.1002/jrs.6363.

(293) Peng, S.; Xing, G.; Tang, Z. Hot Electron-Hole Plasma Dynamics and Amplified Spontaneous Emission in ZnTe Nanowires. *Nanoscale* **2017**, *9* (40), 15612–15621. https://doi.org/10.1039/c7nr04168c.

(294) Dong, J.; Serita, K.; Murakami, F.; Kawayama, I.; Sun, H.; Zhang, B.; Tonouchi, M.; Jie, W.; Xu, Y. Laser Terahertz Emission Microscopy Revealing the Local Fluctuation of Terahertz Generation Induced by Te Inclusion. *Appl. Phys. Lett.* **2021**, *118* (13), 131113. https://doi.org/10.1063/5.0045266.

(295) Nie, K.-Y.; Luo, S.; Ren, F.-F.; Chen, X.; Gu, S.; Chen, Z.; Zhang, R.; Ye, J. Hybrid Plasmonic–Dielectric Metal-Nanowire Coupler for High-Efficiency Broadband Nonlinear Frequency Conversion. *Photonics Res.* **2022**, *10* (10), 2337. https://doi.org/10.1364/prj.465401.

(296) Zhang, Q.; Liu, X.; Utama, M. I. B.; Xing, G.; Sum, T. C.; Xiong, Q. Phonon-Assisted Anti-Stokes Lasing in ZnTe Nanoribbons. *Adv. Mater.* **2016**, *28* (2), 276–283. https://doi.org/10.1002/adma.201502154.

(297) Liu, Y. T.; Hou, L. P.; Zou, S. Y.; Zhang, L.; Liang, B. B.; Guo, Y. C.; Bukhtiar, A.; Farooq, M. U.; Zou, B. S. EMP Formation in the Co(II) Doped ZnTe Nanowires. *Chinese Phys. Lett.* **2018**, *35* (3). https://doi.org/10.1088/0256-307X/35/3/037801.

(298) Bukhtiar, A.; Ke, B.; Khan, M. S.; Liang, W.; Sulaman, M.; Imran, A.; Yao, S.; Zou, B. Photon-Carrier-Spin Coupling in One-Dimensional Ni(II) Doped ZnTe Nanostructure. *Nanotechnology* **2024**, 0–22. https://doi.org/10.1088/1361-6528/ad544c.

(299) Kempa, T. J.; Lieber, C. M. Semiconductor Nanowire Solar Cells: Synthetic Advances and Tunable Properties. *Pure Appl. Chem.* **2014**, *86* (1), 13–26. https://doi.org/10.1515/pac-2014-5010.

(300) Gargas, D. J.; Moore, M. C.; Ni, A.; Chang, S. W.; Zhang, Z.; Chuang, S. L.; Yang, P. Whispering Gallery Mode Lasing from Zinc Oxide Hexagonal Nanodisks. *ACS Nano* **2010**, *4* (6), 3270–3276. https://doi.org/10.1021/nn9018174.

(301) Gargas, D. J.; Gao, H.; Wang, H.; Yang, P. High Quantum Efficiency of Band-Edge Emission from ZnO Nanowires. *Nano Lett.* **2011**, *11* (9), 3792–3796. https://doi.org/10.1021/nl201850k.

(302) Dasgupta, N. P.; Yang, P. Semiconductor Nanowires for Photovoltaic and Photoelectrochemical Energy Conversion. *Front. Phys.* **2014**, *9* (3), 289–302. https://doi.org/10.1007/s11467-013-0305-0.

(303) Wang, F.; Cao, L.; Pan, A.; Liu, R.; Wang, X.; Zhu, X.; Wang, S.; Zou, B. Synthesis of Tower-like ZnO Structures and Visible Photoluminescence Origins of Varied-Shaped ZnO Nanostructures. *J. Phys. Chem. C* **2007**, *111* (21), 7655–7660. https://doi.org/10.1021/jp067151u.

(304) Briseno, A. L.; Holcombe, T. W.; Boukai, A. I.; Garnett, E. C.; Shelton, S. W.; Fréchet, J. J. M.; Yang, P. Oligo- and Polythiophene/ZnO Hybrid Nanowire Solar Cells. *Nano Lett.* **2010**, *10* (1), 334–340. https://doi.org/10.1021/nl9036752.

(305) Dietl, T. Ferromagnetic Semiconductors. *Semicond. Sci. Technol.* **2002**, *17* (1), 377–392. https://doi.org/10.1016/S0961-1290(05)00917-8.

(306) Lai, J. M.; Farooq, M. U.; Sun, Y. J.; Tan, P. H.; Zhang, J. Multiphonon Process in Mn-Doped ZnO Nanowires. *Nano Lett.* **2022**, *22* (13), 5385–5391. https://doi.org/10.1021/acs.nanolett.2c01428.

(307) Liu, R. Bin; Zou, B. S. Lasing Behaviour from the Condensation of Polaronic Excitons in a ZnO Nanowire. *Chinese Phys. B* **2011**, *20*, 047104. https://doi.org/10.1088/1674-1056/20/4/047104.

(308) Liu, R.; Pan, A.; Fan, H.; Wang, F.; Shen, Z.; Yang, G.; Xie, S.; Zou, B. Phonon-Assisted Stimulated Emission in Mn-Doped ZnO Nanowires. *J. Phys. Condens. Matter* **2007**, *19*, 136206. https://doi.org/10.1088/0953-8984/19/13/136206.

(309) Godlewski, M.; Yatsunenko, S.; Khachapuridze, A.; Ivanov, V. Y. Spin-Dependent Recombination Processes in Wide Band Gap II-Mn-VI Compounds. *J. Alloys Compd.* **2004**, *371* (1–2), 111–113. https://doi.org/10.1016/j.jallcom.2003.04.003.

(310) Dey, A.; Yarlagadda, S. Polaron Dynamics and Decoherence in an Interacting Two-Spin System Coupled to an Optical-Phonon Environment. *Phys. Rev. B - Condens. Matter Mater. Phys.* **2014**, *89*, 064311. https://doi.org/10.1103/PhysRevB.89.064311.

(311) Mizokawa, T.; Nambu, T.; Fujimori, A.; Fukumura, T.; Kawasaki, M. Electronic Structure of the Oxide-Diluted Magnetic Semiconductor Zn1-XMnxO. *Phys. Rev. B - Condens. Matter Mater. Phys.* **2002**, *65*, 085209. https://doi.org/10.1103/PhysRevB.65.085209.

(312) Ni, C. Y. A.; Chang, S. W.; Gargas, D. J.; Moore, M. C.; Yang, P.; Chuang, S. L. Metal-Coated Zinc Oxide Nanocavities. *IEEE J. Quantum Electron.* **2011**, *47* (2), 245–251. https://doi.org/10.1109/JQE.2010.2073680.

(313) Jiang, J.; Liao, Q.; Zhao, Y. S.; Yao, J. Tunable Two-Photon Pumped Lasing from Alloyed Semiconductor Nanoribbons. *J. Mater. Chem.* **2011**, *21* (13), 4837–4842. https://doi.org/10.1039/c0jm04437g.

(314) Chen, J.; Wu, Y.; Lei, Y.; Du, P.; Li, C.; Du, B.; Wang, Y.; Luo, L.; Bao, S.; Zou, B. The Effects of Zn/Cd Ratio and GQDs Doping on the Photoelectric Performance of ZnxCd1-

XSe. *Mater. Sci. Eng. B* **2022**, *286*, 116058. https://doi.org/10.1016/j.mseb.2022.116058.

(315) Kim, Y. H.; Yoon, S. Y.; Lee, Y. J.; Jo, D. Y.; Kim, H. M.; Kim, Y.; Park, S. M.; Park, G. M.; Kim, Y.; Kim, J.; Yang, H. Compositional and Heterostructural Tuning in Red-Emissive Ternary ZnSeTe Quantum Dots for Display Applications. *ACS Appl. Nano Mater.* **2023**, *6* (21), 19947–19954. https://doi.org/10.1021/acsanm.3c03749.

(316) Ghosh, K.; Ghorai, G.; Sahoo, P. K. Cathodoluminescence and Structural Properties of ZnTe Nanocrystals Synthesized from Te/ZnO Thin Films. *J. Alloys Compd.* **2023**, *960*, 170655. https://doi.org/10.1016/j.jallcom.2023.170655.

(317) Tang, J.; Li, F.; Yang, G.; Ge, Y.; Li, Z.; Xia, Z.; Shen, H.; Zhong, H. Reducing the Chromaticity Shifts of Light-Emitting Diodes Using Gradient-Alloyed CdxZn1−xSeyS1−y@ZnS Core Shell Quantum Dots with Enhanced High-Temperature Photoluminescence. *Adv. Opt. Mater.* **2019**, *7* (10), 1801687. https://doi.org/10.1002/adom.201801687.

(318) Zhai, T.; Zhong, H.; Gu, Z.; Peng, A.; Fu, H.; Ma, Y.; Li, Y.; Yao, J. Manipulation of the Morphology of ZnSe Sub-Micron Structures Using CdSe Nanocrystals as the Seeds. *J. Phys. Chem. C* **2007**, *111* (7), 2980–2986. https://doi.org/10.1021/jp067498x.

(319) Zeng, R.; Zhang, T.; Dai, G.; Zou, B. Highly Emissive, Color-Tunable, Phosphine-Free Mn:ZnSe/ZnS Core/Shell and Mn:ZnSeS Shell-Alloyed Doped Nanocrystals. *J. Phys. Chem. C* **2011**, *115* (7), 3005–3010. https://doi.org/10.1021/jp111288h.

(320) Zeng, R.; Shen, R.; Zhao, Y.; Sun, Z.; Li, X.; Zheng, J.; Cao, S.; Zou, B. Water-Soluble, Highly Emissive, Color-Tunable, and Stable Cu-Doped ZnSeS/ZnS Core/Shell Nanocrystals. *CrystEngComm* **2014**, *16* (16), 3414–3423. https://doi.org/10.1039/c3ce42273a.

(321) Zhou, W.; Pan, A.; Li, Y.; Dai, G.; Wan, Q.; Zhang, Q.; Zou, B. Controllable Fabrication of High-Quality 6-Fold Symmetry-Branched CdS Nanostructures with ZnS Nanowires as Templates. *J. Phys. Chem. C* **2008**, *112* (25), 9253–9260. https://doi.org/10.1021/jp800599e.

(322) Ke, B.; Bai, X.; Wang, R.; Shen, Y.; Cai, C.; Bai, K.; Zeng, R.; Zou, B.; Chen, Z.

Alkylthiol-Enabled Se Powder Dissolving for Phosphine-Free Synthesis of Highly Emissive, Large-Sized and Spherical Mn-Doped ZnSeS Nanocrystals. *RSC Adv.* **2017**, *7* (71), 44867–44873. https://doi.org/10.1039/c7ra06873e.

(323) Zeng, R.; Rutherford, M.; Xie, R.; Zou, B.; Peng, X. Synthesis of Highly Emissive Mn-Doped ZnSe Nanocrystals without Pyrophoric Reagents. *Chem. Mater.* **2010**, *22* (6), 2107–2113. https://doi.org/10.1021/cm9036023.

(324) Chin, P. T. K.; Stouwdam, J. W.; Janssen, R. A. J. Highly Luminescent Ultranarrow Mn Doped ZnSe Nanowires. *Nano Lett.* **2009**, *9* (2), 745–750. https://doi.org/https://doi.org/10.1021/nl8033015.

(325) Liang, Y.; Xu, H.; Hark, S. Epitaxial Growth and Composition-Dependent Optical Properties of Vertically Aligned ZnS1-XSex Alloy Nanowire Arrays. *Cryst. Growth Des.* **2010**, *10* (10), 4206–4210. https://doi.org/10.1021/cg9014493.

(326) Plaisant, M.; Ntwaeaborwa, O. M.; Swart, H. C.; Holloway, P. H. Nanostructure of CdxZn1-XSe Heterogeneous Nanorods. *Phys. B* **2014**, *439*, 72–76. https://doi.org/10.1016/j.physb.2013.11.053.

(327) Venugopal, R.; Lin, P. I.; Chen, Y. T. Photoluminescence and Raman Scattering from Catalytically Grown ZnxCd1-XSe Alloy Nanowires. *J. Phys. Chem. B* **2006**, *110* (24), 11691–11696. https://doi.org/10.1021/jp056892c.

(328) Yoon, Y. J.; Park, K. S.; Heo, J. H.; Park, J. G.; Nahm, S.; Choi, K. J. Synthesis of ZnxCd1-XSe ($0 \leq x \leq 1$) Alloyed Nanowires for Variable-Wavelength Photodetectors. *J. Mater. Chem.* **2010**, *20* (12), 2386–2390. https://doi.org/10.1039/b917531h.

(329) Shafique, S.; Yang, S.; Wang, Y.; Woldu, Y. T.; Cheng, B.; Ji, P. High-Performance Photodetector Using Urchin-like Hollow Spheres of Vanadium Pentoxide Network Device. *Sensors Actuators, A Phys.* **2019**, *296*, 38–44. https://doi.org/10.1016/j.sna.2019.07.003.

(330) Elahi, E.; Al-Kahtani, A. A.; Dastgeer, G.; Aftab, S.; Aziz, J.; Iqbal, M. W.; Manzoor, M.; Jeong, J.; Suleman, M.; Ahmed, B.; Koyyada, G.; Sharma, P. R. Recent Advances in Thermomagnetic Devices for Spin-Caloritronic Phenomena. *Appl. Mater. Today* **2023**, *32*,

101846. https://doi.org/10.1016/j.apmt.2023.101846.

(331) Sulaman, M.; Yang, S.; Guo, H.; Li, C.; Imran, A.; Bukhtiar, A.; Qasim, M.; Ge, Z.; Song, Y.; Jiang, Y.; Zou, B. Synergetic Enhancement of CsPbI3 Nanorod-Based High-Performance Photodetectors via PbSe Quantum Dot Interface Engineering. *Chem. Sci.* **2024**, *15* (22), 8514–8529. https://doi.org/10.1039/d4sc00722k.

(332) Sulaman, M.; Yang, S.; Imran, A.; Zhang, Z.; Bukhtiar, A.; Ge, Z.; Song, Y.; Sun, F.; Jiang, Y.; Tang, L.; Zou, B. Two Bulk-Heterojunctions Made of Blended Hybrid Nanocomposites for High-Performance Broadband, Self-Driven Photodetectors. *ACS Appl. Mater. Interfaces* **2023**, *15* (21), 25671–25683. https://doi.org/10.1021/acsami.3c01749.

(333) Johnson, J. C.; Yan, H.; Schaller, R. D.; Haber, L. H.; Saykally, R. J.; Yang, P. Single Nanowire Lasers. *J. Phys. Chem. B* **2001**, *105* (46), 11387–11390. https://doi.org/10.1021/jp012304t.

(334) Agarwal, R.; Barrelet, C. J.; Lieber, C. M. Lasing in Single Cadmium Sulfide Nanowire Optical Cavities. *Nano Lett.* **2005**, *5* (5), 917–920. https://doi.org/10.1021/nl050440u.

(335) Zapien, J. A.; Jiang, Y.; Meng, X. M.; Chen, W.; Au, F. C. K.; Lifshitz, Y.; Lee, S. T. Room-Temperature Single Nanoribbon Lasers. *Appl. Phys. Lett.* **2004**, *84* (7), 1189–1191. https://doi.org/10.1063/1.1647270.

(336) Zhao, D.; Liu, W.; Zhu, G.; Zhang, Y.; Wang, Y.; Zhou, W.; Xu, C.; Xie, S.; Zou, B. Surface Plasmons Promoted Single-Mode Polariton Lasing in a Subwavelength ZnO Nanowire. *Nano Energy* **2020**, *78*, 105202. https://doi.org/10.1016/j.nanoen.2020.105202.

(337) Zheng, H.; Jiang, Y.; Yang, S.; Zhang, Y.; Yan, X.; Hu, J.; Shi, Y.; Zou, B. ZnO Nanorods Array as Light Absorption Antenna for High-Gain UV Photodetectors. *J. Alloys Compd.* **2020**, *812*, 152158. https://doi.org/10.1016/j.jallcom.2019.152158.

(338) Zhao, D.; Zhu, G.; Zhang, Y.; Wang, Y.; Zhou, W.; Xie, S.; Zou, B. Surface Plasmon Enhanced Exciton Transitions, Cavity Resonance Effects, and Exciton-/Polariton-LO Phonon Interactions in ZnO Nanowires. *J. Phys. Chem. C* **2020**, *124* (51), 28252–28260. https://doi.org/10.1021/acs.jpcc.0c08114.

Materials Advances Accepted Manuscript

(339) Yan, H.; Johnson, J.; Law, M.; He, R.; Knutsen, K.; McKinney, J. R.; Pham, J.; Saykally, R.; Yang, P. ZnO Nanoribbon Microcavity Lasers. *Adv. Mater.* **2003**, *15* (22), 1907–1911. https://doi.org/10.1002/adma.200305490.

(340) Johnson, J. C.; Knutsen, K. P.; Yan, H.; Law, M.; Zhang, Y.; Yang, P.; Saykally, R. J. Ultrafast Carrier Dynamics in Single ZnO Nanowire and Nanoribbon Lasers. *Nano Lett.* **2004**, *4* (2), 197–204. https://doi.org/10.1021/nl034780w.

(341) Dai, G.; Zhang, Y.; Liu, R.; Wan, Q.; Zhang, Q.; Pan, A.; Zou, B. Visible Whispering-Gallery Modes in ZnO Microwires with Varied Cross Sections. *J. Appl. Phys.* **2011**, *110*, 033101. https://doi.org/10.1063/1.3610521.

(342) Zou, B.; Liu, R. Bin; Wang, F.; Pan, A.; Cao, L.; Wang, Z. L. Lasing Mechanism of ZnO Nanowires/Nanobelts at Room Temperature. *J. Phys. Chem. B* **2006**, *110* (26), 12865–12873. https://doi.org/10.1021/jp061357d.

(343) Huang, Z. T.; Chien, T. W.; Cheng, C. W.; Li, C. C.; Chen, K. P.; Gwo, S.; Lu, T. C. Room-Temperature Gate Voltage Modulation of Plasmonic Nanolasers. *ACS Nano* **2023**, *17* (7), 6488–6496. https://doi.org/10.1021/acsnano.2c11716.

(344) Sirbuly, D. J.; Law, M.; Yan, H.; Yang, P. Semiconductor Nanowires for Subwavelength Photonics Integration. *J. Phys. Chem. B* **2005**, *109* (32), 15190–15213. https://doi.org/10.1021/jp051813i.

(345) Law, M.; Greene, L. E.; Johnson, J. C.; Saykally, R.; Yang, P. Nanowire Dye-Sensitized Solar Cells. *Nat. Mater.* **2005**, *4* (6), 455–459. https://doi.org/10.1038/nmat1387.

(346) Kind, H.; Yan, H.; Messer, B.; Law, M.; Yang, P. Nanowire Ultraviolet Photodetectors and Optical Switches. *Adv. Mater.* **2002**, *14* (2), 158–160. https://doi.org/https://doi.org/10.1002/1521-4095(20020116)14:2<158::AID-ADMA158>3.0.CO;2-W.

(347) Lin, P.; Zhu, L.; Li, D.; Xu, L.; Wang, Z. L. Tunable WSe2-CdS Mixed-Dimensional van Der Waals Heterojunction with a Piezo-Phototronic Effect for an Enhanced Flexible Photodetector. *Nanoscale* **2018**, *10* (30), 14472–14479. https://doi.org/10.1039/c8nr04376k.

(348) Zhang, L.; Wang, Y.; Wu, H.; Hou, M.; Wang, J.; Zhang, L.; Liao, C.; Liu, S.; Wang, Y. A ZnO Nanowire-Based Microfiber Coupler for All-Optical Photodetection Applications. *Nanoscale* **2019**, *11* (17), 8319–8326. https://doi.org/10.1039/c9nr02040c.

(349) Du, J.; Liao, Q.; Hong, M.; Liu, B.; Zhang, X.; Yu, H.; Xiao, J.; Gao, L.; Gao, F.; Kang, Z.; Zhang, Z.; Zhang, Y. Piezotronic Effect on Interfacial Charge Modulation in Mixed-Dimensional Van Der Waals Heterostructure for Ultrasensitive Flexible Photodetectors. *Nano Energy* **2019**, *58*, 85–93. https://doi.org/10.1016/j.nanoen.2019.01.024.

(350) Lou, Z.; Yang, X.; Chen, H.; Liang, Z. Flexible Ultraviolet Photodetectors Based on ZnO-SnO2 Heterojunction Nanowire Arrays. *J. Semicond.* **2018**, *39*, 024002. https://doi.org/10.1088/1674-4926/39/2/024002.

(351) Goldberger, J.; Sirbuly, D. J.; Law, M.; Yang, P. ZnO Nanowire Transistors. *J. Phys. Chem. B* **2005**, *109* (1), 9–14. https://doi.org/10.1021/jp0452599.

(352) Barrelet, C. J.; Greytak, A. B.; Lieber, C. M. Nanowire Photonic Circuit Elements. *Nano Lett.* **2004**, *4* (10), 1981–1985. https://doi.org/10.1021/nl048739k.

(353) Hayden, O.; Agarwal, R.; Lieber, C. M. Nanoscale Avalanche Photodiodes for Highly Sensitive and Spatially Resolved Photon Detection. *Nat. Mater.* **2006**, *5* (5), 352–356. https://doi.org/10.1038/nmat1635.

(354) Barrelet, C. J.; Bao, J.; Lončar, M.; Park, H. G.; Capasso, F.; Lieber, C. M. Hybrid Single-Nanowire Photonic Crystal and Microresonator Structures. *Nano Lett.* **2006**, *6* (1), 11–15. https://doi.org/10.1021/nl0522983.

(355) Wang, X.; Pan, A.; Liu, D.; Zou, B.; Zhu, X. Comparison of the Optical Waveguide Behaviors of Se-Doped and Undoped CdS Nanoribbons by Using Near-Field Optical Microscopy. *J. Nanosci. Nanotechnol.* **2009**, *9* (2), 978–981. https://doi.org/10.1166/jnn.2009.C067.

(356) Johnson, J. C.; Yan, H.; Yang, P.; Saykally, R. J. Optical Cavity Effects in ZnO Nanowire Lasers and Waveguides. *J. Phys. Chem. B* **2003**, *107* (34), 8816–8828. https://doi.org/10.1021/jp034482n.

(357) Greytak, A. B.; Barrelet, C. J.; Li, Y.; Lieber, C. M. Semiconductor Nanowire Laser and

Nanowire Waveguide Electro-Optic Modulators. *Appl. Phys. Lett.* **2005**, *87*, 151103. https://doi.org/10.1063/1.2089157.

(358) Dai, G.; Wan, Q.; Zhou, C.; Yan, M.; Zhang, Q.; Zou, B. Sn-Catalyst Growth and Optical Waveguide of Ultralong CdS Nanowires. *Chem. Phys. Lett.* **2010**, *497* (1–3), 85–88. https://doi.org/10.1016/j.cplett.2010.07.095.

(359) Hao, Y.; Ding, C.; Lu, T.; Xie, L.; Nan, P.; Guo, S.; Wang, X.; Li, A.; Xu, X.; Zou, B.; Liu, R. Multipoint Nanolaser Array in an Individual Core–Shell CdS Branched Nanostructure. *Adv. Opt. Mater.* **2020**, *8* (11), 1901644. https://doi.org/10.1002/adom.201901644.

(360) Dai, G. Z.; Liu, R. B.; Wan, Q.; Zhang, Q. L.; Pan, A. L.; Zou, B. S. Color-Tunable Periodic Spatial Emission of Alloyed CdS1-XSex/ Sn:CdS1-XSex Superlattice Microwires. *Opt. Mater. Express* **2011**, *1* (7), 1185. https://doi.org/10.1364/ome.1.001185.

(361) Li, Y.; Dai, G.; Zhou, C.; Zhang, Q.; Wan, Q.; Fu, L.; Zhang, J.; Liu, R.; Cao, C.; Pan, A.; Zhang, Y.; Zou, B. Formation and Optical Properties of ZnO:ZnFe2O4 Superlattice Microwires. *Nano Res.* **2010**, *3* (5), 326–338. https://doi.org/10.1007/s12274-010-1036-y.

(362) Zou, B.; Dai, G.; Liu, R. Doping Effect on Novel Optical Properties of Semiconductor Nanowires. In *One-Dimensional Nanostructures: Principles and Applications*; John Wiley and Sons Inc, 2013; pp 185–205. https://doi.org/10.1002/9781118310342.ch9.

(363) Guo, S.; Liu, R.; Niu, C.; Weller, D.; Hao, Y.; Zhang, M.; Li, A.; Liang, L.; Wang, X.; Wang, X.; Yang, B.; Li, Z. A.; Pan, A. Tin Nanoparticles–Enhanced Optical Transportation in Branched CdS Nanowire Waveguides. *Adv. Opt. Mater.* **2018**, *6* (17), 1–8. https://doi.org/10.1002/adom.201800305.

(364) Zhao, X.; Li, Q.; Xu, L.; Zhang, Z.; Kang, Z.; Liao, Q.; Zhang, Y. Interface Engineering in 1D ZnO-Based Heterostructures for Photoelectrical Devices. *Adv. Funct. Mater.* **2022**, *32* (11), 2106887. https://doi.org/10.1002/adfm.202106887.

(365) Dong, B.; Cao, L.; Su, G.; Liu, W. Facile Synthesis of Highly Luminescent UV-Blue Emitting ZnSe/ZnS Core/Shell Quantum Dots by a Two-Step Method. *Chem. Commun.* **2010**, *46* (39), 7331–7333. https://doi.org/10.1039/c0cc02042g.

Materials Advances Accepted Manuscript

(366) Fang, Z.; Li, Y.; Zhang, H.; Zhong, X.; Zhu, L. Facile Synthesis of Highly Luminescent UV-Blue-Emitting ZnSe/ZnS Core/Shell Nanocrystals in Aqueous Media. *J. Phys. Chem. C* **2009**, *113* (32), 14145–14150. https://doi.org/10.1021/jp903806b.

(367) Ji, B.; Panfil, Y. E.; Waiskopf, N.; Remennik, S.; Popov, I.; Banin, U. Strain-Controlled Shell Morphology on Quantum Rods. *Nat. Commun.* **2019**, *10*, 2. https://doi.org/10.1038/s41467-018-07837-z.

(368) Riehle, F. S.; Bienert, R.; Thomann, R.; Urban, G. A.; Krüger, M. Blue Luminescence and Superstructures from Magic Size Clusters of CdSe. *Nano Lett.* **2009**, *9* (2), 514–518. https://doi.org/10.1021/nl080150o.

(369) Tyrakowski, C. M.; Shamirian, A.; Rowland, C. E.; Shen, H.; Das, A.; Schaller, R. D.; Snee, P. T. Bright Type II Quantum Dots. *Chem. Mater.* **2015**, *27* (21), 7276–7281. https://doi.org/10.1021/acs.chemmater.5b02040.

(370) Hu, L.; Yan, J.; Liao, M.; Xiang, H.; Gong, X.; Zhang, L.; Fang, X. An Optimized Ultraviolet-a Light Photodetector with Wide-Range Photoresponse Based on ZnS/ZnO Biaxial Nanobelt. *Adv. Mater.* **2012**, *24* (17), 2305–2309. https://doi.org/10.1002/adma.201200512.

(371) Zhang, X. M.; Lu, M. Y.; Zhang, Y.; Chen, L. J.; Wang, Z. L. Fabrication of a High-Brightness Blue-Light-Emitting Diode Using a ZnO-Nanowire Array Grown on p-GaN Thin Film. *Adv. Mater.* **2009**, *21* (27), 2767–2770. https://doi.org/10.1002/adma.200802686.

(372) Wang, L.; Lin, J.; Lv, Y.; Zou, B.; Zhao, J.; Liu, X. Red, Green, and Blue Microcavity Quantum Dot Light-Emitting Devices with Narrow Line Widths. *ACS Appl. Nano Mater.* **2020**, *3* (6), 5301–5310. https://doi.org/10.1021/acsanm.0c00695.

(373) Zhu, M.; Zhong, H.; Jia, J.; Fu, W.; Liu, J.; Zou, B.; Wang, Y. PVA Hydrogel Embedded with Quantum Dots: A Potential Scalable and Healable Display Medium for Holographic 3D Applications. *Adv. Opt. Mater.* **2014**, *2* (4), 338–342. https://doi.org/10.1002/adom.201300517.

(374) Tian, B.; Lieber, C. M. Synthetic Nanoelectronic Probes for Biological Cells and Tissues.

Annu. Rev. Anal. Chem. **2013**, *6*, 31–51. https://doi.org/10.1146/annurev-anchem-062012-092623.

(375) Jie, J. S.; Zhang, W. J.; Jiang, Y.; Lee, S. T. Transport Properties of Single-Crystal CdS Nanoribbons. *Appl. Phys. Lett.* **2006**, *89*, 223114. https://doi.org/10.1063/1.2398891.

(376) Jie, J. S.; Zhang, W. J.; Jiang, Y.; Lee, S. T. Single-Crystal CdSe Nanoribbon Field-Effect Transistors and Photoelectric Applications. *Appl. Phys. Lett.* **2006**, *89*, 133118. https://doi.org/10.1063/1.2345255.

(377) Li, G.; Jiang, Y.; Wang, Y.; Wang, C.; Sheng, Y.; Jie, J.; Zapien, J. A.; Zhang, W.; Lee, S. T. Synthesis of CdSxSe1-x Nanoribbons with Uniform and Controllable Compositions via Sulfurization: Optical and Electronic Properties Studies. *J. Phys. Chem. C* **2009**, *113* (39), 17183–17188. https://doi.org/10.1021/jp9046402.

(378) He, Z.; Zhang, W.; Zhang, W.; Jie, J.; Luo, L.; Yuan, G.; Wang, J.; Wu, C. M. L.; Bello, I.; Lee, C. S.; Lee, S. T. High-Performance CdSe:In Nanowire Field-Effect Transistors Based on Top-Gate Configuration with High-K Non-Oxide Dielectrics. *J. Phys. Chem. C* **2010**, *114* (10), 4663–4668. https://doi.org/10.1021/jp1007895.

(379) Ma, R. M.; Dai, L.; Qin, G. G. High-Performance Nano-Schottky Diodes and Nano-MESFETs Made on Single CdS Nanobelts. *Nano Lett.* **2007**, *7* (4), 868–873. https://doi.org/10.1021/nl062329+.

(380) Lu, J.; Liu, H.; Sun, C.; Zheng, M.; Nripan, M.; Chen, G. S.; Subodh, G. M.; Zhang, X.; Sow, C. H. Optical and Electrical Applications of ZnSxSe1-x Nanowires-Network with Uniform and Controllable Stoichiometry. *Nanoscale* **2012**, *4* (3), 976–981. https://doi.org/10.1039/c2nr11459c.

(381) Li, L.; Lu, H.; Yang, Z.; Tong, L.; Bando, Y.; Golberg, D. Bandgap-Graded CdSxSe1-x Nanowires for High-Performance Field-Effect Transistors and Solar Cells. *Adv. Mater.* **2013**, *25* (8), 1109–1113. https://doi.org/10.1002/adma.201204434.

(382) Ma, R. M.; Dai, L.; Huo, H. Bin; Xu, W. J.; Qin, G. G. High-Performance Logic Circuits Constructed on Single CdS Nanowires. *Nano Lett.* **2007**, *7* (11), 3300–3304. https://doi.org/10.1021/nl0715286.

Materials Advances Accepted Manuscript

(383) Li, Y.; Zhao, F.; Guo, S.; Zhang, Y.; Niu, C.; Zeng, R.; Zou, B.; Zhang, W.; Ding, K.; Bukhtiar, A.; Liu, R. Optically Programmable Encoder Based on Light Propagation in Two-Dimensional Regular Nanoplates. *Nanotechnology* **2017**, *28* (14), 145701. https://doi.org/10.1088/1361-6528/aa5f0f.

(384) Junpeng, L.; Cheng, S.; Minrui, Z.; Mathews, N.; Hongwei, L.; Gin Seng, C.; Xinhai, Z.; Mhaisalkar, S. G.; Chorng Haur, S. Facile One-Step Synthesis of CdSxSe1- x Nanobelts with Uniform and Controllable Stoichiometry. *J. Phys. Chem. C* **2011**, *115* (40), 19538–19545. https://doi.org/10.1021/jp205760r.

(385) Zheng, Y.; Li, L.; Zong, X.; Geng, Z.; Li, W.; Liu, Y. Large-Scale Plasmonic Nanodisk Array as a Biosensing Platform Fabricated by Transfer Nanoprinting. *Appl. Opt.* **2023**, *62* (29), 7706–7712. https://doi.org/10.1364/AO.499639.

(386) Yu, R.; Pan, C.; Wang, Z. L. High Performance of ZnO Nanowire Protein Sensors Enhanced by the Piezotronic Effect. *Energy Environ. Sci.* **2013**, *6* (2), 494–499. https://doi.org/10.1039/c2ee23718k.

(387) Wang, X.; Ozkan, C. S. Multisegment Nanowire Sensors for the Detection of DNA Molecules. *Nano Lett.* **2008**, *8* (2), 398–404. https://doi.org/10.1021/nl071180e.

(388) Ganguly, A.; Chen, C. P.; Lai, Y. T.; Kuo, C. C.; Hsu, C. W.; Chen, K. H.; Chen, L. C. Functionalized GaN Nanowire-Based Electrode for Direct Label-Free Voltammetric Detection of DNA Hybridization. *J. Mater. Chem.* **2009**, *19* (7), 928–933. https://doi.org/10.1039/b816556d.

(389) Li, Z.; Chen, Y.; Li, X.; Kamins, T. I.; Nauka, K.; Williams, R. S. Sequence-Specific Label-Free DNA Sensors Based on Silicon Nanowires. *Nano Lett.* **2004**, *4* (2), 245–247. https://doi.org/10.1021/nl034958e.

(390) Xie, P.; Xiong, Q.; Fang, Y.; Qing, Q.; Lieber, C. M. Local Electrical Potential Detection of DNA by Nanowire-Nanopore Sensors. *Nat. Nanotechnol.* **2012**, *7* (2), 119–125. https://doi.org/10.1038/nnano.2011.217.

(391) Fu, T. M.; Duan, X.; Jiang, Z.; Dai, X.; Xie, P.; Cheng, Z.; Lieber, C. M. Sub-10-Nm Intracellular Bioelectronic Probes from Nanowire-Nanotube Heterostructures. *PNAS*

2014, *111* (4), 1259–1264. https://doi.org/10.1073/pnas.1323389111.

(392) Dey, P.; Roy, J. N. Opto-Spintronics. In *Spintronics: Fundamentals and Applications*; Springer, 2021; p 163. https://doi.org/https://link.springer.com/book/10.1007/978-981-16-0069-2.

(393) Tanaka, M. Recent Progress in Ferromagnetic Semiconductors and Spintronics Devices. *Jpn. J. Appl. Phys.* **2020**, *60*, 010101. https://doi.org/10.35848/1347-4065/abcadc.

(394) Hirohata, A.; Yamada, K.; Nakatani, Y.; Prejbeanu, L.; Diény, B.; Pirro, P.; Hillebrands, B. Review on Spintronics: Principles and Device Applications. *J. Magn. Magn. Mater.* **2020**, *509*, 166711. https://doi.org/10.1016/j.jmmm.2020.166711.

(395) Grollier, J.; Querlioz, D.; Camsari, K. Y.; Everschor-Sitte, K.; Fukami, S.; Stiles, M. D. Neuromorphic Spintronics. *Nat. Electron.* **2020**, *3* (7), 360–370. https://doi.org/10.1038/s41928-019-0360-9.

Materials Advances Accepted Manuscript